博士論文

Non-Inductive Plasma Current Ramp-up on the TST-2 Spherical Tokamak Using the Lower Hybrid Wave

（TST-2 球状トカマクにおける低域混成波を用いた非誘導電流立ち上げ）

新屋　貴浩

Takahiro Shinya

December 9, 2015

Abstract

In order to develop a reliable method to initiate and ramp up the plasma current (I_p) in a spherical tokamak (ST) without using the central solenoid, non-inductive I_p ramp-up experiments were performed using the lower hybrid wave (LHW) on the TST-2 spherical tokamak. In order to achieve efficient I_p ramp-up, the capacitively-coupled combline (CCC) antenna was developed in collaboration with General Atomics (GA).

I_p was successfully ramped up using the CCC antenna to ~20 kA with low reflectivity ($\leq$ 10%) and high antenna-plasma coupling efficiency (100%). The achieved I_p is higher than the results achieved previously in TST-2 ($\leq$ 15 kA). The low reflectivity is one of our main aims to develop the CCC antenna because a large reflection due to low antenna-plasma coupling limited the input RF power to the Grill antenna in earlier experiments on TST-2. The I_p ramp-up rate was approximately 400 kA/sec. The initial $N_{\|}$ spectrum ($N_{\|,0}$) is also improved by the CCC antenna ($N_{\|}$ is the refractive index of the plasma in the direction of the magnetic field line). The $N_{\|,0}$ spectrum was calculated based on measurements by RF magnetic probes installed under the CCC antenna. The excited $N_{\|,0}$ spectrum has a sharp primary peak in the range $-9 \leq N_{\|,0} \leq -2$ and negligible secondary peaks. The spectral power at the main peak of the CCC antenna spectrum is larger than that of the Grill antenna spectrum by a factor of 3.

In order to investigate the optimum LHW antenna at 200 MHz for I_p ramp-up, a comparison among the three antennas: the CCC antenna (LHW excitation with a sharp, single-peaked $N_{\|,0}$ spectrum), the Grill antenna (LHW excitation with a a broad, double-peaked $N_{\|,0}$ spectrum), and the ICC antenna (FW excitation with a sharp, single-peaked $N_{\|,0}$ spectrum) was made. The comparison indicated that the CCC antenna achieved the highest current drive figure of merit (by a factor of 2–3 compared to other two antennas) and the highest antenna-plasma coupling efficiency (CCC: 100%, Grill: 40%–80%, ICC: 40%) at 10 kA. The I_p-P_{rad} relationship indicates that the LHW contributes more effectively to I_p ramp-up than the the FW by a factor of 2 at 15 kA. However, it was difficult to evaluate the dependence of I_p ramp-up on the $N_{\|,0}$ spectrum from the obtained results.

It was also revealed that I_p ramp-up is limited by the toroidal magnetic field

(B_t) and the plasma density. The obtained data was fitted well with the mode conversion curve for $N_{\|} = -5.5$ (which coincides with the peak of the $N_{\|,0}$ spectrum), and hence the B_t limit and the density limit are consistent with the mode conversion limit. The achieved I_p has a positive correlation with the plasma density. At higher densities the high energy electrons accelerated by the LHW slow down more quickly. The lower energy of these electrons results in reduced orbit losses. To achieve higher I_p with the CCC antenna, not only the pulse length, but also higher B_t and density are necessary. Since higher Bt and density lead to LHW power losses by PDI when $\omega < 2\omega_{LH}$, 30–50 kA is the limit for I_p at 200 MHz if I_p increases with density.

It was also found that removing the scrape-off layer (SOL) plasma at the upper and lower sides of the plasma is effective for achieving higher I_p. In the case without the upper and lower limiters (z450 limiter, $z = \pm 0.45$ m, 150 mm away from the LCFS), I_p ramp-up was arrested when the density reached $0.4 - 0.6 \times 10^{18}$ m^{-3}. The density limit was not alleviated by the increase of the magnetic field, and hence the density limit is not caused by mode conversion. LHW power loss in the SOL is a possible reason for the saturation ofI_p ramp-up as the density is increased. The density at the upper z450 limiter measured using Langmuir probes was higher than the cutoff density, and the presence of the LHW was verified by RF rectification observed in the floating potential.

We also succeeded in inventing a plasma density suppression method using the ECW, to keep the density lower than the density limit. The ECW was launched into plasmas with the fundamental EC resonance located at the nominal plasma center. Despite the low ECW power compared to the LHW power by a factor of 15, the ECW was effective in reducing the plasma density. The decrease in the line-integrated density, $n_e l$, (more precisely, the suppression of the $n_e l$ increase) was approximately 10%.

The experimentally inferred I_p ramp-up limitations, mode conversion of the LHW to the FW, and the LHW power loss in the SOL, can be avoided by developing a top-launch antenna according to ray-tracing calculations. The LHW excited by the top-launch antenna undergoes a quick up-shift in wavenumber as it propagates towards the plasma center, and is absorbed by bulk electrons. In addition to the wavenumber up-shift, the LHW accessibility condition is improved due to the higher toroidal magnetic field at smaller major radii (by a factor of two compared to the outboard-launch). I_p ramp-up at lower magnetic field also becomes possible, preventing LHW power loss by PDI that can become important at high magnetic fields (> 0.2 T). The top-launch antenna was developed in collaboration with GA, and has the same structure as the outboard-launch CCC antenna since the utility of the CCC antenna is verified experimentally. The top-launch antenna consists of 6 radiating elements, and the excited $N_{\|}$ is in the range -2 to -10 in vacuum. The top-launch antenna was installed at $z = 0.334$ m and the antenna limiter

at $z = 0.3$ m. A low reflectivity ($\sim 1\%$) and a high antenna-plasma coupuling ($\sim 100\ \%$) were verified with the plasma.

Contents

Chapter 1

Introduction

1.1 Nuclear fusion

Nuclear fusion is the reaction in which atomic nuclei fuse to form a heavier nucleus. When the sum of the masses of the final products is less than that of the initial nuclei by Δm, the energy ($E = \Delta mc^2$) is released. For example, the sun generates a huge amount of energy by fusion of hydrogen nuclei into a helium nucleus.

The fusion reactor utilizes the fusion reaction in order to generate energy on the earth [1, 2]. The most promising fusion reaction is that between deuterium (D) and tritium (T),

$$\mathrm{D} + \mathrm{T} \rightarrow \mathrm{He}^4\ (3.52\ \mathrm{MeV}) + \mathrm{n}\ (14.06\ \mathrm{MeV}). \tag{1.1}$$

For fusion reaction to occur, it is necessary to overcome the mutual Coulomb repulsion between ions due to their positive charges. This can be accomplished when ions are heated to sufficiently high temperatures in the plasma state. The fusion reaction cross-section increases with their energy, and reaches a maximum around 100 keV. The most important parameters of the plasma for a fusion reactor are temperature (T), confinement time (τ_E), and ion density (n). In 1957, J. D. Lawson derived the minimum value for the product of the confinement time and the ion density to produce a fusion output energy equal to the input energy [3]. This condition is called the Lawson criterion (break-even condition),

$$n\tau_E \geq 1.0 \times 10^{20}\ \mathrm{s/m^3}. \tag{1.2}$$

The minimum break-even condition, 1.0×10^{20} s/m^3, can be obtained when we assume that the ratio of the input power to the output thermal energy is 1/3 for

a 50/50 D-T mixture plasma at the optimum temperature of 15 keV. The ignition criterion is defined as maintaining the fusion reaction only by the fusion generated alpha particles (He^4) without any external heating. For a 50/50 D-T plasma with $n = 10^{20}$ m^{-3} and the optimum temperature of 30 keV, the ignition criterion given in Ref. [4] is

$$nT\tau_E \ > \ 8.1 \times 10^{21} \text{ keV} \cdot \text{s} \cdot \text{m}^3. \tag{1.3}$$

According to the conditions explained above, we have to confine a very hot plasma for a long enough time to obtain sufficient energy from the fusion reaction on the earth. Scientists have invented several effective methods of plasma confinement [5–11]. The *Tokamak*, which confines the plasma with nested toroidal surfaces formed by the magnetic field, is considered to be the most practical method for realizing a fusion reactor. The development and improvement of the tokamak is a main topic in this thesis.

1.2 Tokamak

The tokamak is presently the most successful confinement scheme for high density, high temperature plasmas [1, 6, 12, 13]. In 1998, an equivalent break-even condition was achieved on the JT-60U tokamak with D-D plasma operation. In order to study the fusion burn in D-T plasmas, the ITER project is in progress, and is now under construction in France [14, 15]. The main aim of the ITER project is to achieve $Q = 10$, where Q is the ratio of the fusion power to the input power. A brief description of tokamak basics is presented in this section.

The tokamak uses magnetic fields which trap charged particles and keep them away from material walls. The physical mechanism of trapping is the gyro-motion of the charged particles around a magnetic field line. A key point of the tokamak scheme is that the magnetic field line traces the surface of a torus, providing good confinement of particles. Hence, the vacuum vessel and the plasma are in the shape of a torus as shown in Fig. 1.1. The magnetic field in the toroidal direction (B_t) is produced by the toroidal field (TF) coils wound on the outside of the vacuum vessel. The strength of B_t is expressed as $B_t(R) = B_{t,0}R_0/R$, where R is the major radius of the toroidal plasma from the central axis of the tokamak, and the subscript "0" denotes geometrical center of the plasma. As this equation describes, B_t is stronger on the inboard side than on the outboard side, and hence we call the inboard side "the high-field side" (HFS) and the outboard side "the low-field side" (LFS). However, the toroidal magnetic field alone cannot confine the plasma due to the vertical charge separation caused by the ∇B drift (v_{grad}) and

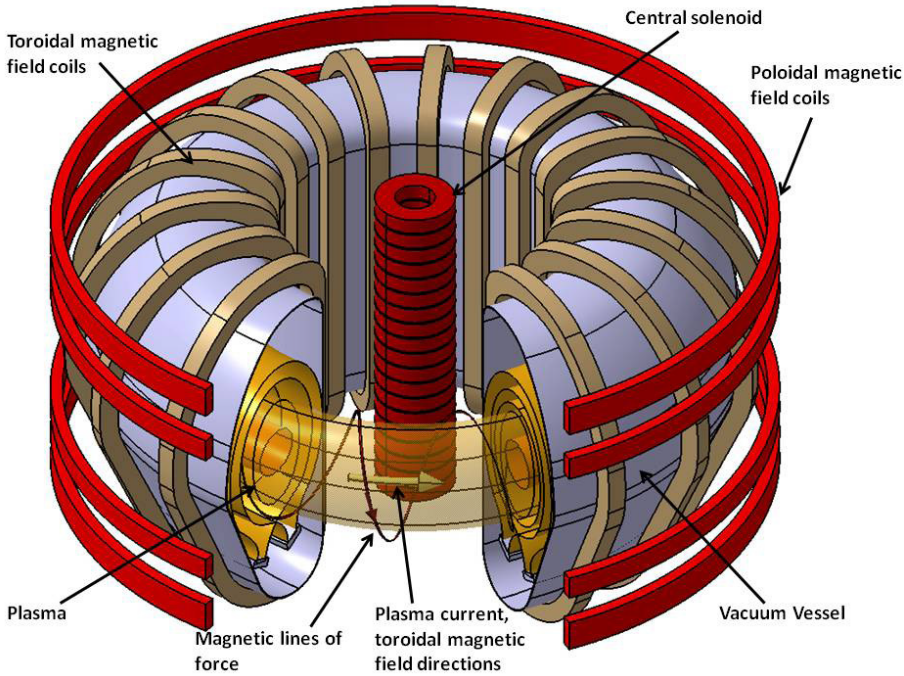

Fig. 1.1: The tokamak [4].

the curvature drift (v_{curv}) [16]

$$\boldsymbol{v}_{\mathrm{grad,s}} + \boldsymbol{v}_{\mathrm{curv,s}} = \frac{T_{\parallel} + T_{\perp}}{q_s} \frac{\boldsymbol{B} \times \boldsymbol{\nabla} B}{B^3}, \tag{1.4}$$

where q is the charge of the particle and the subscript s denotes the particle species, such as electron (e) or ion (i). Hence, electrons and ions move in opposite directions. In order to alleviate the charge separation, the poloidal field (B_{pol}), induced by the plasma current in the toroidal direction (I_{p}), is essential for tokamak confinement. Note that the subscript 'p' denotes 'plasma', not 'poloidal'. The tokamak confines the plasma with nested surfaces traced by the helical magnetic field, $\boldsymbol{B} = \boldsymbol{B}_{\mathrm{t}} + \boldsymbol{B}_{\mathrm{pol}}$.

In the tokamak configuration, the plasma current and the plasma pressure cause toroidal forces directed outwards (the hoop force and the tire tube force) along the major radial direction [2]. In order to establish toroidal force balance, tokamaks are equipped with the poloidal field (PF) coils to generate the external vertical field (B_{v}), which produces an inward restoring force, $\boldsymbol{I}_{\mathrm{p}} \times \boldsymbol{B}_{\mathrm{v}}$. PF coils are located outside the vessel as shown in Fig. 1.1. The needed strength of B_{v} is proportional to I_{p}, and hence B_{v} must be actively controlled. The helical magnetic

field and the plasma current lie on the surface of constant plasma pressure called the flux surface. The plasma is confined where the flux surface is closed, whereas the plasma is lost along magnetic field lines to the wall where the flux surface is open (magnetic field lines intersect the wall). The plasma boundary is called the last closed flux surface (LCFS). The region outside the LCFS is called the scrape-off layer (SOL). In the tokamaks, the plasma boundary is determined either by the protruded material from the wall ('limiter configuration') or the separatrix surface which contains the null point where the poloidal field becomes zero ('divertor configuration').

The ramp-up of I_p is essential for increasing the plasma density. The plasma density is empirically found to be limited by the Greenwald density, n_GW, described in Ref. [17] as

$$n_\mathrm{GW}\ [10^{20}\ \mathrm{m}^{-3}]\ =\ I_\mathrm{p}\ [\mathrm{MA}]/\pi a^2\ [\mathrm{m}^2], \tag{1.5}$$

where a is the horizontal radius of the plasma cross-section, called the minor radius. The Greenwald density is proportional to I_p, and hence the increase of I_p is needed to achieve a high-Q factor. For example, $I_\mathrm{p} = 15$ MA is required for $n = 10^{20}$ m^{-3} to achieve $Q = 10$ on ITER. In addition, the increase of I_p is advantageous for alleviating the orbit losses of high energy electrons and ions, since the orbit depends on the poloidal Larmor radius

$$\rho_{\mathrm{pol},s}\ \equiv\ m_s v_{\parallel,s}/q_s B_\mathrm{pol}, \tag{1.6}$$

where $v_\parallel$ is the component of particle velocity parallel to the magnetic field. The loss of high energy particles occurs when $\rho_{\mathrm{pol},s}$ is large enough so their orbits hit the wall or the limiter. As described by Eq. 1.6, higher B_pol gives smaller $\rho_{\mathrm{pol},s}$. Since B_pol is proportional to I_p, the increase of I_p results in the improvement of confinement of high energy particles.

In most tokamaks, I_p is inductively driven by the toroidal electric field induced by the time-varying current in the central solenoid (CS). For long pulse operation, the plasma current is non-inductively ramped up and sustained using radio frequency (RF) waves or neutral beam injection (NBI). In addition, RF and NBI are also effective for heating the plasma up to 10 keV [12, 18].

Unfortunately, the increase of I_p is not straightforward due to dangerous instabilities which causes a plasma disruption. The instabilities are generally driven in the vicinity of the rational surface of the safety factor, $q = m/n$, where m and n are toroidal and poloidal mode numbers, respectively. The safety factor, equivalent to the number of magnetic field line revolutions in the toroidal direction for one poloidal revolution, is written as

$$q(r)\ =\ rB_\mathrm{t}(r)/R_0 B_\mathrm{pol}(r), \tag{1.7}$$

where r is the minor radius from the plasma center. The tokamak plasmas tend to be stable at high q values ($q(r) > 2$–3 is required for stability), and hence higher B_t is needed to achieve higher I_p. However, since the cost of TF coils is very high, it is preferable to maintain the plasma with lower B_t but at high enough q. To compete with other energy resource, it would be necessary to develop a low cost fusion reactor, for which the spherical tokamak (ST) is a candidate. Because of its special shape, the q value in ST is much higher than that in conventional tokamak under the same values of I_p and B_t, and hence it is possible to achieve higher I_p with lower B_t. A brief description of ST will be presented in the following section.

1.3 Spherical tokamak

The ST is a low aspect ratio tokamak [1, 2]. The aspect ratio (A) is defined as the ratio of the major radius (R_0) to the minor radius (a). The conventional tokamak has aspect ratios of $A > 2$ (typically 3 to 4), whereas the ST has aspect ratios of $A < 2$ (typically 1.5). Typical magnetic configurations of the conventional tokamak and the ST are compared in Fig. 1.2. It is clear that a lower aspect ratio is preferable for obtaining higher q. In addition, the low aspect ratio enables achievement of higher plasma pressures relative to the confining magnetic field pressure, because of the strong intrinsic plasma shaping and the preferable magnetic field line curvature [19]. In the tokamak configuration, the field lines on the inboard side are stable to pressure driven modes, such as the ballooning mode, whereas the field lines on the outboard side are unstable to such modes. In the ST, the length of the field line on the inboard side is much longer than on the outboard side due to its low aspect ratio and strong shaping. Because of these advantages, it is possible to confine a high pressure plasma at a lower magnetic field. Plasma beta (β), defined as the ratio of the plasma pressure to the magnetic field pressure, describes the effectiveness of the magnetic field to confine the plasma. It has been empirically verified that β improves up to 40 % in STs [7, 20, 21]. Note that β is typically only few % in conventional tokamaks.

According to low aspect ratio reactor design studies, it is difficult to install the CS because of the limited space on the inboard side of the device [22, 23]. The high beta discharges above were achieved using the CS. Presently there are no established method or scenario to ramp up the plasma current without the CS. Hence, demonstration of non-inductive plasma start-up (without the CS) is one of the most important issues for the future applications of ST [24, 25]. Some useful and attractive examples of early experiments will be described in the following section.

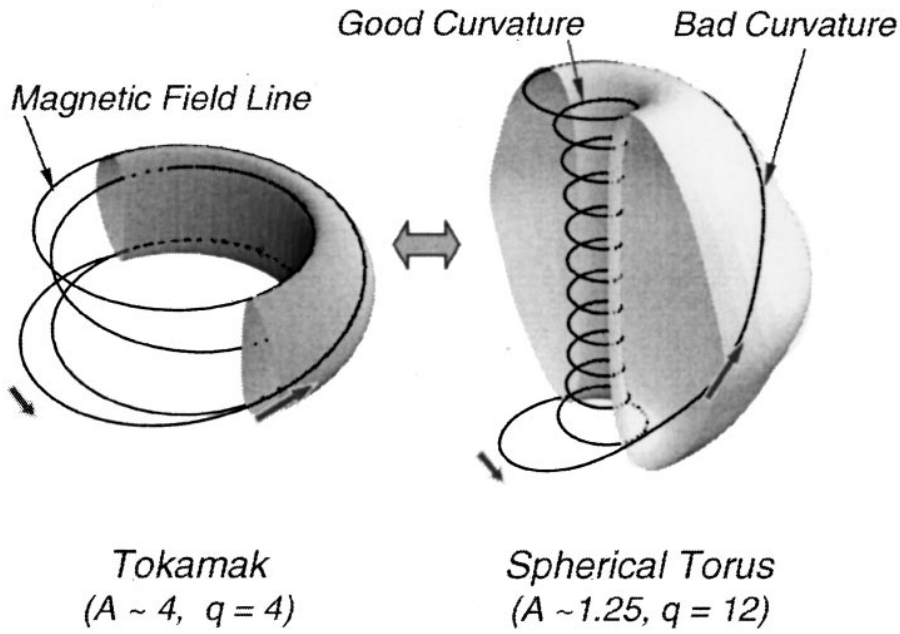

Fig. 1.2: Magnetic configurations of the tokamak (left) and the spherical tokamak (right) [19]. It is clear that the magnetic field line in the good curvature region (inboard side) is much longer than the in the bad curvature region in ST. In addition, high q can be obtained in ST.

1.4 Non-inductive plasma ramp-up

Major methods of non-inductive plasma current ramp-up are:

- Lower Hybrid Wave (LHW)
- Electron Cyclotron Wave (ECW)
- Coaxial Helicity Injection (CHI)
- Neutral Beam Injection (NBI)

In most tokamaks, ECW is used to ionize the gas since ECW can propagate in vacuum and low density plasmas. Absorption of ECW occurs in the vicinity of the EC resonance layer, where $B(R) = 2\pi f m_e/q$. After ionization, LHW or ECW can be used for non-inductive current drive. Ionization by ECW is unnecessary for CHI operation since CHI ionizes the gas itself using a biased electrode in the divertor region. Note that the effective use of NBI is limited to high I_p, where the orbit loss of high energy ions becomes negligible. Also, the plasma must be dense enough to ionize the injected fast neutral particles.

1.4.1 LH current ramp-up

First, early results of plasma current ramp-up experiments using the LHW, the main topic of this thesis, are described. The LHW behaves as an electrostatic wave, and can give momentum to superthermal electrons in the direction of the background magnetic field (parallel or || direction) [26, 27]. The details of LHW theory is described in Chapter 2. Since the superthermal electrons accelerated in the parallel direction are collisionless, and are less likely to be trapped in the weak region of magnetic field, LHCD is a preferred method from the viewpoint of CD efficiency.

The application of LHW to non-inductive current drive was first challenged in conventional tokamaks [28–30]. It is notable that a current ramp-up to 100 kA was achieved using 200 kW of LHW power at 800 MHz in PLT [30]. In this experiment, LHW was launched using a grill antenna (phased array of six waveguides) located on the LFS of the torus. 100 kA was achieved with $N_{\|,0}$ of 2 and 3.5, where $N_{\|,0}$ is the initial parallel refractive index of the LHW. The toroidal field was $B_t \sim 2$ T and the plasma line averaged density was 10^{18} m^{-3}. The mode conversion density, above which the LHW cannot propagate into the plasma core, is approximately 10^{20} m^{-3}, and hence the launched LHW was accessible to the plasma core. The current ramp-up rate was initially 200 kA/sec (30 kA over 130 ms) and subsequently 35 kA/sec (70 kA over 2 sec). Moreover, a successful current ramp-up by the LHW, followed by a transition to the advanced tokamak (AT)

condition using NBI, with a large fraction of the self-driven bootstrap current, was verified in JT-60U [31]. Despite the great achievements in the conventional tokamak, it is believed that the use of LHW for current ramp-up in the ST is difficult due to the high dielectric constant of the plasma. The ST can confine high density plasmas at low B_t, and hence wave reflection near the plasma surface due to mode conversion is a serious problem. It is critically important to find out whether the LHW can be used effectively for current ramp-up in ST.

LH current ramp-up experiments have been performed on the TST-2 spherical tokamak and the Globus-M spherical tokamak [32, 33]. The achieved plasma current is about 20 kA with less than 100 kW of LHW power so far in STs for short pulse discharges around 100 ms used presently. The current ramp-up rate is about 200–300 kA/sec, which is about the same as the initial ramp-up rate observed in PLT. It will be explained throughout this thesis that there are newly revealed essential parameters for higher plasma current in addition to the pulse length.

1.4.2 EC current ramp-up

The ECW is effective not only for ionization, but also for current ramp-up. The mechanism of EC current drive (ECCD) is based on the creation of an asymmetric resistivity from perpendicular acceleration of electrons [4]. The resonance condition is

$$\omega - l|\Omega_e|/\gamma - k_{\parallel}v_{\parallel} = 0, \tag{1.8}$$

where Ω_e is the electron cyclotron frequency, γ is the relativistic mass correction factor, l is the harmonic number, $k_{\parallel}$ is the parallel wavenumber, and $v_{\parallel}$ is the parallel velocity of the electron. Since some accelerated electrons are trapped in the weak region of magnetic field due to perpendicular acceleration, the ECCD efficiency is lower than that of LHCD [27]. The fundamental O-mode ($l = 1$) or second harmonic X-mode ($l = 2$) are widely used for heating and current drive. In addition to the O-mode and X-mode, there is an electrostatic branch called the electron Bernstein wave (EBW), which can be generated via mode conversion of the X-mode near the upper hybrid resonance (UHR) layer. The EBW can give momentum to electrons in the parallel direction like LHCD, and hence it is believed that the CD efficiency of EBW is higher than that of ECW. However, the excitation of EBW is not straightforward due to the presence of the X-mode cutoff layer. The X-mode is inaccessible to the UHR layer in the case of LFS injection, and hence it is necessary to use reflection on the HFS with O-X mode conversion or direct injection of the X-mode from the HFS. For a steep density profile, an effective tunneling of the X-mode to the UHR layer is expected.

EC current ramp-up has been performed on several STs: QUEST [37], LATE [34], MAST [35, 36]. In the QUEST experiment, the plasma current was slowly ramped-up to 54 kA, taking about 0.8 sec, by injecting the O-mode at 28 GHz expecting absorption at the 2nd harmonic layer. The injected power was ~270 kW, and the ramp-up rate was ~100 kA/sec for the initial 20 kA and ~70 kA/sec up to 54 kA. In LATE, 17 kA was achieved by injecting 190 kW of ECW at 5 GHz for a short pulse discharge (~100 ms). The obtained ramp-up rate was 260 kA/sec. In MAST, O-mode was injected from the LFS below the midplane, reflected from a grooved mirror on the HFS to convert to the X-mode, and converted to the EBW near the UHR layer on the LFS. A short pulse experiment (~100 ms) and a long pulse experiment (~450 ms) were performed. In the case of a short pulse discharge, the achieved plasma current was 33 kA by injecting ~100 kW of O-mode wave, and the ramp-up rate was ~200 kA/sec. In the case of a long pulse discharge, the plasma current was successfully ramped up to 73 kA with 60 kW of RF power by optimizing the PF coil current waveform. The ramp-up rate was approximately 170 kA/sec.

1.4.3 CHI current ramp-up

The use of CHI in ST was first suggested in Ref. [38] and conducted on the CDX-U tokamak [39]. Recently, the technique has been optimized for non-inductive start-up and ramp-up on the NSTX spherical tokamak [40–42]. To inject the current into the vessel, the source current in the poloidal direction (injector current, I_{inj}) is induced by electrical break down between the HFS and LFS divertor plates (electrodes). The injector current is trapped by the poloidal field (injector flux) induced by a PF coil located under the divertor. The injector flux stretches into the vessel, and when the Lorentz force of $\boldsymbol{I}_{\mathrm{inj}} \times \boldsymbol{B}_{\mathrm{t}}$ overcomes the field line tension of the injector flux, the stretched flux is helically wound from the inboard side to the outboard side of the divertor.

In the NSTX experiment, the achieved plasma current by CHI was 300–400 kA. The pulse length was only about 3 ms, and hence the ramp-up speed was about 10^5 kA/sec. Instead of steady CHI for long pulse operation, which has not been so successful, they have developed the transient CHI operation to start the plasma with CHI and hand it over to Ohmic operation.

Recently, a new helicity injection technique called the Local Helicity Injection (LHI) has been developed. LHI operation uses the cathode (injector) and the anode installed on the outboard side. In the PEGASUS spherical tokamak, the plasma current was ramped up to 170 kA using LHI in a longer pulse operation (~20 ms) [43].

1.5 Thesis objectives and methods

The main objectives of this research and methods to achieve them are listed below:

- Objective 1: To establish a CS-free I_p ramp-up operation on ST.
- Method: I_p ramp-up experiments using the LHW on TST-2.

In previous experiments on TST-2, it was difficult to achieve high I_p using the grill antenna, widely used in conventional tokamaks. The reason is the input power limitation of around 100 kW imposed by the use of ceramic-loaded waveguides.

- Objective 2: To develop a new type of LHW antenna which can handle higher power to reach higher I_p.
- Method: Applying the combline type traveling wave antenna to excite the LHW with sharp wavenumber spectrum and high directivity.

The combline antenna can be adjusted to 50 Ω input impedance and can be designed to launch the LHW directly using capacitive coupling. We have developed an innovative antenna called the capacitively-coupled combline (CCC) antenna in collaboration with General Atomics.

- Objective 3: To evaluate the utility of LHCD in ST.
- Method: Perform experiments at high/low B_t, density, and I_p to examine the LHW accessibility in ST plasmas.

This research provides the first experimental data to address these issues.

Chapter 2

Theory of Lower Hybrid Wave

2.1 Waves in a cold plasma

In the cold plasma model, ions and electrons are assumed to have zero temperature (no thermal velocity spread) and are collisionless [44]. It is assumed that charge neutrality is satisfied, ion and electron densities are constant, and are immersed in a uniform static magnetic field. The wave equation and the dispersion relation are derived below.

2.1.1 Susceptibility and dielectric tensors

From Maxwell's equations,

$$\frac{1}{\mu_0}\nabla \times \boldsymbol{B} \;=\; \boldsymbol{J} \;+\; \epsilon_0 \frac{\partial \boldsymbol{E}}{\partial t} \;=\; \frac{\partial \boldsymbol{D}}{\partial t}. \tag{2.1}$$

The electric displacement $\boldsymbol{D}$ is written as

$$\boldsymbol{D}(\omega, \boldsymbol{k}) \;=\; \epsilon_0 \boldsymbol{\epsilon}(\omega, \boldsymbol{k}) \boldsymbol{E}(\omega, \boldsymbol{k}) \;=\; \epsilon_0 \boldsymbol{E}(\omega, \boldsymbol{k}) \;+\; \frac{i}{\omega}\boldsymbol{J}(\omega, \boldsymbol{k}) \tag{2.2}$$

after Fourier analysis in space and time. $\boldsymbol{J}$ is the current density and $\boldsymbol{\epsilon}$ is the dielectric tensor

$$\boldsymbol{\epsilon}(\omega, \boldsymbol{k}) \;=\; \mathbf{1} \;+\; \sum_s \chi_s(\omega, \boldsymbol{k}) \tag{2.3}$$

and is expressed using the electron and ion susceptibility tensors χ_s which describe the response of particle species s, such as electron (e) or ion (i). In order to derive the susceptibility under the cold-plasma model, we take into account the

motion of particle species s using the equation of motion. The first-order equation of motion, after Fourier analysis in space and time, can be written as

$$-i\omega m_s \boldsymbol{v}_s = q_s (\boldsymbol{E} + \boldsymbol{v}_s \times \boldsymbol{B}) . \tag{2.4}$$

Note that $q_\mathrm{e} = -e$ and $q_\mathrm{i} = Z_\mathrm{i} e$ in this convention. The fluid stress tensor is assumed to be zero in the cold-plasma assumption.

When the static magnetic field is directed along the z-direction ($\boldsymbol{B}_0 = B_0 \hat{\boldsymbol{z}}$), and the velocity and the electric field are expressed using the left hand and right hand rotating components, $v^\pm = (v_x \pm i v_y)/2$, $E^\pm = (E_x \pm i E_y)/2$, the velocity for species s can be written as

$$v_s^\pm = \frac{i q_s}{m_s} \frac{E^\pm}{\omega \mp \Omega_s}, \tag{2.5}$$

$$v_{zs} = \frac{i q_s}{m_s} \frac{E_z}{\omega}, \tag{2.6}$$

where $\Omega_s = q_s B_0 / m_s$ is the cyclotron frequency ($\Omega_i > 0$, $\Omega_e < 0$). The current density is written as

$$\boldsymbol{J} = \sum_s \boldsymbol{J}_s = \sum_s n_s q_s \boldsymbol{v}_s . \tag{2.7}$$

From Eqs. (2.2) and (2.7), the susceptibility can be expressed using the particle velocity,

$$\boldsymbol{J}_s = n_s q_s \boldsymbol{v}_s = -i\omega\epsilon_0 \chi_s \boldsymbol{E} . \tag{2.8}$$

The susceptibility tensor components are derived by substituting Eqs. (2.5) and (2.6) into Eq. (2.8),

$$\chi_s^\pm = -\frac{\omega_{ps}^2}{\omega(\omega \mp \Omega_s)}, \tag{2.9}$$

$$\chi_{xx,s} = \chi_{yy,s} = \frac{\chi_s^+ + \chi_s^-}{2}, \tag{2.10}$$

$$\chi_{xy,s} = -\chi_{yx,s} = \frac{i(\chi_s^+ - \chi_s^-)}{2}, \tag{2.11}$$

$$\chi_{zz,s} = -\frac{\omega_{ps}^2}{\omega^2}, \tag{2.12}$$

where ω_{ps} is the plasma frequency for species s ($\omega_{ps}^2 = n_s q_s^2/\epsilon_0 m_s$). When these susceptibility components are substituted into Eq. (2.3), the cold-plasma dielectric tensor $\boldsymbol{\epsilon}$ can be expressed as

$$\boldsymbol{\epsilon} \cdot \boldsymbol{E} = \begin{pmatrix} S & -iD & 0 \\ iD & S & 0 \\ 0 & 0 & P \end{pmatrix} \begin{pmatrix} E_x \\ E_y \\ E_z \end{pmatrix}. \tag{2.13}$$

S (for sum), D (for difference), P (for plasma) are called Stix parameters [44] which are defined as

$$S = \frac{R + L}{2}, \tag{2.14}$$

$$D = \frac{R - L}{2}, \tag{2.15}$$

$$R = 1 + \sum_s \chi_s^- = 1 - \sum_s \frac{\omega_{ps}^2}{\omega(\omega + \Omega_s)}, \tag{2.16}$$

$$L = 1 + \sum_s \chi_s^+ = 1 - \sum_s \frac{\omega_{ps}^2}{\omega(\omega - \Omega_s)}, \tag{2.17}$$

$$P = 1 + \sum_s \chi_{zz,x} = 1 - \sum_s \frac{\omega_{ps}^2}{\omega^2}. \tag{2.18}$$

2.1.2 Wave equation and dispersion relation

Faraday's law

$$\nabla \times \boldsymbol{E} = -\frac{\partial \boldsymbol{B}}{\partial t} \tag{2.19}$$

and Eq. (2.1) can be combined to derive the homogeneous plasma wave equation

$$\boldsymbol{N} \times (\boldsymbol{N} \times \boldsymbol{E}) + \boldsymbol{\epsilon} \cdot \boldsymbol{E} = 0 \tag{2.20}$$

where $\boldsymbol{N}$ is the refractive index vector, $\boldsymbol{N} \equiv c\boldsymbol{k}/\omega = c/\boldsymbol{v}_{\mathrm{ph}}$, which is the ratio of the velocity of light to the wave phase velocity ($\boldsymbol{v}_{\mathrm{ph}}$). Choosing the coordinate system so that $\boldsymbol{B}_0 = (0, 0, B_0)$ and $\boldsymbol{N} = (N \sin\theta, 0, N \cos\theta)$, the wave equation can be rewritten as

$$\begin{pmatrix} S - N^2\cos^2\theta & -iD & N^2\cos\theta\sin\theta \\ iD & S - N^2 & 0 \\ N^2\cos\theta\sin\theta & 0 & P - N^2\sin^2\theta \end{pmatrix} \begin{pmatrix} E_x \\ E_y \\ E_z \end{pmatrix} = 0. \tag{2.21}$$

If the determinant of the matrix multiplying the electric field vector is zero, a finite amplitude electric field solution can exist. In this case, the cold-plasma dispersion relation is expressed as

$$AN^4 - BN^2 + C = 0, \tag{2.22}$$

where

$$\begin{aligned} A &= S\sin^2\theta + P\cos^2\theta, \\ B &= RL\sin^2\theta + PS(1 + \cos^2\theta), \\ C &= PRL. \end{aligned} \tag{2.23}$$

One expression for the solutions of the dispersion relation is

$$N^2 = \frac{B \pm \sqrt{(RL - PS)^2\sin^4\theta + 4P^2D^2\cos^2\theta}}{2A}. \tag{2.24}$$

Another expression is

$$\tan^2\theta = \frac{-P(N^2 - R)(N^2 - L)}{(SN^2 - RL)(N^2 - P)}. \tag{2.25}$$

The expression for the perpendicular refractive index ($N_\perp$) is useful when a the value of the parallel refractive index ($N_\parallel$) is known. The dispersion relation expressed for the perpendicular refractive index is

$$aN_\perp^4 - bN_\perp^2 + c = 0 \tag{2.26}$$

where

$$\begin{aligned} a &= S, \\ b &= RL + PS - N_\parallel^2(P + S), \\ c &= P(RL - 2SN_\parallel^2 + N_\parallel^4). \end{aligned} \tag{2.27}$$

The perpendicular refractive index is derived as

$$N_\perp^2 = \frac{b \pm F}{2a}, \tag{2.28}$$

where $F = \sqrt{b^2 - 4ac}$. This equation indicates that two branches (solutions) exist under proper parameters. The wave with slower phase velocity is called the slow wave, and the faster one is called the fast wave.

2.2 Landau damping

Landau damping occurs when the charged particle velocity is close to the wave phase velocity [44, 45]. In order to explain Landau damping mathematically, we consider only longitudinal oscillations of the electric field, $\boldsymbol{k} \parallel \boldsymbol{E}$, in the absence of magnetic field. The equation of motion for a single particle with velocity $\boldsymbol{v} = \hat{\boldsymbol{z}}v$ can be written as

$$\begin{aligned} \boldsymbol{E} &= \hat{\boldsymbol{z}}E\cos(kz - \omega t), \\ m\frac{dv}{dt} &= qE\cos(kz - \omega t). \end{aligned} \tag{2.29}$$

The zeroth-order solution to Eq. (2.29) is

$$z = v_0 t + z_0, \tag{2.30}$$

where v_0 is the initial velocity and z_0 is the initial position of the particle. The first-order equation of motion is obtained by substituting Eq. (2.30) into Eq. (2.29),

$$m\frac{dv_1}{dt} = qE\cos(kz_0 + kv_0 t - \omega t), \tag{2.31}$$

where v_1 is the first-order velocity of the particle induced by the wave. This equation can be solved with the initial value of $v_1 = 0$ at $t = 0$ as

$$v_1 = \frac{qE}{m}\frac{\sin(kz_0 + kv_0 t - \omega t) - \sin(kz_0)}{kv_0 - \omega}. \tag{2.32}$$

The rate of increase of the kinetic energy averaged over initial positions z_0 is

$$\left\langle \frac{d}{dt}\frac{mv^2}{2} \right\rangle_{z_0} = \frac{q^2E^2}{2m}\left[-\frac{\omega\sin(\alpha t)}{\alpha^2} + t\cos(\alpha t) + \frac{\omega t\cos(\alpha t)}{\alpha} \right], \tag{2.33}$$

where $\alpha = kv_0 - \omega$. This is further averaged over the distribution of initial velocities v_0

$$f(v_0) = f\left(\frac{\alpha + \omega}{k}\right) = g(\alpha) \tag{2.34}$$

to yield

$$\left\langle \frac{d}{dt}\frac{mv^2}{2} \right\rangle_{z_0, v_0} = -\frac{\pi\omega q^2E^2}{2m|k|}P\int_{-\infty}^{\infty} d\alpha \frac{g(\alpha)\sin(\alpha t)}{\alpha^2}. \tag{2.35}$$

Expanding $g(\alpha)$ in the vicinity of $\alpha = 0$ as

$$g(\alpha) = g(0) + \alpha g'(0) + \frac{\alpha^2}{2}g'' + \cdots, \tag{2.36}$$

Eq. (2.35) can be approximated as

$$\left\langle \frac{d}{dt}\frac{mv^2}{2} \right\rangle_{z_0,v_0} = -\frac{\pi\omega q^2 E^2}{2m|k|}\left[\frac{df(v_0)}{dv_0}\right]_{v_0=\frac{\omega}{k}}. \tag{2.37}$$

From this equation, energy transfer from the wave to the particle occurs if the derivative of the distribution function at $v_0 = \omega/k$ is negative, meaning there are more particles moving slightly slower than the wave than slightly faster than the wave.

2.3 Theory of LHW

2.3.1 Dispersion relation

The dispersion relation for the LHW can be derived from the cold-plasma dispersion relation [4]. The frequency range for LHW is $\Omega_\mathrm{i} \ll \omega \ll |\Omega_\mathrm{e}|$, and Stix parameters can be approximated as

$$\begin{aligned} S &\sim 1 + \frac{\omega_\mathrm{pe}^2}{\Omega_e^2} - \frac{\omega_\mathrm{pi}^2}{\omega^2}, \\ P &\sim 1 - \frac{\omega_\mathrm{pe}^2}{\omega^2}, \\ D &\sim \frac{\omega_\mathrm{pe}^2}{\omega\Omega_e}. \end{aligned} \tag{2.38}$$

In general, the parallel refractive index of the wave induced by an antenna ($N_{\|,0}$) is determined by the antenna geometry and would be conserved in the limit of a straight tokamak (infinite aspect ratio). Hence, it is convenient to consider the variation of $N_\perp$ for a fixed $N_\| \approx N_{\|,0}$. From Eq. (2.28), the two branches are described by

$$N_{\perp,\,\mathrm{s}}^2 \approx -\frac{P(N_\|^2 - S) + D^2}{S}, \tag{2.39}$$

$$N_{\perp,\,\mathrm{f}}^2 \approx \frac{D^2 - (N_\|^2 - S)^2}{(N_\|^2 - S) + D^2/P}. \tag{2.40}$$

The slow branch, $N_{\perp,\,\mathrm{s}}^2$, is the LHW and the fast branch, $N_{\perp,\,\mathrm{f}}^2$, is the fast wave (FW). Note that in this dispersion relation for LHW there is a finite electromagnetic contribution. Wave propagation, accessibility and mode conversion can be calculated from the dispersion relation. The polarization can be derived by substituting the refractive index into the wave equation.

In order to obtain simplified dispersion relations for the LHW, we consider the low density case and the high density case separately. In the low density edge plasma, the Stix parameters become $S \cong 1$, $|D| \ll 1$, and $RL \cong 1$, so

$$\left[N_\perp^2 - P(1 - N_\parallel^2)\right]\left[N_\perp^2 - (1 - N_\parallel^2)\right] = 0. \tag{2.41}$$

The left side of this equation shows a propagating mode for $P < 0$ and $N_\parallel^2 > 1$,

$$N_\perp^2 = P(1 - N_\parallel^2). \tag{2.42}$$

When the wave propagates into the high density plasma core, $N_\perp^2$ becomes larger than P, R, L, RL/S substantially, and we can derive the high density dispersion relation from Eq. (2.25),

$$\tan^2\theta = -P/S. \tag{2.43}$$

This equation indicates the resonance cone [46]: the wave vector lies on the cone determined by plasma parameters. It can be rewritten in terms of refractive index components,

$$SN_\perp^2 + PN_\parallel^2 = 0. \tag{2.44}$$

It can also be rewritten as

$$\omega = \omega_{\mathrm{LH}}\left(1 + \frac{k_\parallel^2}{k_\perp^2}\frac{m_\mathrm{i}}{m_\mathrm{e}}\right)^{1/2}, \tag{2.45}$$

where ω_{LH} is the lower-hybrid-resonance frequency,

$$\omega_{\mathrm{LH}}^2 = \frac{\omega_{\mathrm{pi}}^2}{1 + \omega_{\mathrm{pe}}^2/\Omega_\mathrm{e}^2}. \tag{2.46}$$

The high density dispersion relation can be derived using the electrostatic approximation. Under this approximation, the electric field can be expressed as a gradient of the electrostatic potential,

$$\boldsymbol{E} = -\nabla\phi = -i\boldsymbol{k}\phi. \tag{2.47}$$

We can solve the wave equation, Eq. (2.20) by substituting this expression and multiplying by $\boldsymbol{k}$ from the left,

$$\begin{pmatrix} k_\perp & 0 & k_\parallel \end{pmatrix}\begin{pmatrix} S & 0 & 0 \\ 0 & S & 0 \\ 0 & 0 & P \end{pmatrix}\begin{pmatrix} k_\perp \\ 0 \\ k_\parallel \end{pmatrix} = 0. \tag{2.48}$$

The dispersion relation for the LHW obtained under the electrostatic approximation, $Sk_\perp^2 + Pk_\parallel^2 = 0$, is the same as Eq. (2.43).

2.3.2 Wave propagation

Accessibility

A reflection of the LHW or the FW occurs when the wave reaches the cut off layer where $N_\perp \to 0$, and conversion between the LHW and the FW occurs when the wave reaches the mode conversion layer where $N^2_{\perp,\mathrm{s}} = N^2_{\perp,\mathrm{f}}$. If the LHW reaches the LH resonance density, the wavenumber becomes infinite under the cold-plasma approximation. When we introduce the finite ion Larmor radius effect, mode conversion from the LHW to the ion plasma waves occurs. Since the ion plasma wave is quickly absorbed by ions, it would not contribute to current drive. Hence, the density of the target plasma should be higher than the cut off density, but lower than the LHW-FW mode conversion density.

According to Eq. (2.26), the cut off densities for the LHW, n_s, and for the FW, n_f, can be derived from $c = 0$

$$\omega^2_{\mathrm{pe}} = \omega^2, \tag{2.49}$$

$$\omega^2_{\mathrm{pe}} = (N^2_\parallel - 1)\omega|\Omega_e|. \tag{2.50}$$

The cut off for the LHW occurs when $P = 0$. If $N_\parallel$ is small enough for F in Eq. (2.28) becomes zero, the LHW propagating from the low density side mode converts to the FW, or from the FW to the LHW (Fig. 2.1 left). The critical density where n^+_e becomes equal to n^-_e is given by

$$\omega_{\mathrm{pi}}/\omega = N_\parallel\hat{\omega} \pm [1 + N^2_\parallel(\hat{\omega}^2 - 1)]^{1/2}, \tag{2.51}$$

where $\hat{\omega} = \omega/(|\Omega_e|\Omega_i)^{1/2}$ and $n^+_e > n^-_e$. If $N_\parallel$ is large enough for$F$ to be positive, the LHW and the FW mode coalescence never occurs [47] (Fig. 2.1 right). When $\hat{\omega}^2 < 1$ and $(\omega_{\mathrm{pi0}}/\omega)^2 > \hat{\omega}^2/(1-\hat{\omega}^2)$, Eq. (2.51) is rewritten as

$$N^2_\parallel \geq \frac{1}{1-\hat{\omega}^2}, \tag{2.52}$$

Which is the relationship of accessibility to the LH resonance, first obtained in Ref. [48] (Fig. 2.1). The subscript “0" denotes the value at the maximum plasma density. The right hand side of this equation is greater than one, and hence the wave must have be a slow wave with $|N_\parallel| > 1$ [49]. When $\hat{\omega}^2 > 1$ or $\hat{\omega}^2 < 1$ and $(\omega_{\mathrm{pi0}}/\omega)^2 < \hat{\omega}^2/(1-\hat{\omega}^2)$, we can derive the accessibility condition to the plasma interior as

$$N^2_\parallel \geq \frac{\omega_{\mathrm{pe0}}}{|\Omega_{\mathrm{e0}}|} + S_0^{1/2}. \tag{2.53}$$

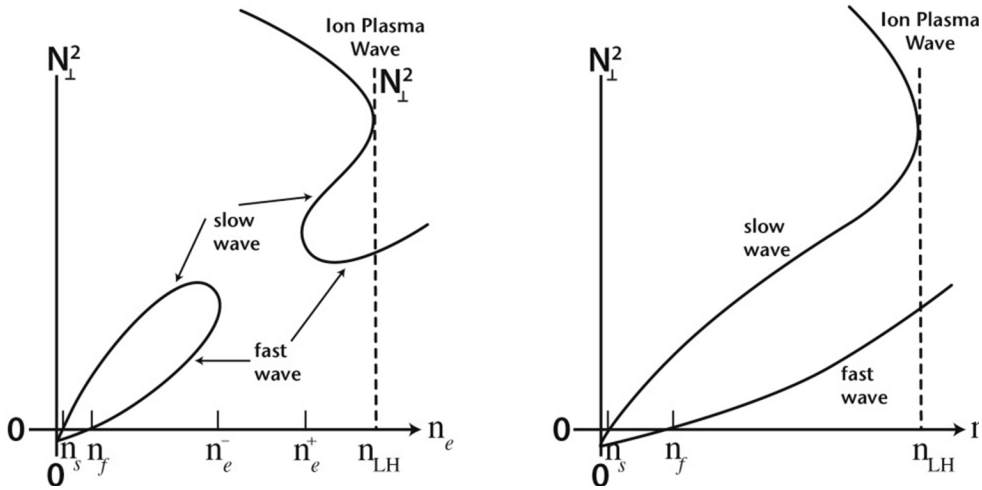

Fig. 2.1: Accessibility diagram for the LHW. $n_\mathrm{s} < n_\mathrm{e} < n_\mathrm{e}^-$ (left) or $n_\mathrm{s} < n_\mathrm{e} < n_\mathrm{LH}$ (right) are regions where the LHW can propagate from the low density plasma edge [4].

Group velocity

In order to consider the direction of energy flow (ray direction) of the LHW, the group velocity is introduced. In an anisotropic media, the direction of the ray is different from that of the wave vector, $\boldsymbol{k}$. The ray direction is along the group velocity,

$$\boldsymbol{v}_\mathrm{g} = \frac{d\boldsymbol{r}}{dt} = \frac{\partial\omega(\boldsymbol{k})}{\partial\boldsymbol{k}}. \tag{2.54}$$

We can obtain the group velocity from the LHW dispersion relation, Eq. 2.45. The ratio of the parallel group velocity, $v_{\mathrm{g},\|}$, to the perpendicular group velocity, $v_{\mathrm{g},\perp}$, can be expressed as

$$\frac{v_{\mathrm{g},\|}}{v_{\mathrm{g},\perp}} = \frac{-k_\perp}{k_\|} = \frac{v_{\mathrm{ph},\|}}{-v_{\mathrm{ph},\perp}} = \mp\left(-\frac{P}{S}\right)^{1/2}, \tag{2.55}$$

where Eq. (2.43) was used. Note that the ratio of the group velocity components depends only on plasma parameters. In the plasma core, $|P| \gg S$, and hence $|v_{\mathrm{g},\|}| \gg |v_{\mathrm{g},\perp}|$, $|v_{\mathrm{ph},\|}| \gg |v_{\mathrm{ph},\perp}|$, and $|k_\|| \ll |k_\perp|$. In this region, the group velocity and the wave vector are perpendicular to each other ($\boldsymbol{v}_\mathrm{g} \cdot \boldsymbol{k} = 0$). The parallel phase velocity and the parallel group velocity are in the same direction.

Up-shift and down-shift

In the toroidal geometry, the toroidal mode number, n, is conserved but the poloidal mode number, m, is not conserved [47, 50]. The toroidal mode number is determined by the initial major radius, R_{i}, and the initial wavenumber, $k_{\parallel,0}$, where the wave is launched,

$$n = k_{\parallel,0} R_{\mathrm{i}}. \tag{2.56}$$

The poloidal mode number varies as [50]

$$\frac{\mathrm{d}m}{\mathrm{d}\theta} \simeq -k_{\parallel} R_0 q(\rho) \left(1 + \frac{\omega_{\mathrm{pe}}^2/\Omega_{\mathrm{e}}^2}{S} \frac{\rho}{R_0} \sin\theta \right) \tag{2.57}$$

where θ is the poloidal angle, $\rho = r/a$ is the normalized radius, and $q(\rho) = (\rho/R_0) B_0/B_\theta(\rho)$ is the safety factor. The parallel wavenumber can be expressed as

$$k_{\parallel} = \frac{1}{B} \left[\frac{m}{\rho} B_\theta + \frac{n}{R} B_\phi \right], \tag{2.58}$$

where ϕ is the toroidal angle. The parallel wavenumber undergoes up-shift or down-shift during propagation. Note that up-shift (increase of $|N_{\parallel}|$) occurs for $0 \leq \theta \leq \pi$ in TST-2 because $k_{\parallel,0} < 0$.

2.4 Absorption by electron Landau damping

It is important to investigate the optimum $N_{\parallel}$ of the LHW for absorption in the core plasma by electron Landau damping. In the case of a Maxwellian velocity distribution for electrons, significant electron Landau damping occurs when $v_{\mathrm{ph},\parallel} \sim 3v_{\mathrm{th,e}}$ [26, 51]. When quasi-linear evolution of the electron distribution function is taken into account, the condition for significant Landau damping becomes $v_{\mathrm{ph},\parallel} \sim 2.3v_{\mathrm{th,e}}$ [47]. In general, the electron temperature peaks at the center of the plasma. Hence, if we aim for absorption near the plasma center, $N_{\parallel}$ should satisfy

$$v_{\mathrm{ph},\parallel} \leq 3v_{\mathrm{th,e}} \tag{2.59}$$

in the plasma core.

The damping rate can be derived from the LHW dispersion relation by adding an imaginary part to describe Landau damping. The equation is expressed as

$$S \frac{k_\perp^2}{k^2} + P \frac{k_\parallel^2}{k^2} + i\varepsilon_{\mathrm{Im}} = 0, \tag{2.60}$$

where

$$\varepsilon_{\mathrm{Im}} = \frac{\sqrt{\pi}}{k^2\lambda_D^2}\frac{\omega}{k_{\parallel}v_{\mathrm{th,e}}}\exp\left(-\frac{\omega^2}{k_{\parallel}^2 v_{\mathrm{th,e}}^2}\right), \tag{2.61}$$

and $\lambda_D^2 = v_{\mathrm{th,e}}^2 \,/\, 2\omega_{\mathrm{pe}}^2$, and $v_{,e} = \sqrt{2T_e \,/\, m_e}$ is the electron thermal velocity. From Eq. (efeq:lamdaudisper), the relationship between the imaginary part of $k_\perp$ and the real part of $k_\perp$ is derived as

$$\frac{\Im k_\perp}{\Re k_\perp} = -\sqrt{\pi}\frac{\omega^3}{k_{\parallel}^3 v_{th,e}^3}\exp\left(-\frac{\omega^2}{k_{\parallel}^2 v_{th,e}^2}\right). \tag{2.62}$$

Equation (2.62) yields the condition to obtain sufficient absorption by electron Landau damping

$$N_{\parallel}\sqrt{T_e} \geq 5\text{–}7, \tag{2.63}$$

where T_e is in keV.

2.5 Parametric decay instability

The parametric decay instability (PDI) has been observed during LHW heating and current drive experiments on several Tokamaks [52, 53]. The theory of PDI relevant to RF heating in the LH frequency range is presented in Ref. [54, 55]. According to a review study of PDI, the loss by PDI becomes important when $\omega \leq 2\omega_{\mathrm{lh}}$. The physical mechanism of PDI is based on three-wave coupling among the incoming pump wave (ω_0, $\boldsymbol{k}_0$), the low frequency mode (ω_1, $\boldsymbol{k}_1$), and the lower sideband wave (ω_2, $\boldsymbol{k}_2$). These frequencies and wavenumbers satisfy the relationship

$$(\omega_0, \boldsymbol{k}_0) \rightarrow (\omega_1, \boldsymbol{k}_1) \;+\; (\omega_2, \boldsymbol{k}_2).$$

For LHCD, there is a suitable wavenumber to drive the current effectively. Hence, the change of the wavenumber by PDI generally leads to undesirable power losses.

An example is decay to the low-frequency ion-cyclotron quasi-mode (ICQM) and the sideband LHW. The quasi-mode is not a wave that satisfies the linear dispersion relation, and is strongly damped by ion-cyclotron harmonic damping ($\omega = n\Omega_{\mathrm{i}}$). Therefore, $\epsilon_{\mathrm{Re}}(\omega) \neq 0$. The lower sideband wave satisfies $\epsilon_{\mathrm{Re}}(\omega^-) = 0$ while the upper sideband is nonresonant $\epsilon_{\mathrm{Re}}(\omega^+) \neq 0$. For the ICQM PDI, the relationship among the pump wave, the low frequency ICQM, and the lower sideband LHW is

$$(\omega_0, \boldsymbol{k}_0) \rightarrow (n\Omega_{\mathrm{i}}, \boldsymbol{k}) \;+\; (\omega^-, \boldsymbol{k}^-).$$

Chapter 3

TST-2

3.1 TST-2 configuration and parameters

TST-2 (Tokyo Spherical Tokamak-2) is a spherical tokamak at the University of Tokyo (Fig. 3.1(a)) [24] with plasma major radius $R_0 \simeq 0.36 - 0.38$ m, minor radius $a \simeq 0.23$–0.25 m, and aspect ratio $A = R_0/a \simeq 1.5$–1.6. The toroidal magnetic field strength, induced by 24 turns of toroidal field (TF) coils, is $B_t \leq 0.3$ T for short pulse operation ($\sim$ 40 ms) or $B_t \leq 0.12$ T for long pulse operation ($\sim$ 100 ms). Three types of PF coils (PF1, PF2, PF3) are equipped to provide force balance along the major radius R and to control the plasma shape. The current in the PF coil for the main vertical field B_v, either PF3 alone or PF1, PF2, and PF3 in series, is controlled by an IGBT switching system. The plasma vertical position along z is controlled by the horizontal coil (H coil). In non-inductive start-up operation using the LHW, it takes 60–100 ms to ramp up the plasma current, and hence the long pulse operation is used. In these experiments, deuterium gas was injected just before preionization by ECW. It was discovered that ECW can also be used for density suppression. TST-2 is equipped with a variety of diagnostics to measure plasma parameters. The line-integrated electron density is measured using microwave interferometers along vertical and horizontal chords. Thomson scattering system on TST-2 has been improved to measure the electron temperature and density profiles in very low density plasmas in the range $10^{16-18}\mathrm{m}^{-3}$ by accumulating data from several shots. The poloidal magnetic flux profile is reconstructed from magnetic data obtained by flux loops, saddle loops, and magnetic coils using the equilibrium fitting code EFIT [56].

TST-2 is equipped with a slim CS for inductive current drive. The obtained current in the short-pulse inductive operation is up to 120 kA, and the electron temperature is in the range 100–400 eV.

(a)

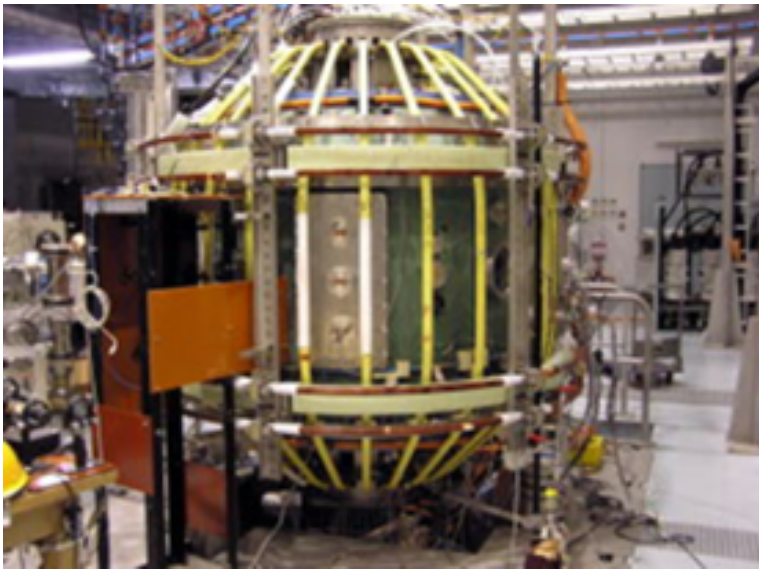

(b)

Fig. 3.1: (a) Photograph of TST-2. (b) 200 MHz RF power amplifier system consisting of four sub-systems with 100 kW output each.

3.2 LHW system

The 200 MHz RF amplifier system (Fig. 3.1(b), 3.2)was installed in 2007, and it has contributed to non-inductive start-up experiments on TST-2. In this system, there are four parallel sub-systems of amplifier chain with an output power of up to 100 kW each. The RF wave at a frequency of 200 MHz is generated by the signal generator (SG) and amplified by the pre-amplifier and the excite-amplifier. The power divider is used to split the RF power into four channels and the balance attenuators equalize the power for the four sub-systems. The phase shifter is used to optimize the combined power of two channels, or to adjust $N_{\|}$ of the LHW excited by the grill antenna. The intermediate power amplifiers (IPA) increase the RF power up to 25 kW, and the final power amplifiers (FPA) increase the RF power up to 100 kW for each sub-system. The circulators are equipped to avoid damage to the FPA by the reflected RF power from the antenna. The reflected RF power is diverted to the dummy load and is absorbed. The number of RF transmission lines depends on the antenna design. For the combline-type antenna, the outputs of two sub-systems are combined using a 180 degree hybrid coupler, and the maximum combined RF power is 200 kW (Fig. 3.3). The RF power is fed into the input side of the combline antenna, and the transmitted wave is absorbed by the dummy load connected to the output side of the antenna. For the grill antenna, four RF transmission lines are used to feed the four waveguides separately (Fig. 3.4).

3.3 LHW propagation in TST-2

As described in Chapter 2, the propagation region for the LHW is limited on the low density side by the cutoff density (where $P = 0$), and on the high density side by the mode conversion density (where $F = 0$). The accessible region for TST-2 parameters is plotted for 200 MHz and $N_{\|} = -2,\ -5,\ -10$ in Fig. 3.5. The LHW is accessible where the density is higher than the cutoff density ($\approx 5 \times 10^{14}$ m^{-3}, shown by the blue dashed line), and is lower than the mode conversion density (shown by the black solid lines for three cases of $N_{\|}$). The LHW accessibility to higher densities improves when $|N_{\|}|$ is higher. The magnetic field strength and the line-averaged density are typically 0.12 T and 10^{17}–10^{18} m^{-3} for LHW operation on TST-2. The edge density around the LCFS is 10^{15}–10^{16} m^{-3}, which is higher than the cutoff density. Hence, $|N_{\|}| \geq 5$ is preferable from the point of view of accessibility. According to the review studies on PDI, absorption by ions becomes non-negligible when $2\omega_{\mathrm{lh}} > \omega$ (shown by the red dashed line). To avoid reaching the mode conversion density, increasing the toroidal magnetic field by upgrading the TF power supply helps, but there is an upper density limit due to PDI.

$N_{\perp}^2$ of the SW (or the LHW, black solid line) and the FW (red dash line) are

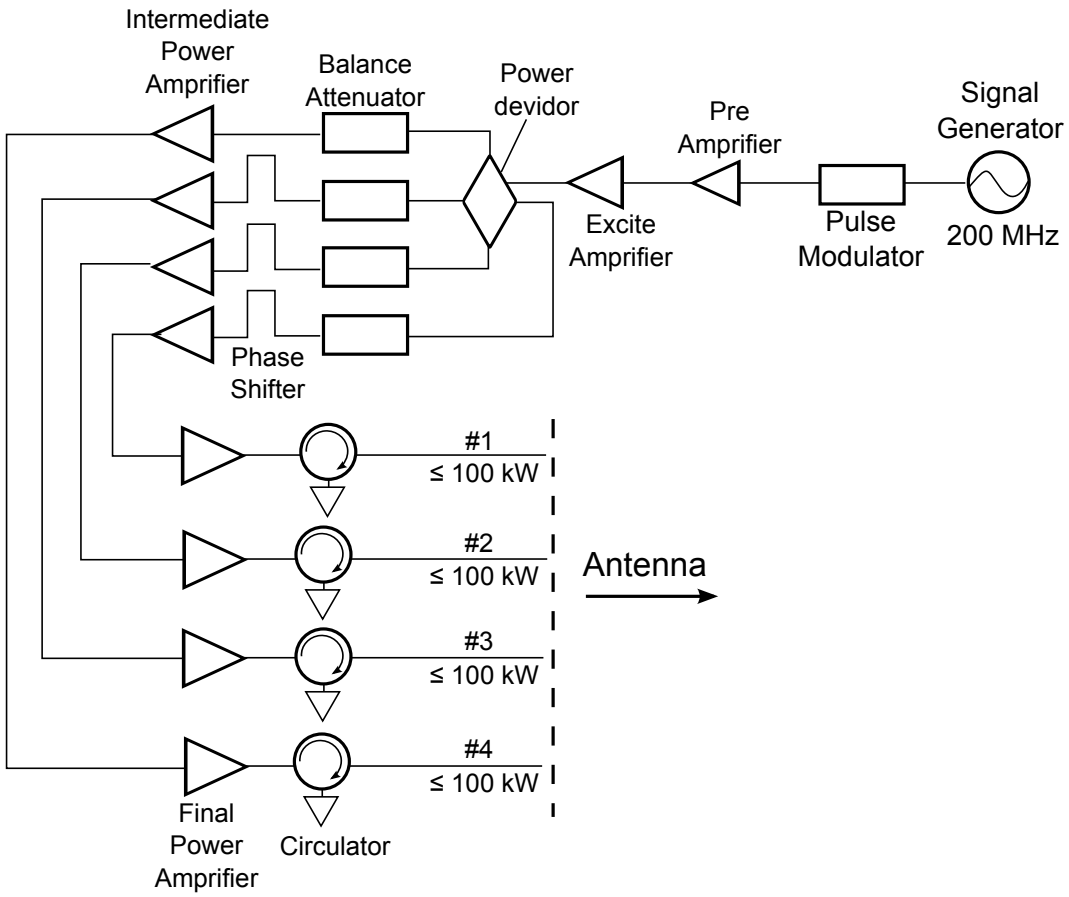

Fig. 3.2: Block diagram of the 200 MHz RF power amplifier system. The number of RF transmission lines depends on the antenna design.

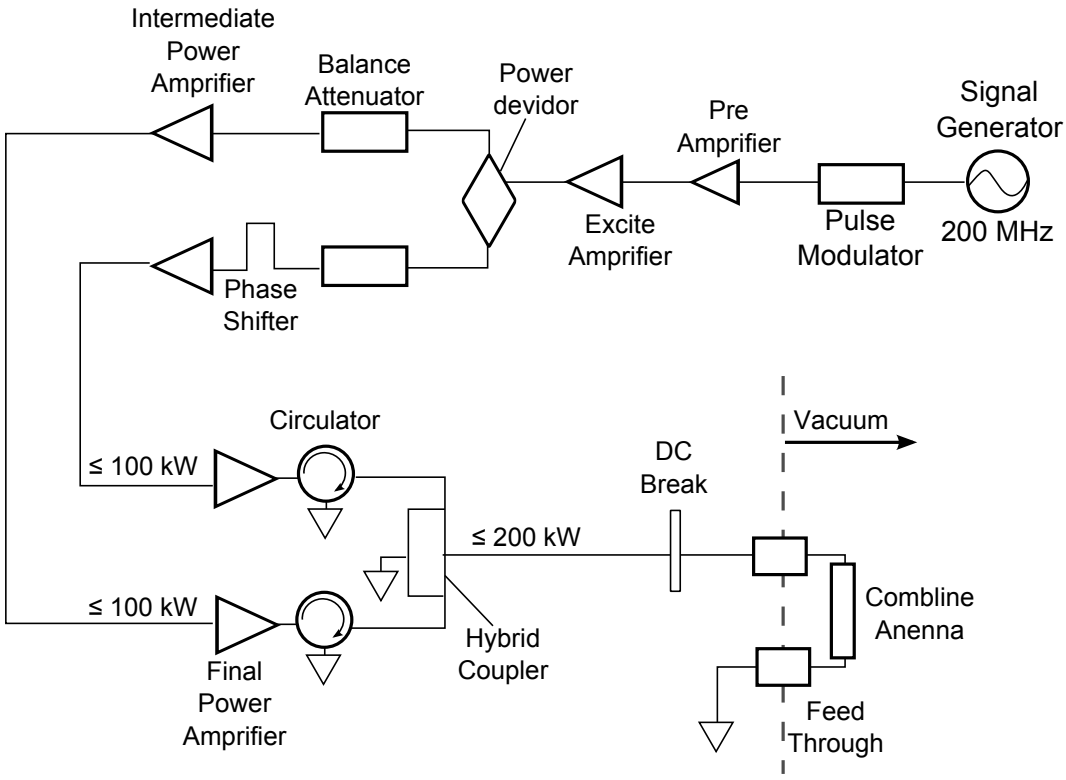

Fig. 3.3: Block diagram for the combline-type antenna.

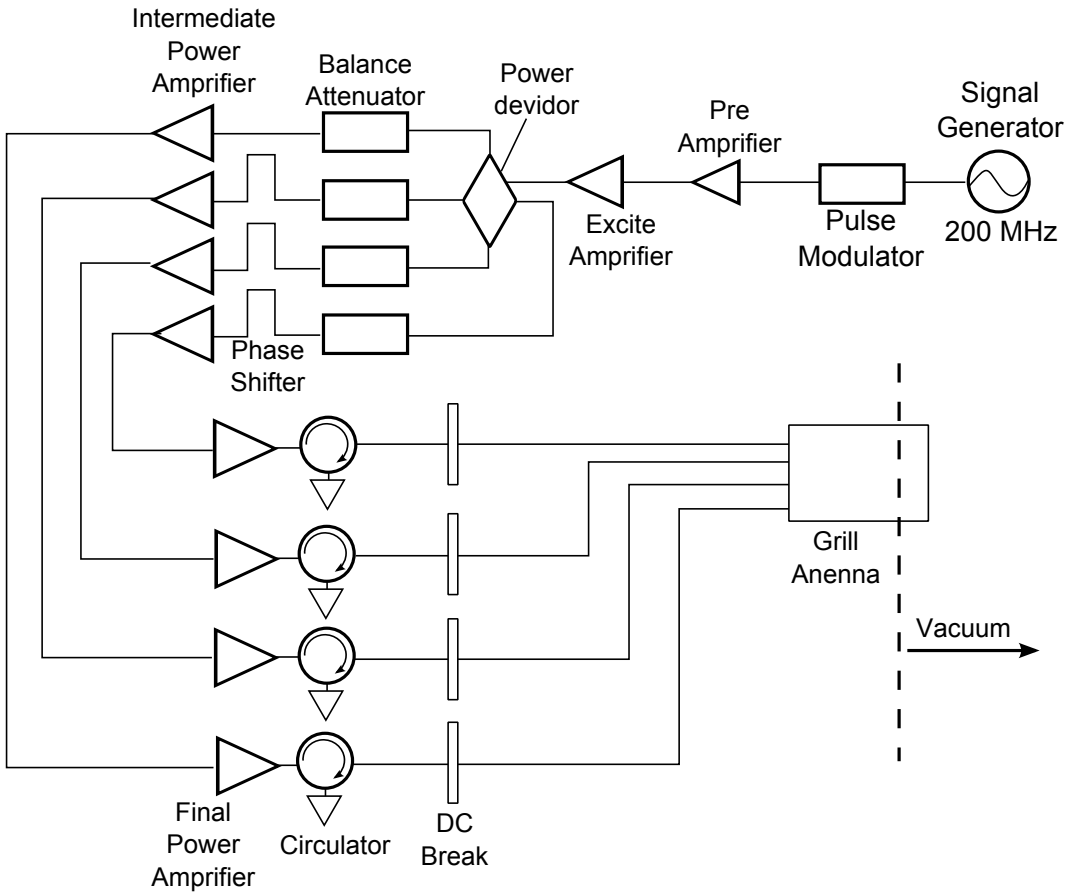

Fig. 3.4: Block diagram for the grill antenna.

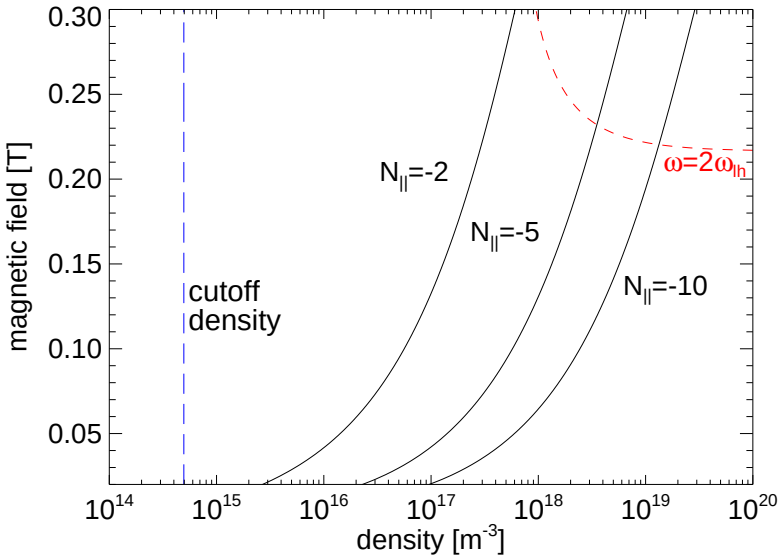

Fig. 3.5: Accessible region of the LHW for TST-2 parameters.

solved as functions of the density using the cold-plasma dispersion relation (Eq. (2.26)) for $N_{\|} = -2, \ -5, \ -10$ with $B = 0.12$ T. The electrostatic condition, $|N_{\perp}| \gg |N_{\|}|$, is satisfied when the density is higher than 10^{16}–10^{17} m^{-3}. Therefore, we can expect that the launched LHW behaves as the electrostatic wave in the plasma core in TST-2.

In order to investigate the group velocity and the resonance cone for TST-2 parameters, $(-P/S)^{1/2}$ is calculated and plotted in Fig. 3.7. The result indicates the direction of the group velocity and the wave vector, $v_{g,\|}/v_{g,\perp}$, when the electrostatic assumption (Eq. (2.55)) is satisfied. According to this result, propagation is dominantly in the parallel direction when the density is higher than approximately 10^{17} m^{-3}.

3.4 Early non-inductive ramp-up experiments using the grill and ICC antennas

In earlier studies using the grill antenna on TST-2 in 2012–2014, the optimum current drive efficiency was obtained around $-6 \leq N_{\|,0} \leq -2$ for 10 kA [59]. The grill antenna can excite the wave with $N_{\|,0}$ from -18 to 18 (Fig. 3.9). Since the waveguide size becomes large as the wave frequency is reduced, the waveguides

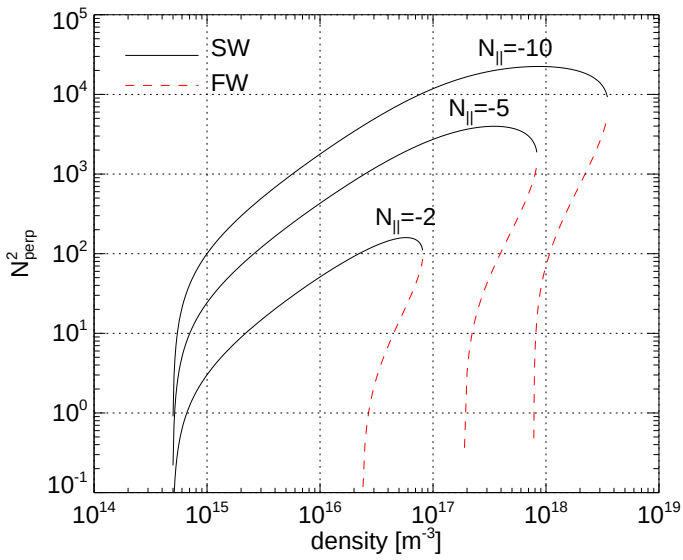

Fig. 3.6: $N_\perp^2$ of the SW (or the LHW, black solid line) and the FW (red dashed line) are plotted for $N_\parallel = -2,\ -5,\ -10$ with $B = 0.12$ T using the cold-plasma dispersion relation (Eq. (2.26)).

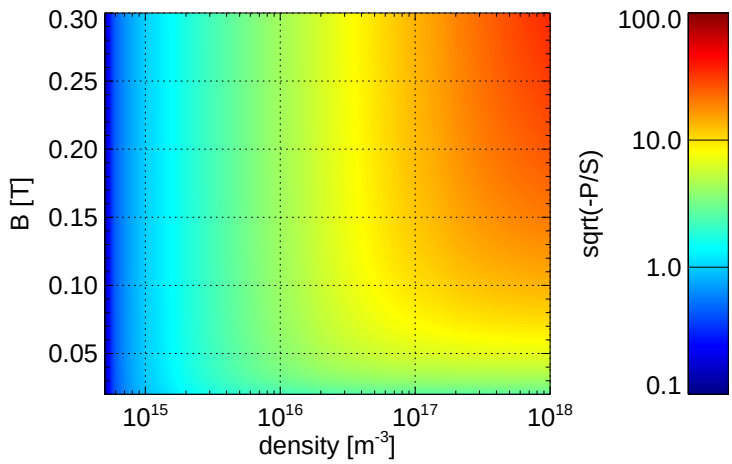

Fig. 3.7: Contour plot of $(-P/S)^{1/2}$ for TST-2 parameters. Under the electrostatic assumption, the contours indicate that the ratio of the parallel group velocity, $v_{g,\parallel}$, to the perpendicular group velocity, $v_{g,\perp}$, since $(-P/S)^{1/2} = |v_{g,\parallel}/v_{g,\perp}|$

.

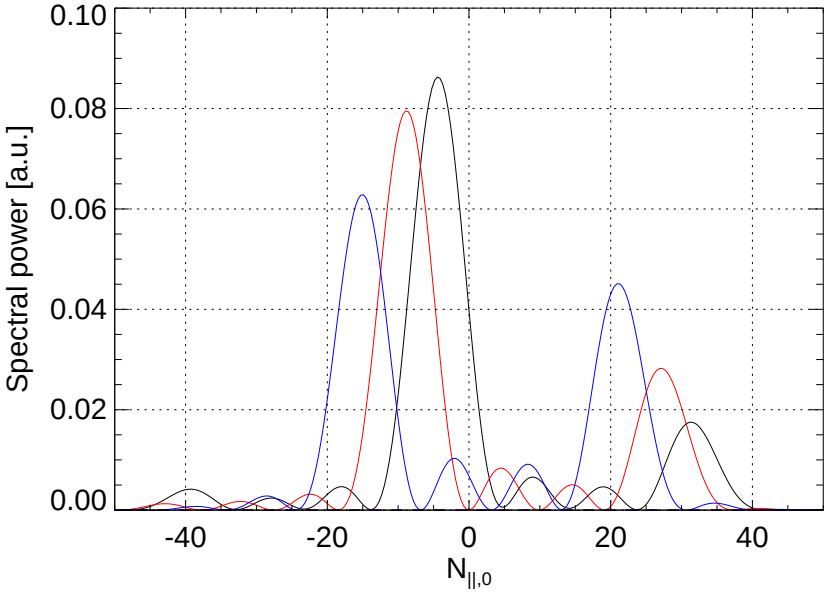

Fig. 3.8: $N_{||,0}$ spectrum of the grill antenna on TST-2 for three different phasings. The second peak becomes large by increasing the peak $|N_{||,0}|$ ($N_{||,0} = \pm 18$).

needed to be loaded with ceramic (Alumina with $\epsilon_r \approx 10$) in order to use the grill antenna in TST-2 at 200 MHz. However, the use of ceramic limited the input power to around 100 kW due to a large reflection coefficient and arcing along the ceramic at the antenna surface. The poderomotive force, enhanced by the ceramic, caused a vacuum gap between the antenna and the plasma, which lead to a low plasma-antenna coupling and large reflection.

In addition to the power limitation, the excited $N_{||,0}$ spectrum was broad and contained a second peak because there were only four waveguides (Fig. 3.8). The broad $N_{||,0}$ spectrum can cause extra ionization which prevents the LHW from penetrating into the plasma core due to mode conversion. The second peak can drive the plasma current in the opposite direction, and hence it would deteriorate the current drive efficiency. Thus, the requirement for the new LHW antenna is to launch the LHW with a sharp and single peaked $N_{||,0}$ spectrum with low reflectivity.

In order to achieve higher plasma currents on TST-2, it is necessary to develop a new type of LHW antenna which can handle higher power and launch the LHW with sharp and single peaked $N_{||,0}$ spectrum. The combline-type antenna is special. The antenna size is not limited by the port size and the input impedance is 50Ω, so it is possible to launch a sharp $N_{||}$ spectrum with low reflectivity. We also

performed experiments using the inductively-coupled combline (ICC) antenna on TST-2 in 2010–2012 (Fig. 3.10) [60]. The ICC antenna was used on JFT-2M at JAEA [61] [62] previously to investigate the FW current drive physics. After the shutdown of the JFT-2M project, the ICC antenna was disassembled, modified for use on TST-2, and was installed in 2010. The ICC antenna consists of eleven-element quarter-wave resonant straps, which are coupled by the mutual inductance. Hence, it is possible to launch a sharp $N_{\|}$ spectrum with the ICC antenna. The front surface of the antenna was designed to fit to a spherical surface, in order to keep a constant distance between the antenna surface and the plasma. The antenna was installed on the outboard midplane of TST-2, and the front surface of the antenna was located at $R = 0.59$ m. The launched parallel refractive index is fixed by the antenna geometry to be $N_{\|,0} = -7.2$. In TST-2, the density in front of the antenna is lower than the cutoff density for the FW, and hence the current drive efficiency was not good. However, up to 15 kA of plasma current was driven non-inductively using the ICC antenna . Therefore, it is believed that the FW tunnelled through the evanescent layer and was converted to the LHW at the mode conversion density [63]. Hence, we can expect a more efficient current drive and high plasma current by using an optimized combline-type LHW antenna.

Therefore, we developed a combline-type LHW antenna to launch the LHW directly with a sharp and single-peaked $N_{\|}$ spectrum with low reflectivity.

Fig. 3.9: Photograph of the grill antenna (ceramic-loaded waveguide array).

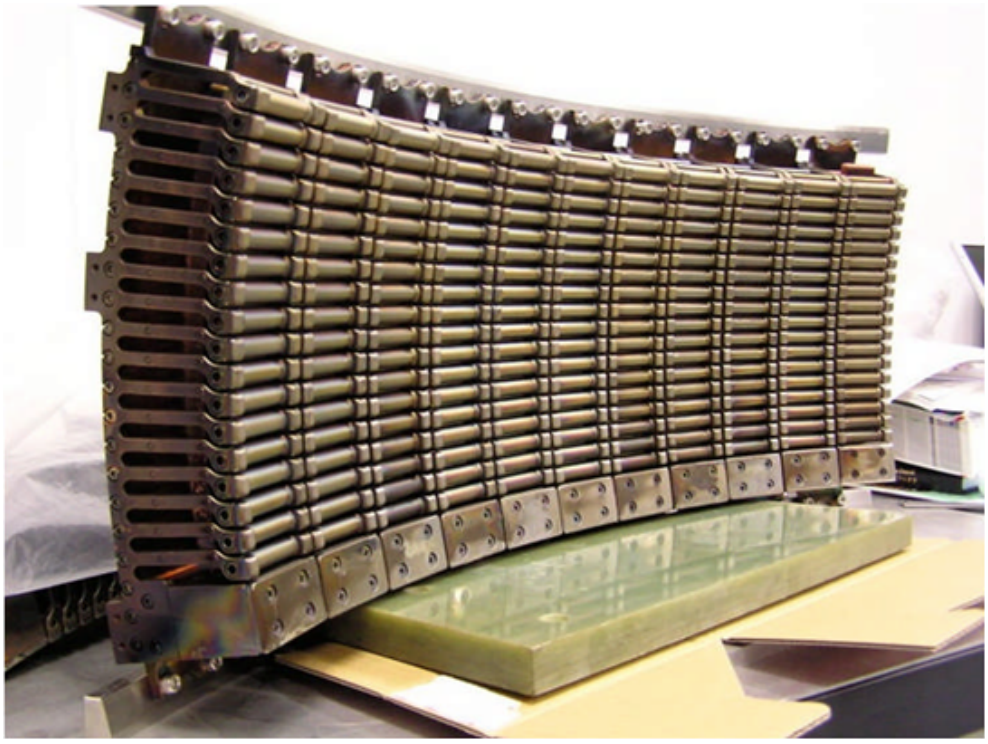

Fig. 3.10: Photograph of the ICC antenna.

Chapter 4

Development of the CCC Antenna

4.1 Concept and design

In order to launch the LHW directly with low reflectivity and a sharp, single peaked $N_{\|,0}$ spectrum, the Capacitively-Coupled Combline (CCC) antenna was developed in collaboration with General Atomics (GA) (Fig. 4.1). The CCC antenna consists of thirteen half-wave resonant straps, which couple capacitively with adjacent elements. The input and output ports are located behind both end elements. The characteristics of the CCC antenna is basically the same as the combline band-pass filter. Hence, the input impedance can be adjusted to be 50Ω at 200 MHz by selecting suitable inductance (L) and capacitance (C) (Fig. 4.2, 4.3).

The CCC antenna was designed to launch a sharp and single peaked $N_{\|,0}$ spectrum around -5.5, which is within the range of preferable $N_{\|,0}$ as described in Chapter 3. The CCC antenna is also installed on the outboard midplane of the vessel at $(R,\ z)$ = (0.621 m, 0 m). Considering the polarization of the electric field of the LHW, the antenna must excite the RF electric field along the confining magnetic field. In TST-2 start-up experiment, the magnetic field pitch angle in front of the antenna is negligible, and hence the CCC antenna excites the RF electric field along the toroidal direction by capacitive coupling with adjacent elements. The elements are electrically half-wavelength at 200 MHz, and hence the electric field is maximum at the midplane. Naturally, the dominant component of mutual coupling coefficient (M) is capacitive. The phase shift from element to element is approximately -60 degrees ($N_{\|,0} = -5.5$), and hence a backward wave is launched from the CCC antenna: the direction of energy flow in the CCC antenna is opposite to the parallel phase velocity and the parallel group velocity of the LHW.

For minor adjustments of the impedance of each element, the inductance of

Fig. 4.1: Front view of the CCC antenna.

the rods are adjusted by changing the positions of short to the baseplate (Fig. 4.2, 4.3), and the input impedance of the whole antenna was adjusted by changing the position of the feeder connection. Assembly, minor adjustments, and calibration were performed at our laboratory.

4.2 Impedance matching and $N_{||,0}$ adjustment

Calibration was performed using a network analyzer (NWA, Hewlett Packard 8712C), which can sweep the RF frequency from 0.3 MHz to 1300 MHz and measure the complex S-parameters (amplitude and phase). The main aim of calibration is to adjust the input impedance to 50Ω around 200 MHz and the phase shift between elements to -60 degrees (which corresponds to $N_{||,0} = -5.5$). Note that the wide bandwidth ensures a stable 50Ω impedance for 200 MHz even if the antenna impedance is slightly affected by the plasma. The RF signal from the NWA was fed to the input port of the antenna, and the wave transmitted to the output port and the wave reflected from the input port were measured by the NWA (Fig. 4.4). After calibration, the input impedance was successfully adjusted to 50Ω in the range 197–203 MHz. The reflected power is less than 0.1 % of the incident power (Fig. 4.5). The transmitted power is approximately 82 %, and the 18 % loss is caused by electromagnetic wave radiation and dissipation by antenna resistance. The phase shift was also successfully adjusted to -58.9 ± 6.1 degrees

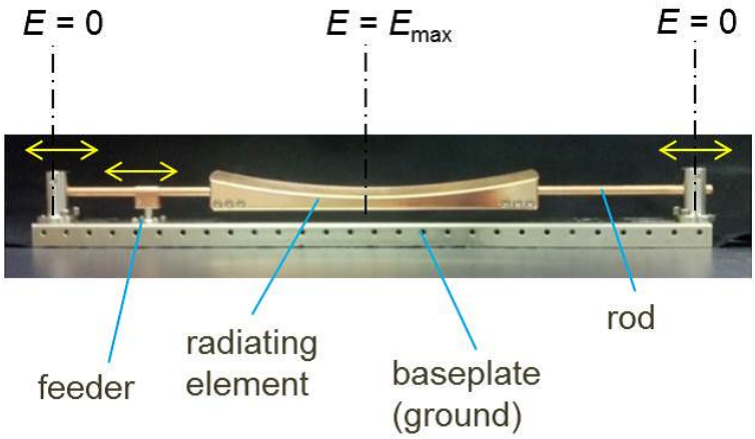

Fig. 4.2: Side view of the input/output element with covers surrounding the rods removed.

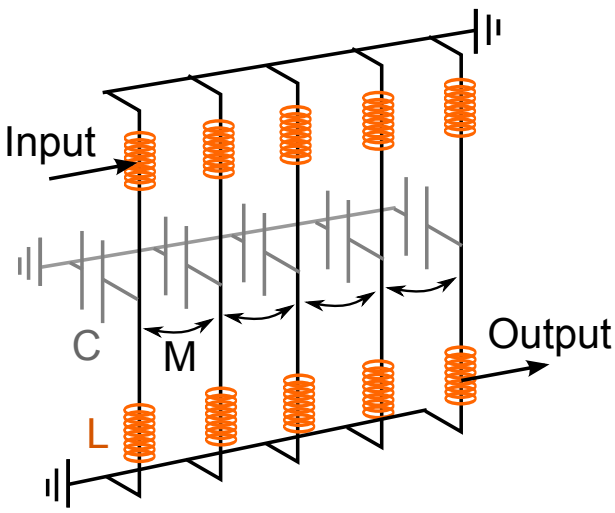

Fig. 4.3: Schematic circuit of the CCC antenna (five elements are shown). L, C, and M represent the capacitance, inductance, and mutual coupling coefficient (mostly capacitive), respectively. The LHW propagates from right to left, opposite to the power flow in the CCC antenna (backward wave).

at the same time (Fig. 4.6(a)). The phase at each element was measured using a small loop coil which detects the RF magnetic field induced by the RF current near the short point. The RF signal from the NWA was fed to the input port of the antenna, and the RF magnetic field (amplitude and phase) detected by the loop coil was measured with the NWA. The output port of the antenna was connected to a 50Ω termination to absorb the transmitted power. Assuming a constant amplitude of the RF electric field between elements (neglecting the weak antenna losses), we can calculate the $N_{||,0}$ spectrum from the measured phases (Fig. 4.6(b)). The peak of the $N_{||,0}$ spectrum is approximately at -5.5, which is what we aimed for. Note that the calculated $N_{||,0}$ spectrum is the spectrum of the RF electric field in front of the antenna, not the traveling wave in air or vacuum. In Fig. 4.7, we can see how the CCC antenna $N_{||,0}$ spectrum is improved over the grill antenna. A desired $N_{||,0}$ spectrum (sharp and single-peaked) is realized by the CCC antenna. Thus, we have succeeded in developing a new LHW antenna for 200 MHz which excites a sharp and single-peaked $N_{||,0}$ spectrum.

We also checked the input impedance of the vacuum feedthrough used in the experiment. The feedthrough was not designed for 200 MHz, and hence 10% of the reflected power was induced at the feedthrough. However, the reflected power is low enough for safe operation, and hence we decided to use the feedthough without modification for the CCC antenna.

4.3 $N_{||,0}$ spectrum in the plasma

The input RF power undergoes an exponential decay from element to element due to radiation of RF wave (≈ LHW) into the plasma, and hence it is necessary to adjust the antenna-plasma coupling, for example by changing the limiter position to control the density in front of the antenna. In the case of a strong decay of input power (strong antenna-plasma coupling), the $N_{||,0}$ spectrum deteriorates. When the power decay is weak (weak antenna-plasma coupling), the $N_{||,0}$ spectrum remains sharp, but the efficiency of RF wave radiation into the plasma is low. For convenience, the number of effective elements (n_{eff}) is defined as

$$P_{n_{eff}}/P_{input} \approx 0.1, \tag{4.1}$$

where P_n is the RF power at the nth element, and P_{input} is the RF input power. As shown in Fig. 4.8, an optimum case is obtained with n_{eff} = 13 (10 % of input power remained at the 13th element). In this case, the $N_{||,0}$ spectrum is approximately the same as that for the vacuum (or air) case, and the efficiency of RF power radiation into the plasma is 90 % (blue dashed line). In this calculation, the measured phases described in the previous section were used. For the case of n_{eff} = 2 (black long dashed line), the peakepower of the spectrum is only 20%

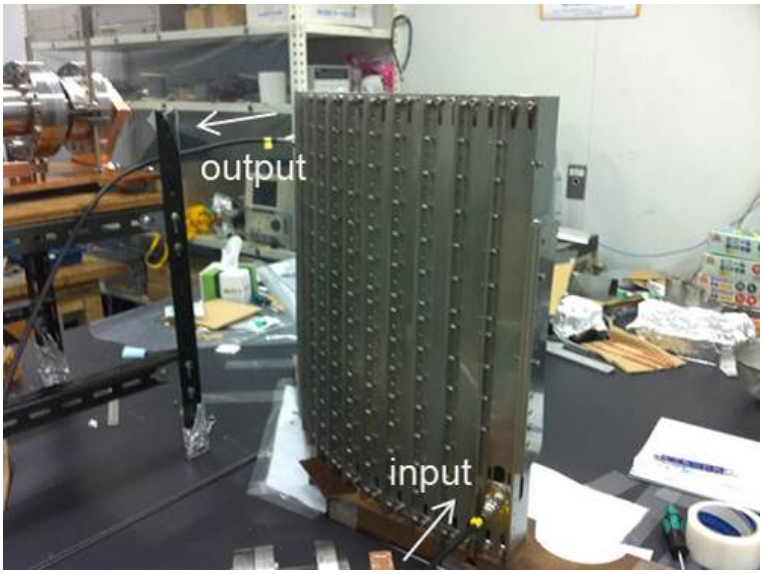

Fig. 4.4: Calibration setup.

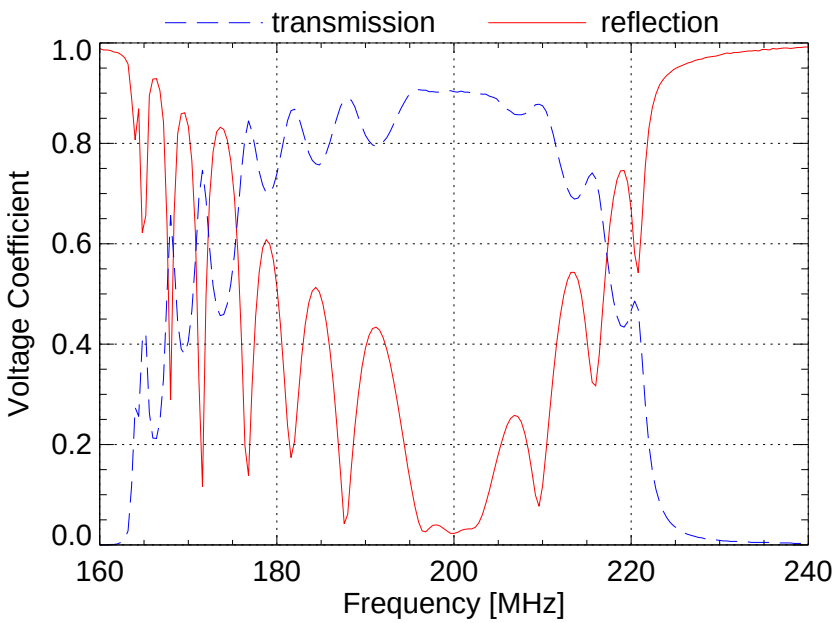

Fig. 4.5: Frequency dependences of transmission and reflection coefficients of the CCC antenna, measured in air.

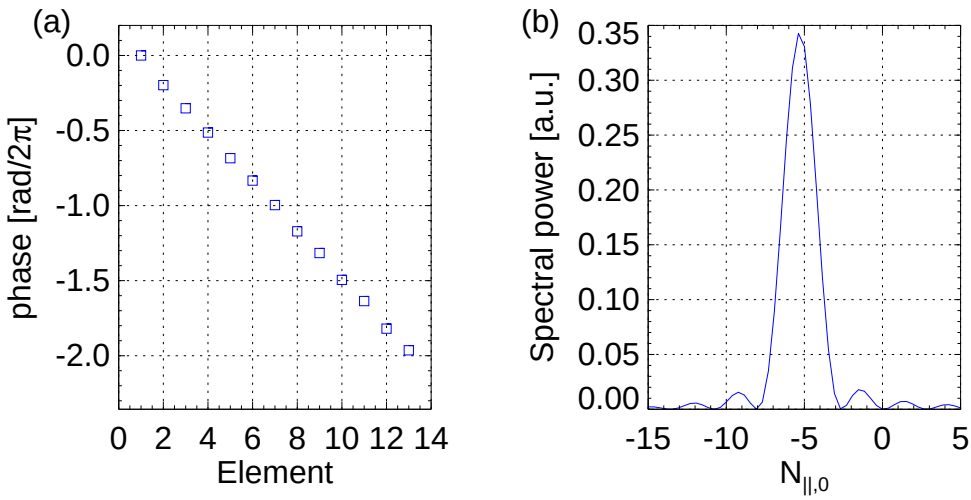

Fig. 4.6: Phase (a) and $N_{||,0}$ spectrum (b) of the CCC antenna, measured in air. The spectrum is peaked at $N_{||,0} = -5.5$.

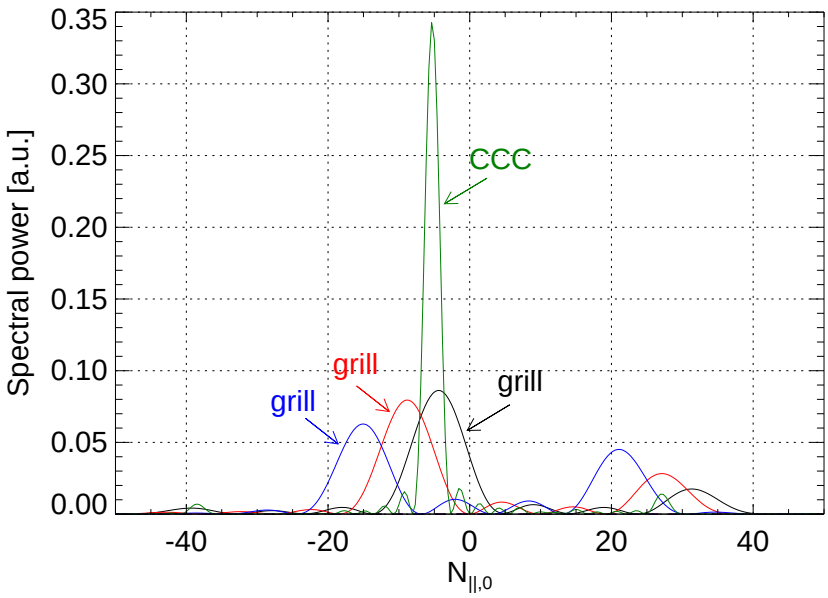

Fig. 4.7: Comparison of $N_{||,0}$ spectra between the CCC antenna and the grill antenna (at three phasings).

of the vacuum case, and the spectrum contains non-negligible positive $N_{\|}$ components. For the case of $n_{eff} = 6$ (red solid line), the $N_{\|,0}$ spectrum is broader than the optimum case ($n_{eff} = 13$), but the positive $N_{\|}$ components are substantially low, i.e. this $N_{\|,0}$ spectrum should be effective for current ramp-up.

4.4 Installation on TST-2

The CCC antenna was installed on TST-2 in 2013 (Fig. 4.9, 4.10). The front surface of the antenna is located at $R = 0.621$ m, and the center of the antenna in the vertical direction (where $E = E_{max}$) is located at the midplane ($z = 0$ m). In order to protect the CCC antenna from the plasma and to adjust the antenna-plasma coupling, the antenna limiters are located on both sides of the antenna (Fig. 4.12). The antenna limiter consists of molybdenum (Mo) tiles mounted on a stainless steel (SUS304) plate. The antenna limiters are attached to the ribs on the outboard vacuum vessel wall, and hence vacuum opening is necessary to adjust the position of the antenna limiter. In this experiment, antenna-plasma coupling was investigated with two different antenna limiters. The first limiter was located at $R = 0.585$ m and had a radius of curvature of 0.585 m. The second limiter is located at $R = 0.607$ m. In addition to the antenna limiter, there is a main limiter at $R = 0.585$ m. The toroidal location of the main limiter is 60° counterclockwise (viewed from the top) from the antenna limiter on the input side. The main limiter is also mounted on an outboard rib. The upper and lower limiters (z450 limiter) are installed at $z = \pm 0.45$ m (Fig. 4.11). Two Langmuir probes (U1 probe and U2 probe) are mounted at $(R, z) = (0.275$ m, 0.45 m) and $(0.475$ m, 0.45 m) on the upper z450 limiter. The probe tip length is approximately 3 mm, and the diameter is 0.51 mm.

In order to measure the density profile in front of the antenna (the region between the two antenna limiters), 3-element Langmuir probe arrays are mounted on the inside surfaces of both input side and output side antenna limiters (Fig. 4.13(b), Fig. 4.10). The three Langmuir probes are made of three thin rectangular copper electrodes plated on a ceramic substrate. The width of the Langmuir probe is 2 mm and the height is 18 mm. The three Langmuir probes are located at $R = 0.594$ m, 0.598 m, 0.602 m, and are named IP1 ($R = 0.594$ m on the input side), IP2 ($R = 0.598$ m on the input side), IP3 ($R = 0.602$ m on the input side), OP1 ($R = 0.594$ m on the output side), OP2 ($R = 0.598$ m on the output side), and OP3 ($R = 0.602$ m on the output side).

In order to monitor the $N_{\|,0}$ spectrum, 1-turn loop RF magnetic probes are installed at the bottom end of the 1st, 2nd, 4th, 6th, 9th, 11th, and 13th elements (Fig. 4.13(a)). The RF magnetic probes measure RF magnetic fields induced by RF current in each element. The measured RF current is proportional to the RF

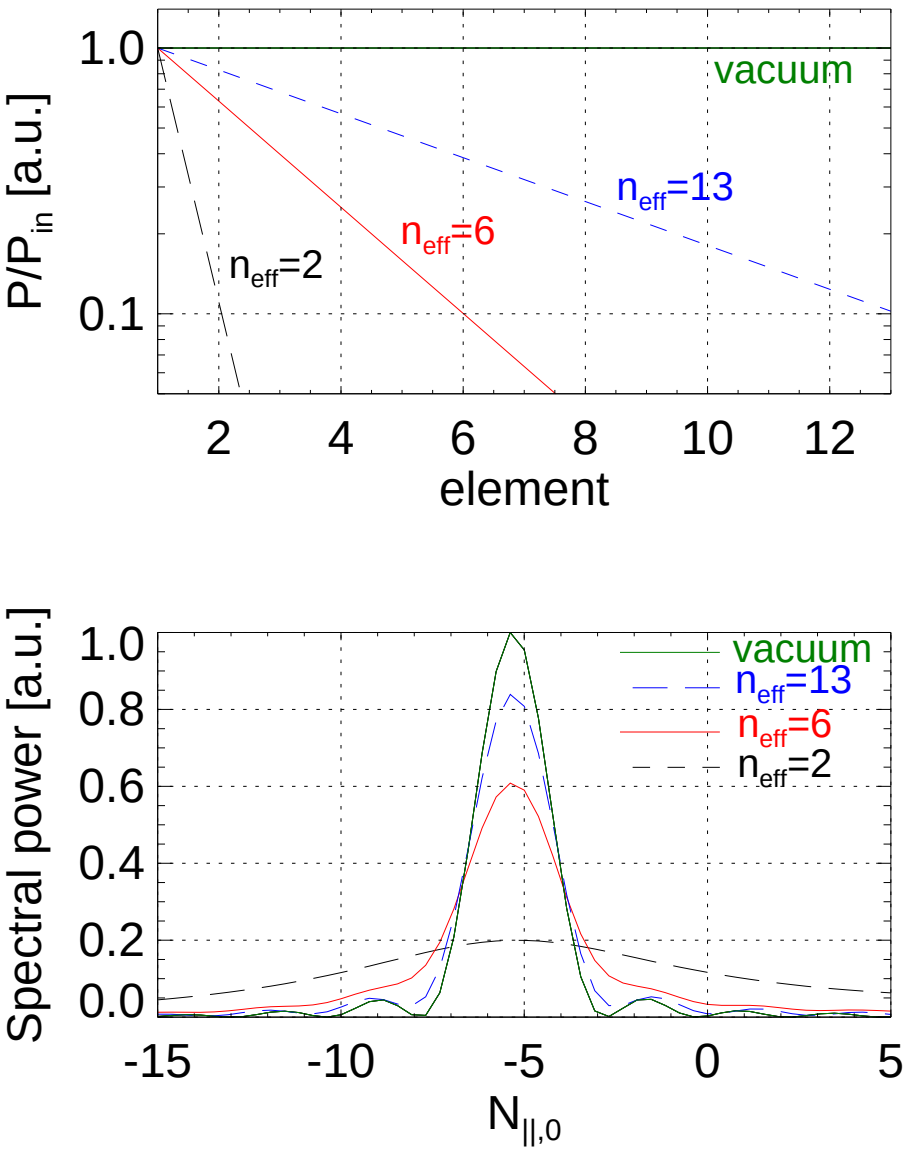

Fig. 4.8: Calculation of the $N_{||,0}$ spectrum for four cases of antenna-plasma coupling, $n_{eff} = 13$ (blue dashed line), $n_{eff} = 6$ (red solid line), $n_{eff} = 2$ (black long dashed line), and vacuum ($n_{eff} = \infty$, green solid line).

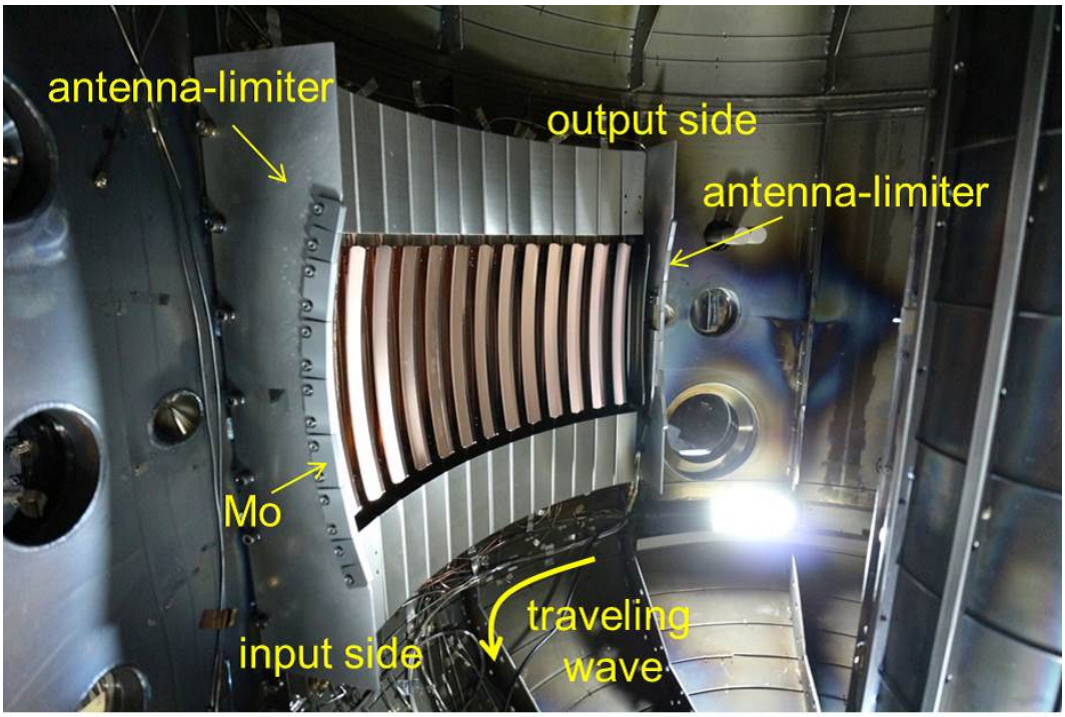

Fig. 4.9: CCC antenna installed inside TST-2. The antenna is protected by antenna limiters on both input side and output side.

potential at the midplane of each element, and hence it is possible to estimate the RF electric field between neighboring elements from the measured signals. The method will be described in the Chapter 5.

Five RF magnetic probes (RFMPs) were installed at $(R, z) = (0.223, 0.45)$, (0.295,0.45), (0.367,0.45), (0.439,0.45), and (0.510,0.45) m on the upper z450 limiter to measure the LHW. According to ray-tracing calculations, it is expected that RFMPs can be used to study LHW propagation in the SOL.

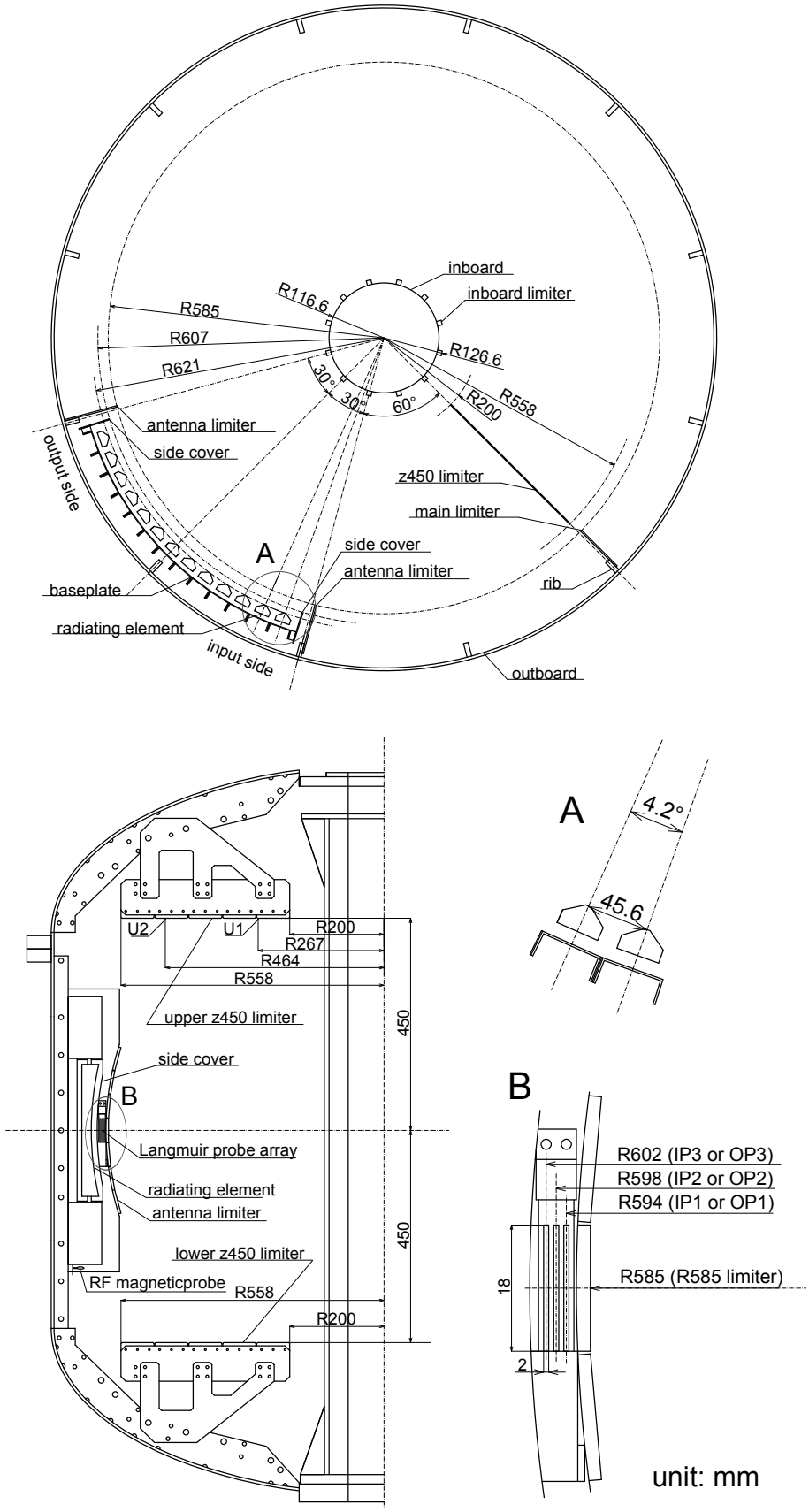

Fig. 4.10: Top view and side view of the CCC antenna, limiters, and diagnostics installed in TST-2.

Fig. 4.11: Upper and lower z450 limiters installed at $z = \pm 0.45$ m. Two Langmuir probes are mounted on the upper z450 limiter. U1 probe at (R, z) = (267mm, 450 mm) and U2 probe-: at (R, z) = (464mm, 450 mm).

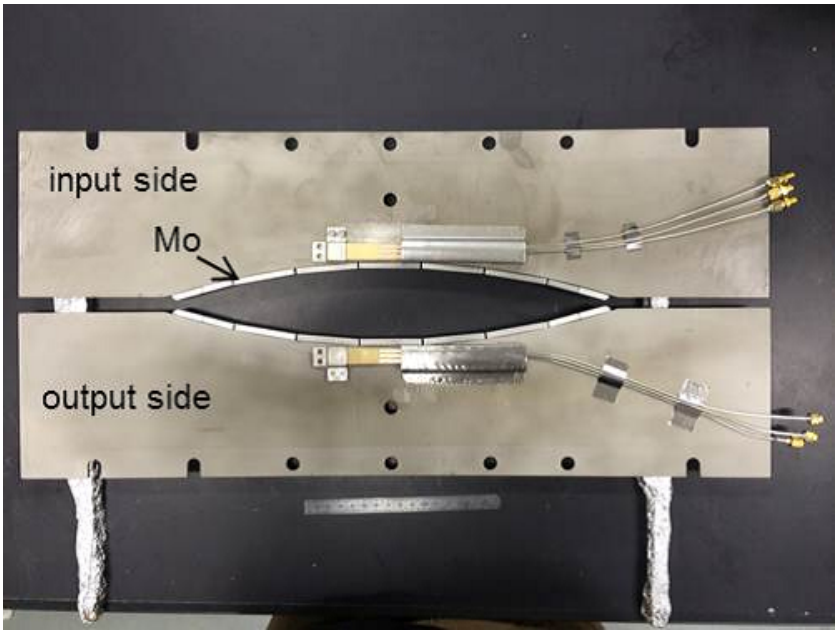

Fig. 4.12: Antenna limiters to protect the CCC antenna from the plasma and to adjust antenna-plasma coupling. Antenna limiters are installed on the outside both ends (input element and output element) of the antenna. The curved region facing the plasma is covered with Mo tiles to prevent melting. Inside the antenna limiters (the sides facing the antenna), Langmuir probe arrays are mounted to measure the density profile in front of the antenna.

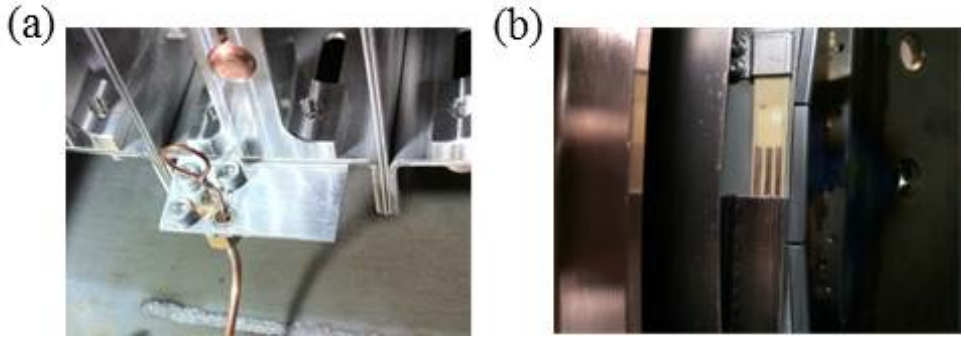

Fig. 4.13: Diagnostics on the CCC antenna. (a) RF magnetic probe to monitor the $N_{||,0}$ spectrum by measuring the RF magnetic field induced by the RF current at bottom short point of each element. RF magnetic probes are installed at the 1st, 2nd, 4th, 6th, 9th, 11th, and 13th elements. (b) Langmuir probe array to measure the density and temperature profiles in front of the antenna. The arrays are installed on the inside (antenna side) of the antenna limiter on both the input side and the output side.

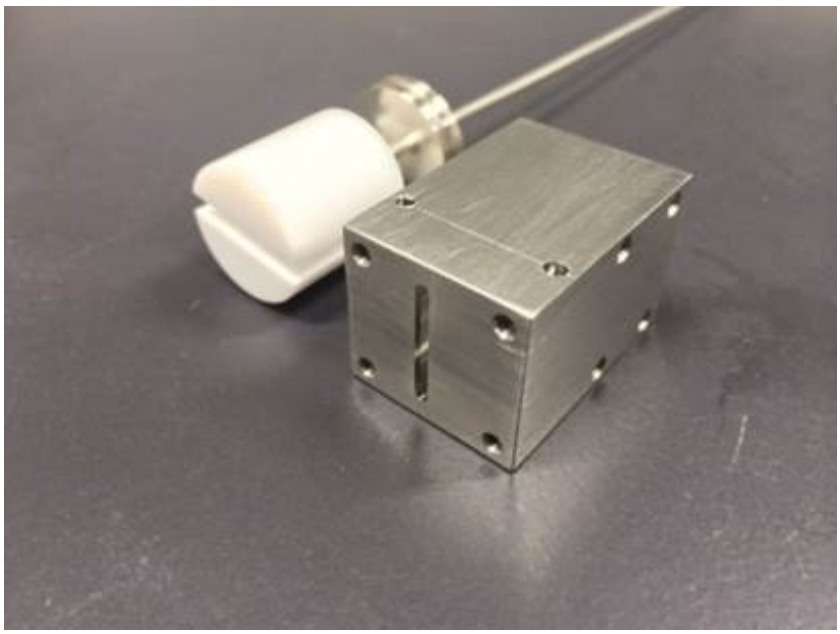

Fig. 4.14: RFMP (one-turn coil wound in the slot machined in the Teflon holder) and stainless steel shield case. Five RFMPs were installed at $(R, z) = (0.223, 0.45)$, (0.295,0.45), (0.367,0.45), (0.439,0.45), and (0.510,0.45) m.

4.5 Langmuir probe theory

The Langmuir probe characteristic is approximately described by

$$I_{\mathrm{pr}}(V) \;=\; I_{\mathrm{sat}}\left[1 \;+\; \exp\left(\frac{V - V_{\mathrm{fl}}}{T_{\mathrm{e}}}\right)\right]. \tag{4.2}$$

I_{pr} is the current flowing through the Langmuir probe, V is the bias voltage on the probe, I_{sat} is the ion saturation current, and V_{fl} is the floating potential where $I_{\mathrm{pr}} = 0$. The electron temperature T_{e} can be derived from this equation. Using the measured T_{e}, the ion density can be derived as

$$n_i \;=\; \frac{-I_{\mathrm{sat}}}{eZS_{\mathrm{p}}\exp(-1/2)(\kappa T_{\mathrm{e}}/m_i)^{1/2}}, \tag{4.3}$$

where S_{p} is the probe area.

In the presence of the RF potential, $V_{\mathrm{RF}}\sin(\omega t)$, the potential will vary as [58]

$$V \;\rightarrow V \;+\; V_{\mathrm{RF}}\sin(\omega t). \tag{4.4}$$

When we substitute the potential to Eq. (4.2), and average over $-T/2 \leq t \leq T/2$ where T is the RF oscillation period, we obtain the time-averaged probe current in the presence of the RF potential as [58]

$$I_{\mathrm{pr}}^{\mathrm{ave}}(V) \;=\; I_{\mathrm{sat}}\left[1 \;+\; I_0(\alpha)\exp\left(\frac{V - V_{\mathrm{RFfl}}}{T_{\mathrm{e}}}\right)\right], \tag{4.5}$$

$$I_0(\alpha) = \frac{1}{\pi}\int_{-T/2}^{T/2}\exp(\alpha\sin\omega t)dt \tag{4.6}$$

where $\alpha = V_{\mathrm{RF}}/T_{\mathrm{e}}$. Hence, the floating potential in the presence of the RF potential, V_{RFfl}, is lower than V_{fl} [58]. Note that the density and temperature measured by the probe are not affected by the presence of the RF potential.

Chapter 5

Current Ramp-up Experiment using the CCC Antenna

5.1 Current ramp-up experiment

The plasma current was ramped up successfully to approximately 20 kA using the CCC antenna. A typical I_p ramp-up discharge with the R585 antenna limiter and the z450 limiter (without the main limiter) is shown in Fig. 5.1. As shown in Fig. 5.1(e), the RF power reflectivity is less than 10 %. If we could design the vacuum feedthrough optimized for 200 MHz, the reflectivity would be reduced to few %. The reflected RF power was diverted to the dummy load and absorbed to prevent damage to the FPA. Note that no transmitted RF power was observed at the output port of the antenna (Fig. 5.1(e)). This result indicates that the antenna-plasma coupling was stronger than the optimum case (10 % transmitted power), so that the $N_{\|,0}$ spectrum of the excited LHW was broader than the optimum case, but still substantially sharper than the spectra with the grill antenna (Sec. 5.2). Even in such a case with no output, we can estimate the $N_{\|,0}$ spectrum using the data obtained by RF magnetic coils equipped under several elements of the CCC antenna. The RF power $P_{\mathrm{coil,\ n}}$ and phase $\phi_{\mathrm{coil,\ n}}$ were measured at the nth element with sufficient signal to noise level (Fig. 5.1(g), (h)). The subscript 'n' refers to the element number counted from the input side (n = 1, 2, 4, 6, 9, 11, or 13). Using the RF powers measured at these elements, we define the number of effective elements (n_{eff}) as $P_{\mathrm{coil,\ n_{eff}}}/P_{\mathrm{coil,\ 1}} \approx 0.1$. In the R585 antenna limiter case, the n_{eff} was around 6–8 (Fig. 5.1(j)). The results of antenna-plasma coupling and the $N_{\|,0}$ spectrum will be described in Sec. 5.2.

The plasma current is mainly determined by the vertical field strength because the force balance must be satisfied (Fig. 5.1(c)). The current ramp-up rate was approximately 400 kA/sec (20 kA over 50 ms). This may lead to the expecta-

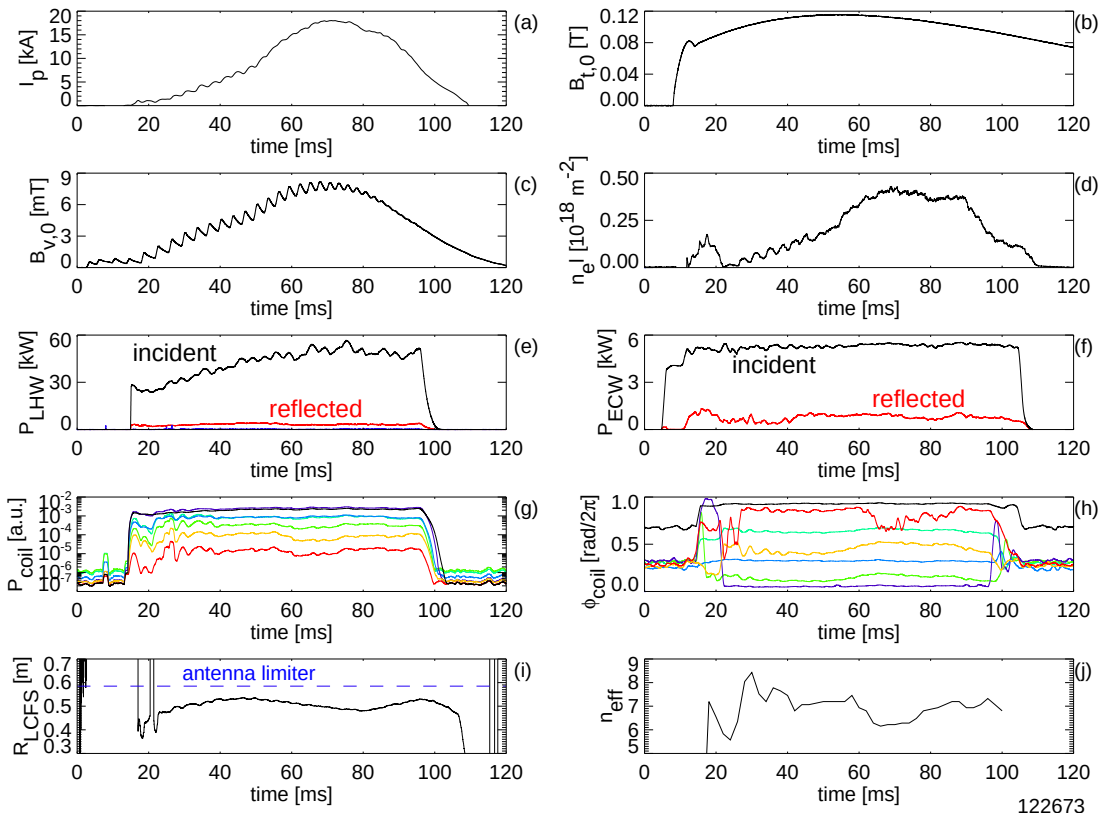

Fig. 5.1: Typical non-inductive I_p ramp-up discharge with the CCC antenna. (a) Plasma current, (b) toroidal magnetic field at the plasma center, (c) vertical field at the plasma center, (d) line-integrated density along a vertical chord at $R = 0.39$ m, (e) LH power: incident RF power (black), reflected RF power (red), transmitted RF power (blue), (f) ECW power: incident power (black), reflected power (red), (g) RF power in arbitrary unit measured by RF magnetic probes at 1st (black), 2nd (blue), 4th (sky blue), 6th (light green), 9th (green), 11th (orange), 13th (red) elements, (h) RF phase measured by RF magnetic coils, (i) major radius of the outboard LCFS on the midplane, (j) number of effective elements, n_{eff} ($P_{coil,\ n_{eff}}/P_{coil,\ 1} \approx 0.1$).

tion of achieving 400 kA over 1 sec by increasing the pulse length, but it is also necessary to solve other limitations associated with current ramp-up. The maximum plasma current is also limited by the toroidal magnetic field strength and the plasma density (and naturally the RF power). The details will be described in Sec. 5.3.

In order to use the toroidal magnetic field effectively, the maximum plasma current should be reached around 60 ms (Fig. 5.1(b)). However, the antenna and the vacuum vessel must be conditioned sufficiently for the current to reach the peak around 60 ms, because such a rapid ramp-up increases the plasma density, and the plasma will disrupt by approaching the density limit (Sec. 5.3). The density limit will be discussed using the line-integrated density, $n_e l$, at $R = 0.39$ m (Fig. 5.1(d)). The plasma height within the LCFS is approximately 0.5 m along this chord, and hence the line- averaged density is given as $\overline{n}_e = n_e l/0.5$.

The LHW was launched by the CCC antenna after preionization by ECW. It was discovered that the ECW is also effective for suppressing the plasma density during the current ramp-up phase, and hence ECW was injected throughout the discharge (Fig. 5.1(f)). The density suppression experiment using the ECW will be described in Sec. 5.5.

Typical electron density, temperature, and pressure profiles are presented in Fig. 5.2. Measurements using the Thomson scattering system on TST-2 were first performed in this CCC antenna campaign. The line-integrated density through the vertical chord at $R = 0.39$ m was 0.4–$0.5 \times 10^{18}\mathrm{m}^{-2}$. The measured profiles on the midplane indicate that the sustained plasma has a parabolic electron density profile and a hollow electron temperature profile with the temperature at the inboard side higher than that at the outboard side. The most important information from this measurement is that the electron temperature is too low to expect strong absorption of the LHW in the plasma core since $|N_{\|}|T_e^{1/2} = 5.5 \cdot 0.02^{1/2} \approx 0.8 < 5$–$7$. In addition to the weak absorption condition in the plasma core, the higher edge temperature could induce edge LHW power deposition. It is believed that the power deposited at the edge is mostly lost quickly because the electron orbits in the vicinity of the LCFS could intersect the inboard wall or limiters, or because of conduction and radiation losses. An up-shift of $N_{\|}$ occurs on the inboard side due to the toroidal upshift (the toroidal component of the wavenumber is given by n/R where the toroidal mode number n is conserved), and the up-shifted LHW could provide a temperature increase on the inboard side rather than the plasma center during the first pass through the plasma. The edge density and temperature will be compared with Langmuir probe results in Sec. 5.2.

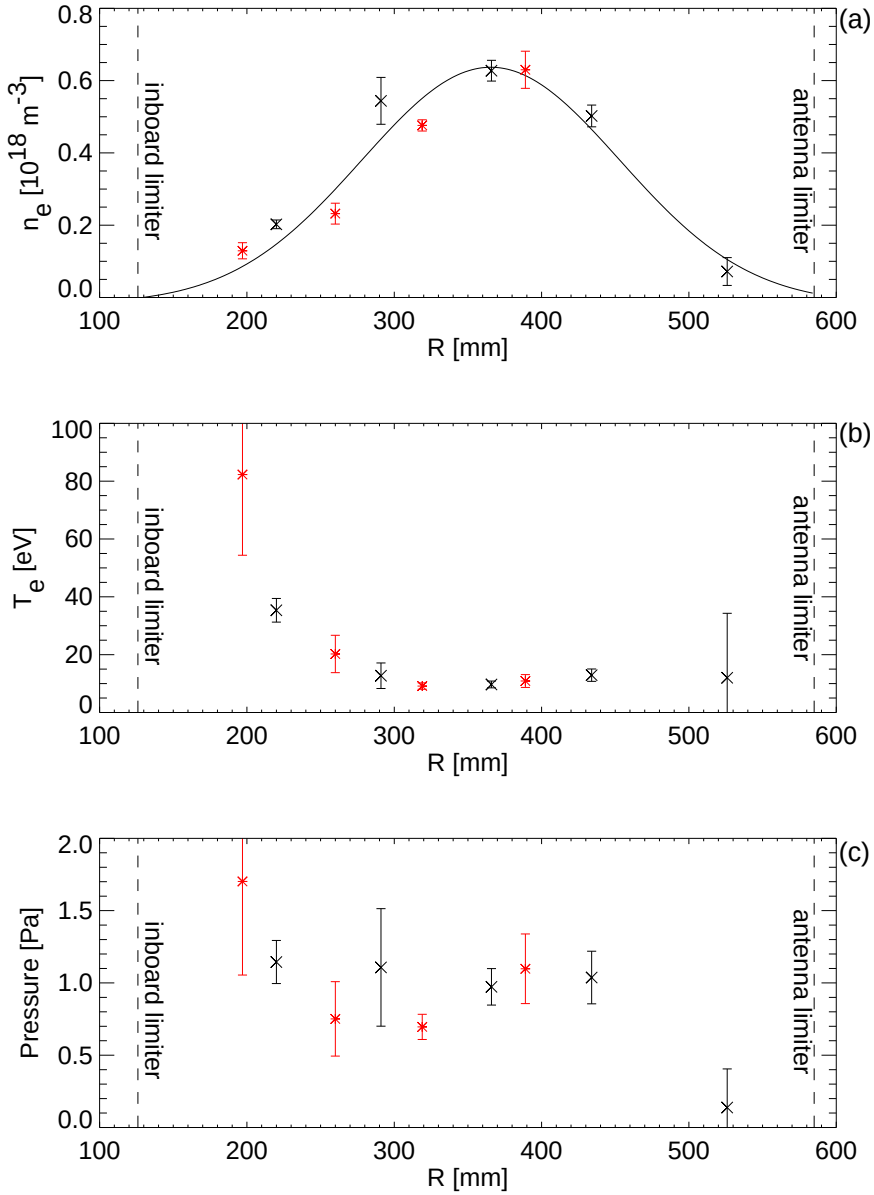

Fig. 5.2: Electron density profile (a), temperature profile (b), and pressure profile (c) measured by Thomson scattering. The profiles were obtained by accumulating six shots (black × symbols) or four shots (red ∗ symbols).

5.2 Antenna-plasma coupling

Optimization of the $N_{\|,0}$ spectrum

The antenna-plasma coupling of the CCC antenna was studied experimentally by changing the radial positions of the antenna limiter and the main limiter. Three cases were investigated. In the first case, (antenna limiter, main limiter) = (R607, R585). At the beginning of the CCC antenna campaign, RF magnetic coils were installed at 2nd, 4th, 6th, and 9th elements, but the Langmuir probe array was not installed. The measured P_{coil} was fitted with an exponential function and ϕ_{coil} was fitted with a straight line as functions of element number (Fig. 5.3(a), (b)). According to the fit, n_{eff} is estimated to be 4–5. After the campaign, we removed the main limiter, so (antenna limiter, main limiter) = (R607, -). In this case, antenna-plasma couping was too strong to determine n_{eff} from the four RF magnetic coils, but it is clear that n_{eff} is less than 4. It was found that we need to place the antenna limiter beyond $R = 0.607$ m to weaken antenna-plasma coupling. After these experiments, we installed the antenna limiter at $R = 0.585$ m to reduce antenna-plasma coupling. For the case of (antenna limiter, main limiter) = (R585, -), n_{eff} is estimated to be 6–8 (Fig. 5.4(a), (b)).

The $N_{\|,0}$ spectrum is calculated using the fits to P_{coil} and ϕ_{coil}. The electric field in front of the antenna can be written as

$$E(\varphi) \cong \begin{cases} \frac{\Phi_{\mathrm{j+1}} - \Phi_{\mathrm{j}}}{\Delta L} & \text{for} \quad \mathrm{j}\frac{\Delta L}{R_{\mathrm{a}}} \leq \varphi < (\mathrm{j}+1)\frac{\Delta L}{R_{\mathrm{a}}} \\ 0 & \text{for} \quad 12\frac{\Delta L}{R_{\mathrm{a}}} \leq \varphi < 2\pi \end{cases} \tag{5.1}$$

$$\Phi_{\mathrm{n}} = P_{\mathrm{coil,\ n}}^{1/2} \exp(i\phi_{\mathrm{coil,\ n}}) \tag{5.2}$$

where $0 \leq j \leq 11$, $\Delta L \approx 0.0456$ m, and $R_{\mathrm{a}} = 0.621$ m. The subscript "j " refers to the element number counted from the input side. ΔL is the distance between adjacent elements, where the arc length and the distance are taken to be the same because of the large curvature. R_{a} is the major radius at the antenna surface. We can derive the toroidal mode number spectrum, N_{tor}, of the electric field by Fourier transformation. Finally, we obtain the $N_{\|,0}$ spectrum as $N_{\|,0} \cong cN_{\mathrm{tor}}/\omega R_{\mathrm{a}}$.

The $N_{\|,0}$ spectrum for (antenna limiter, main limiter) = (R607, R585) is shown in Fig. 5.3(d). $N_{\|,0}$ at the peak of the spectrum is nearly the same as the vacuum spectrum, and hence the phase shift due to the plasma dielectric tensor is negligible. The peak of the power spectrum is reduced by 60 % due to the strong antenna-plasma coupling, and the spectrum contains high and low $N_{\|}$ components.

In order to reduce antenna-plasma coupling, the R585 antenna limiter was installed without the R585 main limiter, (R585, -). Throughout previous experiments with (antenna limiter, main limiter) = (R607, R585), we concluded that the

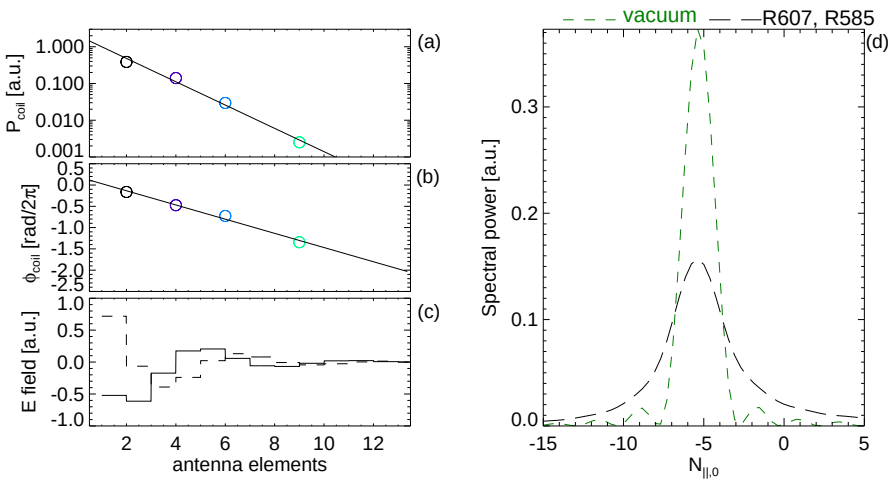

Fig. 5.3: RF magnetic probe data for the (R607, R585) case. (a) $P_{\text{coil, n}}$, (b) $\phi_{\text{coil, n}}$, (c) the real part (solid line) and the imaginary part (dashed line) of the electric field in front of the antenna calculated using Eq. 5.1, (d) $N_{||,0}$ spectra with plasma (black long-dashed line) and without plasma (green short-dashed line).

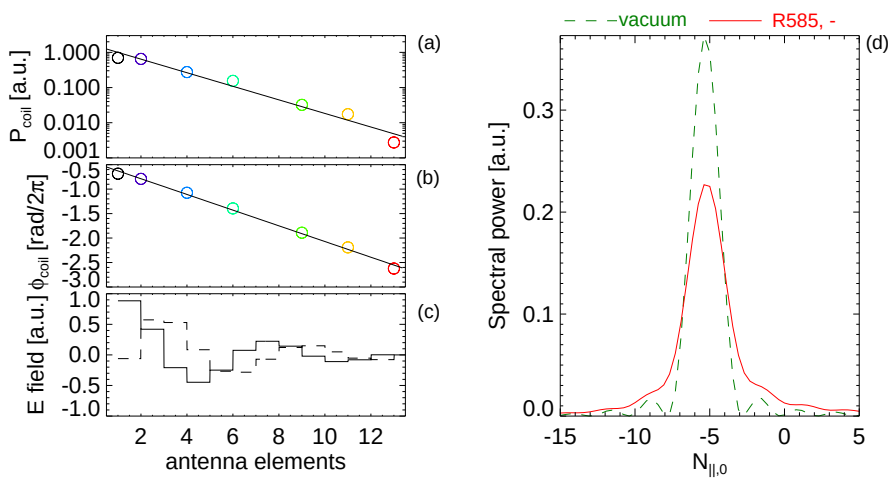

Fig. 5.4: RF magnetic probe data for the (R585, -) case. (a) $P_{\text{coil, n}}$, (b)$\phi_{\text{coil, n}}$, (c) the real part (solid line) and the imaginary part (dashed line) of the electric field in front of the antenna calculated using Eq. 5.1, (d) $N_{||,0}$ spectra with plasma (red solid line) and without plasma (green short-dashed line).

RF magnetic coils are effective for antenna-plasma coupling studies. The density profile in front of the antenna would also be useful. From this campaign, RF magnetic coils were added to the 1st, 11th, 13th elements, and a Langmuir probe array was also installed on the R585 antenna limiter. The measured P_{coil} and ϕ_{coil} can be fitted well by exponential and linear function of element number (Fig. 5.4(a), (b)). According to the fit, n_{eff} is approximately 6–8 elements. The $N_{\|,0}$ spectrum was improved thanks to the repositioning of the antenna limiter (Fig. 5.4(d)). The reduction of the peak of the spectrum is 40 % compared to the vacuum cas, and the positive components of $N_{\|}$ are negligible. Note that the first limiter for both (R585, -) and (R607, R585) cases are $R = 0.585$ m, but n_{eff} is different, 6–8 vs. 4–5. This result indicates that the antenna limiter is effective for reducing the antenna-plasma coupling. The density decay length probably increases as the distance from the main limiter to the antenna is increased. For the (R607, R585) case, the toroidal location of the main limiter was 60° counterclocwise from the antenna limiter on the input side, which was large enough to reduce n_{eff} to 1–4.

To obtain a sharper $N_{\|,0}$ spectrum than the (R585, -) case, it is necessary to move the antenna limiter further into the plasma. However, that would cause reflection of the LHW from the antenna limiter. The reflected LHW would drive the plasma current in the opposite direction. Considering the $N_{\|,0}$ spectrum for the (R585, -) case, the spectrum was sufficiently sharp to launch the LHW in only one direction, and hence the optimization of antenna-plasma coupling was discontinued.

One of our main objectives is to launch the LHW directly with a sharp and single-peaked $N_{\|,0}$ spectrum. A comparison of the $N_{\|,0}$ spectra for the CCC antenna and the grill antenna is shown in Fig. 5.5. It is clear that the $N_{\|,0}$ spectrum for the CCC antenna was improved dramatically. In the CCC antenna spectrum, the main peak contains only $-9 \leq N_{\|,0} \leq -2$, and the second peak is negligible.

Probe measurements at antenna limiter

Density measurements at the input side and output side antenna limiters were performed using the Langmuir probe arrays mounted on the surface facing the antenna. The current-voltage (I-V) characteristics measured by IP1 (input side) and OP1 (output side) probes are shown by black and red traces in Fig. 5.6. The I-V characteristics can be fitted well by exponential functions (dashed lines). A typical discharge used for Langmuir probe measurements is shown in Fig. 5.7. For TST-2 parameters, the measured ion density can be assumed to be the same as the electron density. According to the time dependences of the measured densities, the density measured inside the antenna limiter correlates well with the line-integrated density measured along a vertical chord at $R = 0.39$ m (≈plasma center). At the time of the current jump around 20 ms, the density becomes too

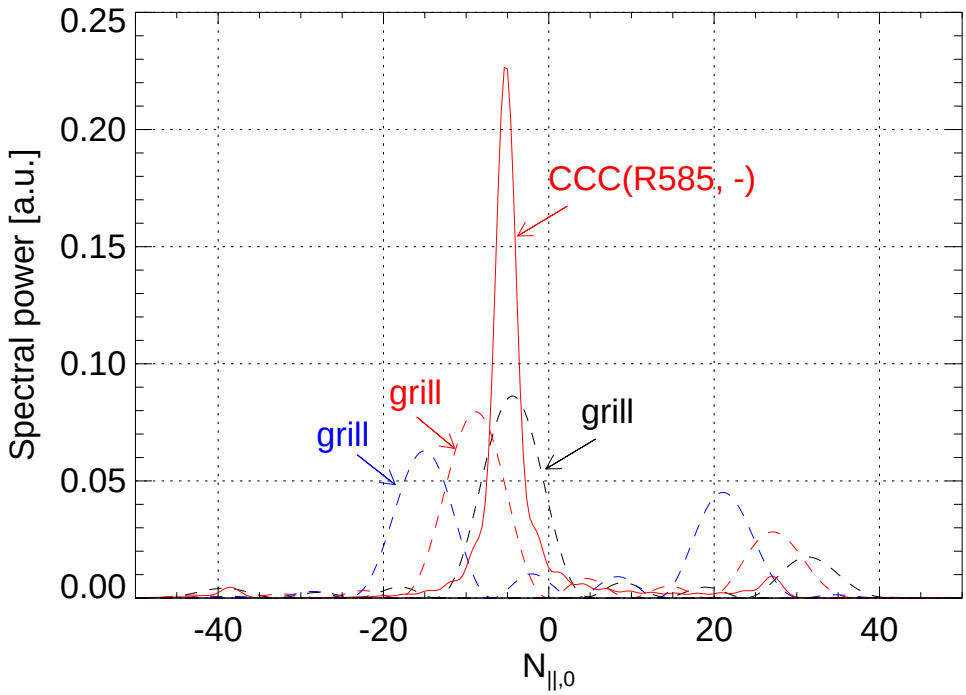

Fig. 5.5: Comparison of the measured $N_{||,0}$ spectra for the CCC antenna (red solid line) with (R585, -) and the grill antenna (dashed line).

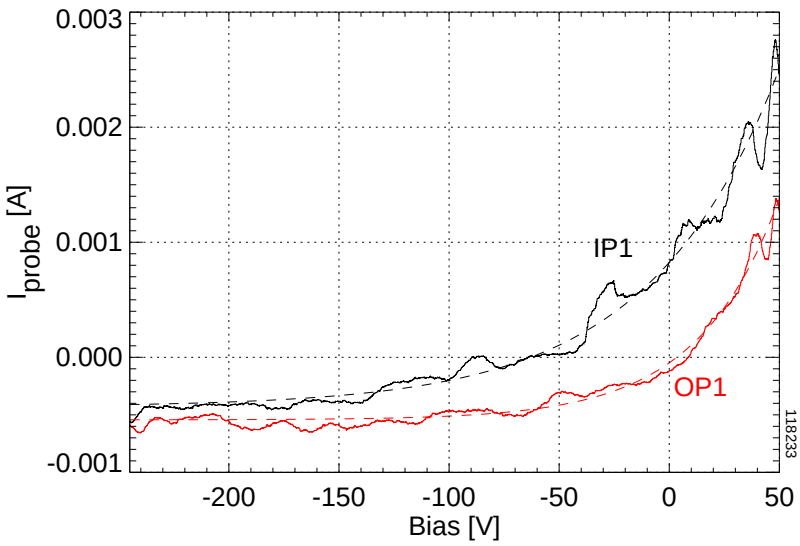

Fig. 5.6: Measured *I*-*V* characteristics obtained using IP1(black) and OP1(red) Langmuir probes. The measured *I*-*V* characteristics ca be fitted with an exponential function to obtain the density and the temperature.

large to be measured by the Langmuir probe. The electron temperature measured inside the antenna limiter is roughly 50 eV, which is roughly consistent with the temperature measured by Thomson scattering measurement near the LCFS. The measured density and temperature are the same between the input side and the output side, but the floating potential is significantly different. The floating potential measured on the input side is approximately -70 V, whereas that measured on the output side is approximately 0 V. According to probe theory, only the floating potential is affected by RF rectification. RF rectification reduces the floating potential, and hence the observed result indicates that the input side is affected by RF rectification but the output side is not. This is reasonable because the RF power at the output side is nearly zero.

The density decay length inside the antenna limiter was derived by fitting the density profile measured by the Langmuir probe array by an exponential function (Fig. 5.8). The result indicates that the decay length is approximately 60 mm, and the density at the antenna surface is higher than the cutoff density ($\approx 5 \times 10^{14}$ m^{-3}). This measurement was performed after sufficient wall and antenna conditioning. After a vacuum vessel opening, the density at $R = 0.585$ m increase up to 10^{16} m^{-3}, and the density decay length is as short as 10–20 mm.

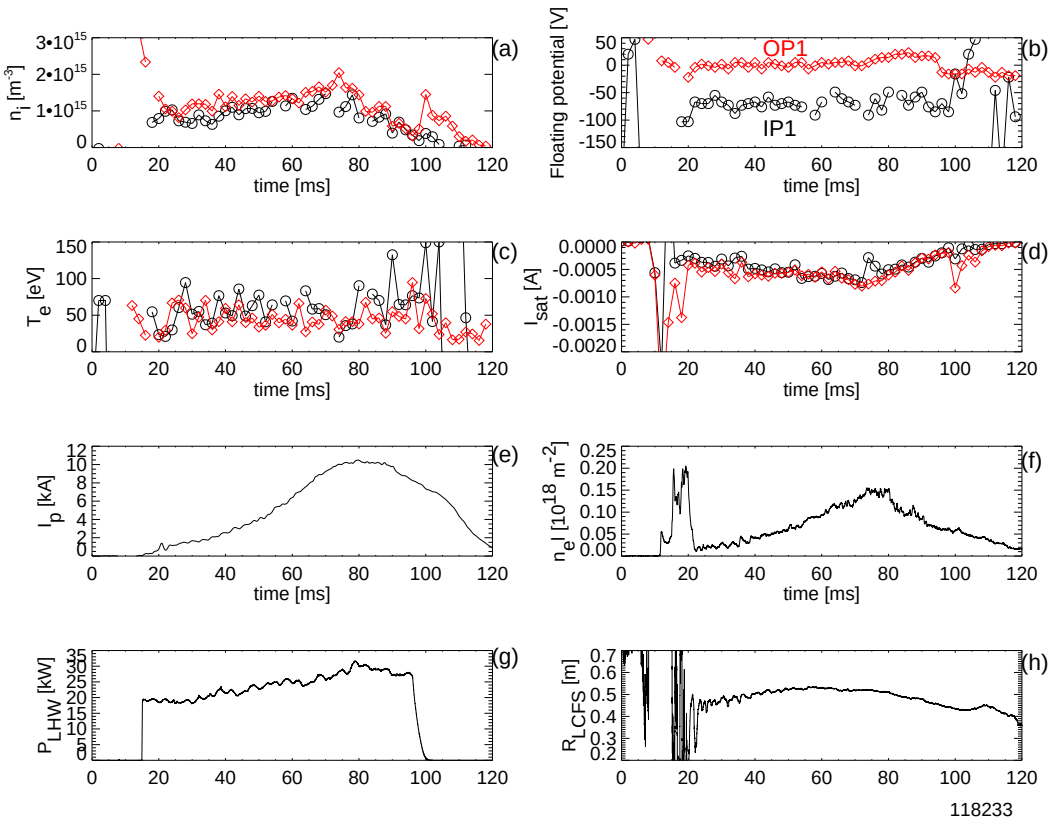

Fig. 5.7: Time evolutions of quantities measured using IP1 (black ∘) and OP1(red ◇) Langmuir probes on the antenna side of the R585 antenna limiter. (a) Ion density, (b) floating potential, (c) electron temperature, (d) ion saturation current, (e)plasma current, (f) line-integrated density along a vertical chord at $R = 0.39$ m, (g) incident LH power, (h) major radius of the outboard LCFS on the midplane.

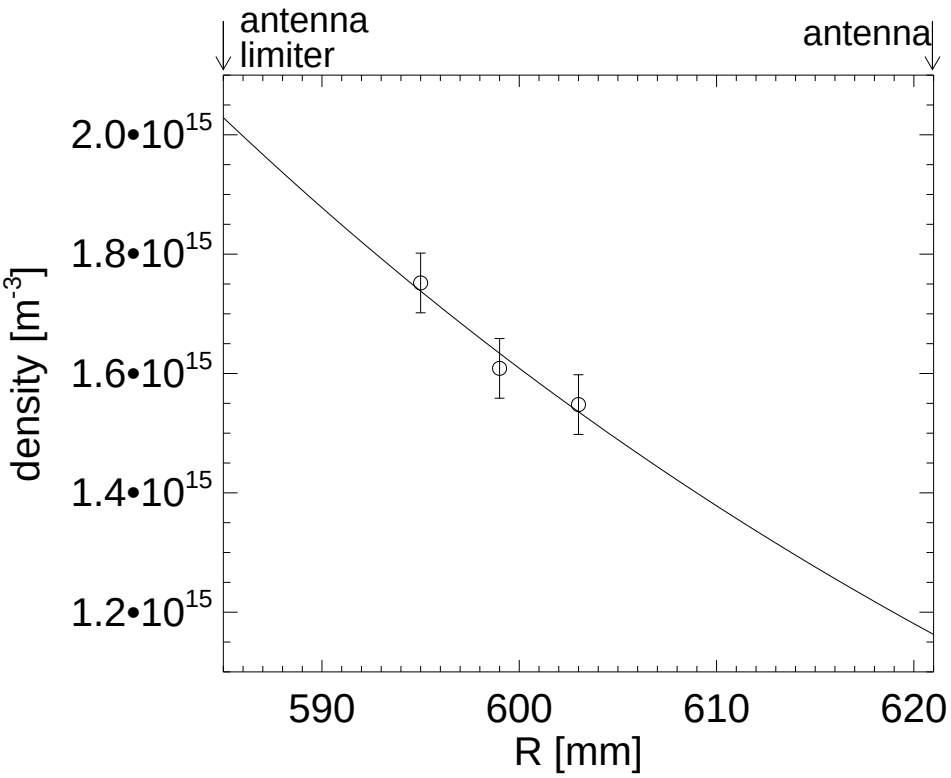

Fig. 5.8: Density profile measured by the Langmuir probe array on the antenna side of the antenna limiter on the output side. The density decay length is approximately 60 mm according to the exponential fit. The density at the antenna surface is higher than the cutoff density ($\approx 5 \times 10^{14}$ m^{-3}).

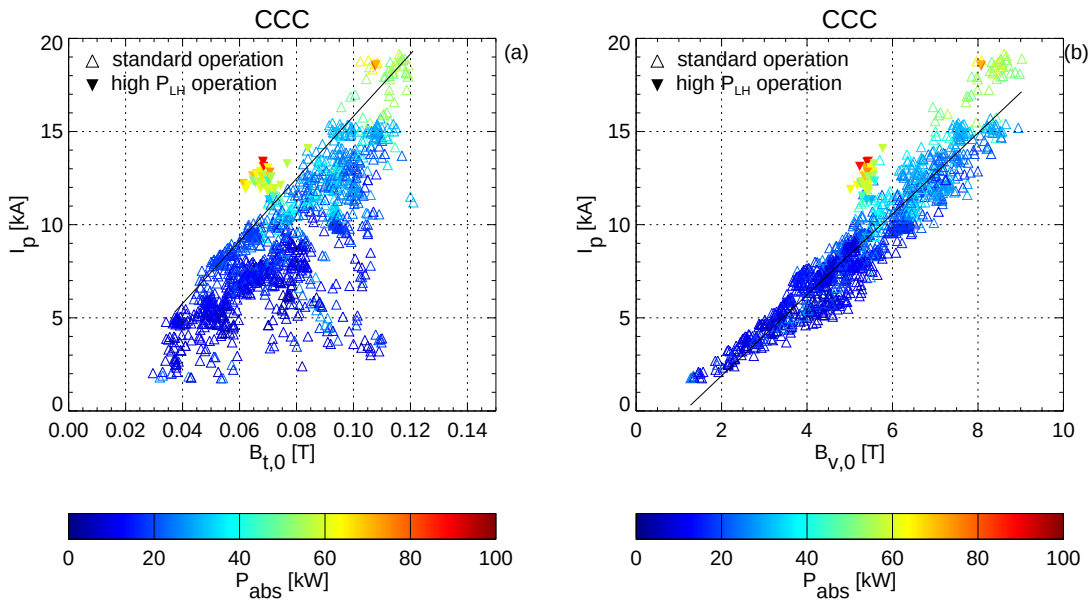

Fig. 5.9: Dependences of the maximum I_p during a discharge achieved with the CCC antenna on a shot-by-shot basis: (a) I_p vs. $B_{t,0}$, (b) I_p vs. $B_{v,0}$.

5.3 Current ramp-up limitations

We succeeded in identifying the plasma parameters which limit I_p ramp-up by analyzing the dependences of I_p on various plasma parameters at the time of maximum I_p on a shot-by-shot basis.

Toroidal field limit

The relationships between I_p and background magnetic fields at the plasma center, $B_{t,0}$ and $B_{v,0}$, were investigated during the CCC antenna campaign (Fig. 5.9). I_p has a linear correlation with $B_{v,0}$ because the toroidal force balance must be satisfied. Interestingly, the maximum I_p also increases with $B_{t,0}$ asI_p[kA] $\approx 168B_{t,\,0}$[T]$-$0.9. In order to investigate the B_t limit more clearly, a controlled B_t scan experiment was performed (Fig. 5.10). The result indicates that I_p is strongly limited by B_t, and the maximum I_p is roughly proportional to $B_{t,0}$ (Fig. 5.11).

The B_t limit will become a serious problem when we challenge to achieve higher I_p by increasing B_t. As described in Chapter 3, the loss by PDI becomes non-negligible when $\omega \leq 2\omega_{LH}$. Since B_t varies greatly in the R direction in an ST, it is difficult to predict the limit in B_t. Suppose the loss condition is first satisfied at the plasma center and the plasma density is successfully suppressed to under

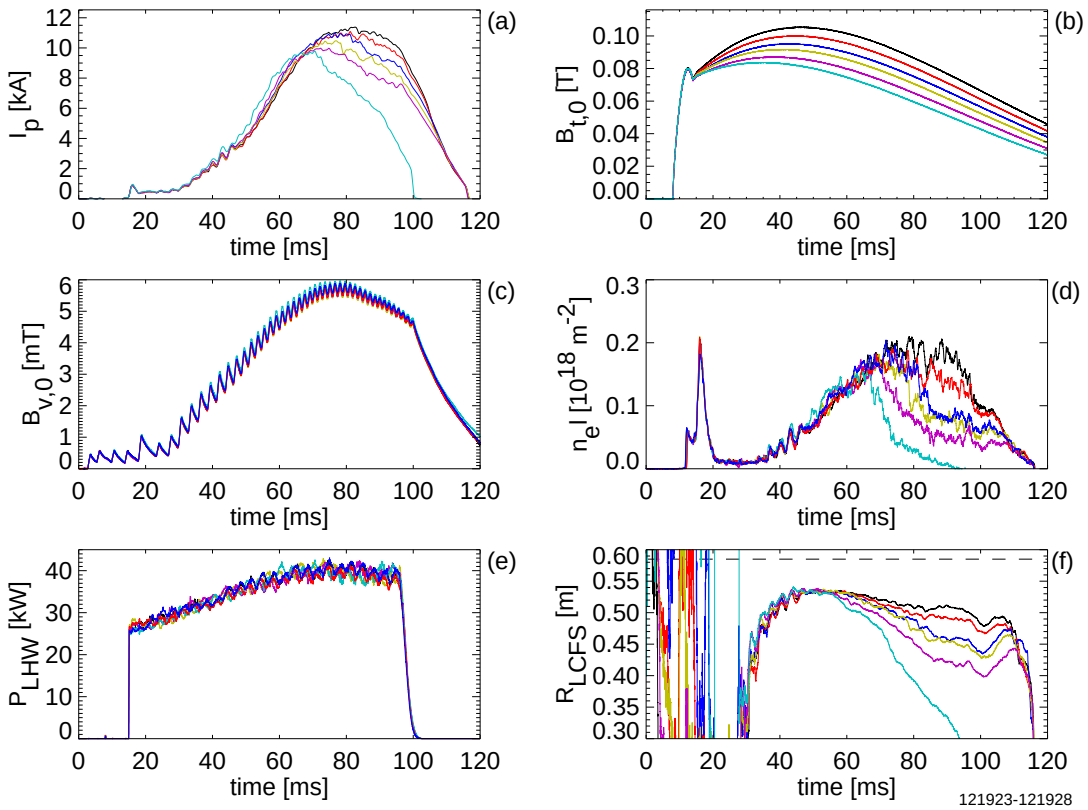

Fig. 5.10: $B_{t,0}$ scan experiment to investigate the dependence of I_p on $B_{t,0}$. Only $B_{t,0}$ was changed shot-by-shot. (a) Plasma current, (b) toroidal magnetic field at the plasma center, (c) vertical field at the plasma center, (d) line-integrated density along a vertical chord through $R = 0.39$ m, (e) incident LHW power, (f) major radius of the outboard LCFS on the midplane.

10^{18}m^{-3}, the loss by PDI becomes serious at $B_t = 0.3$ T with $I_p = 50$ kA if this B_t limit remains valid. If the plasma density increases with I_p, the loss by PDI becomes serious at $B_t = 0.2$ T with $I_p = 33$ kA.

We also found a method to break the B_t limit slightly by launching extra LHW power (triangle pointing down in Fig. 5.9). The extra LHW power expands the plasma volume and increases the plasma density, and contributes slightly to increase I_p. For example, to increase I_p by 3 kA from 10kA, 40 kW of extra LHW power is required. This is equal to the LHW power for $I_p = 10$ kA under standard operation. Since this operation is not efficient, such data points with excessive LH power were removed from the plots.

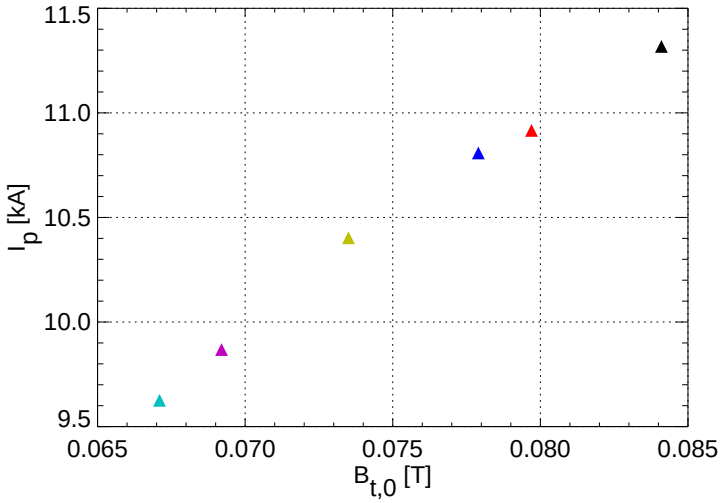

Fig. 5.11: Dependence of maximum I_p on$B_{t,0}$ Obtained from the $B_{t,0}$ scan experiment (Fig. 5.10).

Density limit

There are also plasma density limitations for I_p ramp-up. We observed two cases of density limit, depended on the existence of the upper and lower z450 limiters. In the case without the z450 limiter, I_p started to decline after the line-averaged density reached around 0.4–0.6 $\times 10^{18}$m^{-3}. For TST-2 parameters, it is reasonable to consider the density limit due to mode conversion, but the observed density limit has no clear dependence on B_t (Fig. 5.12(a)). Hence, it was not possible to alleviate the density limit by increasing B_t. As an example a discharge with declined I_p due to the density limit is shown in Fig. 5.13. The plasma current started to decline after the line-integrated density reached $\sim 0.25 \times 10^{18}$m^{-2}.

In the case with the z450 limiter, it was possible to alleviate the density limit by increasing B_t. As shown in Fig. 5.12(b), a good correlation was observed between the experimental data and the mode conversion curve. Hence, it is reasonable to believe that the density limit corresponds to the mode conversion density in the case with the z450 limiter. We were able to ramp up the plasma current successfully up to around 20 kA by alleviating the density limit. Actually, the z450 limiters were installed for another purpose, and it was not expected that limiters located in such far scrape-off layer (the LCFS is around $z \approx \pm 0.3$ m) can affectI_p ramp-up.

In order to investigate the dependence of the density limit on the z450 limiter, two Langmuir probes (U1 and U2) were installed on the upper z450 limiter. The

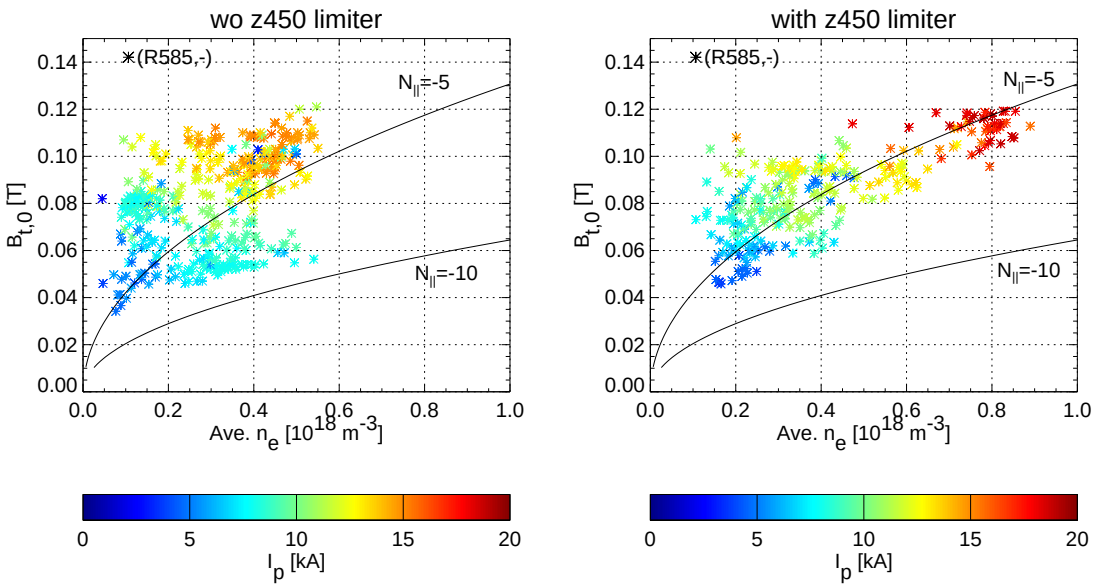

Fig. 5.12: Experimental data for the (R585, -) case plotted on the accessibility map: (a) without the z450 limiter, (b) with the z450 limiter.

measured *I*-*V* characteristics are plotted in Fig. 5.14. The data are fitted well with exponential functions. Time dependences of measured quantities are plotted in Fig. 5.15. The density at the U1 probe, before 60 ms, is sometimes too low to be measured by the probe. According to these results, the density at the z450 limiter is about 2×10^{15} m^{-3}, which is higher than the cutoff density. In addition, the effect of RF rectification was observed at the U1 probe, indicating that the LHW exists around the U1 probe located at (R, z) = (0.275 m, 0.45 m) (Fig. 5.15(b)). The floating potential is affected by the LHW power on the U1 probe, but not on the U2 probe. Thus, we can conclude that the density at the z450 limiter is higher than the cutoff density, and the LHW actually propagates to the U1 probe. In other words, the z450 limiter contributed to reducing the density in the regions $z < -0.45$ m and $z > 0.45$ m. Therefore, it is inferred that the z450 limiters changed the trajectories of the LHW in the SOL, in such a way to break the constant density limit. Although there are no data to support the conjecture directly, the z450 limiters could have contributed to alleviate the losses by ionization in the SOL, dissipation at the wall, ribs, and protruding diagnostics.

We now discuss the relationship between the plasma current and the plasma density. According to studies of the LHW, there is a preferred density for current drive because the density affects the slowing down of RF accelerated fast electrons. We saw in Fig. 5.12(b) that the data tend to cluster around the mode

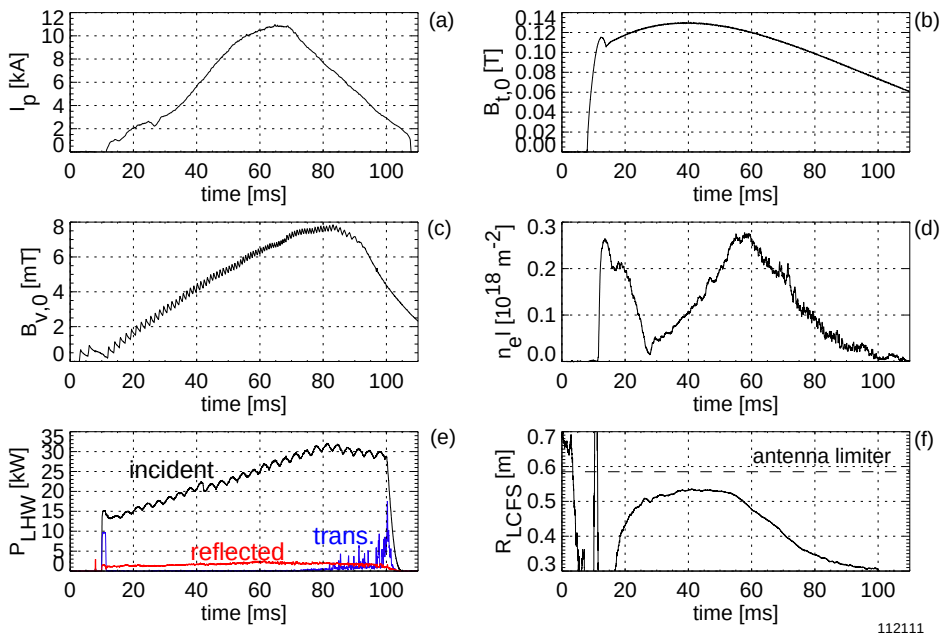

Fig. 5.13: An example of discharge with declining I_p caused by the density limit in the case without the z450 limiter. (a) Plasma current, (b) toroidal magnetic field at the plasma center, (c) vertical field at the plasma center, (d) line-integrated density along a vertical chord at $R = 0.39$ m, (e) LHW power: incident RF power (black), reflected RF power (red), and transmitted RF power (blue), (f) major radius of the outboard LCFS on the midplane.

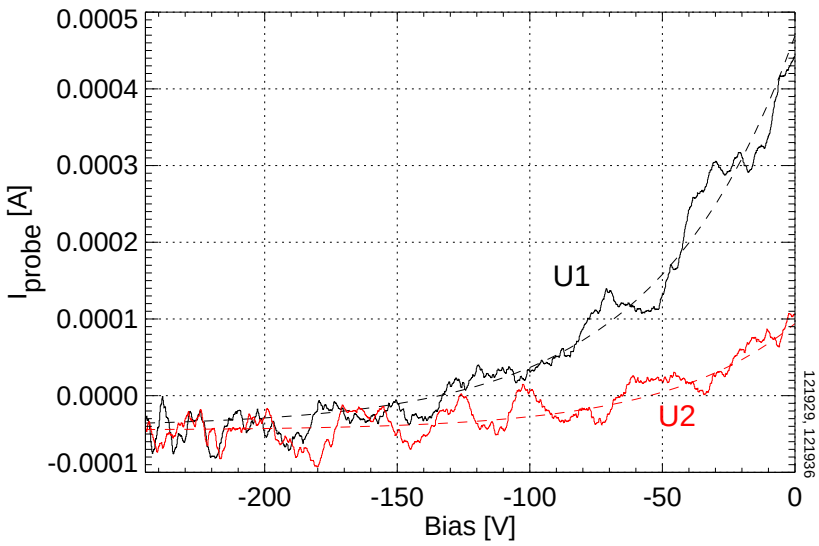

Fig. 5.14: *I*-*V* characteristics of the U1 (black) and U2 (red) Langmuir probes on the z450 limiter. The data are fitted well with exponential functions.

conversion curve, especially at higher plasma currents. Hence, it is experimentally verified that high density, but under the mode conversion density, is advantageous for effective current ramp-up by the LHW. After achieving the preferred density for slowing down, the density should be kept for efficient current ramp-up.

Wave measurements were also performed using RF magnetic probes (RFMPs) on the upper z450 limiter at $(R, z) = (0.223, 0.45)$, (0.295,0.45), (0.367,0.45), (0.439,0.45), and (0.510,0.45) m. Example s of the measured signal and the power spectrum obtained by Fourier transform are shown in Fig. 5.16. Not only the pump wave (~200 MHz), but also the lower side band wave (LSB, < 200 MHz) and the upper side band wave (USB, > 200 MHz) were measured by RFMPs. The decay waves (LSB and USB) are considered as losses because the wavenumber has been shifted away from desired values. In order to investigate the effect of the SOL plasma on the waves, spatial profiles of the pump wave component and the LSB component were compared in a low density plasma and a high density plasma (Fig. 5.17). The results indicate that only the LSB component at $R > 0.35$ m increased with density, implying that the loss in the SOL increases with density. Since the density at the z450 limiter is lower than the cutoff density for the FW, the measured wave must be the SW (LHW). However, the integrated power spectrum at the inboard side is the same as that at the outer board side, which is inconsistent with the result of Langmuir probe measurements on the z450 limiter.

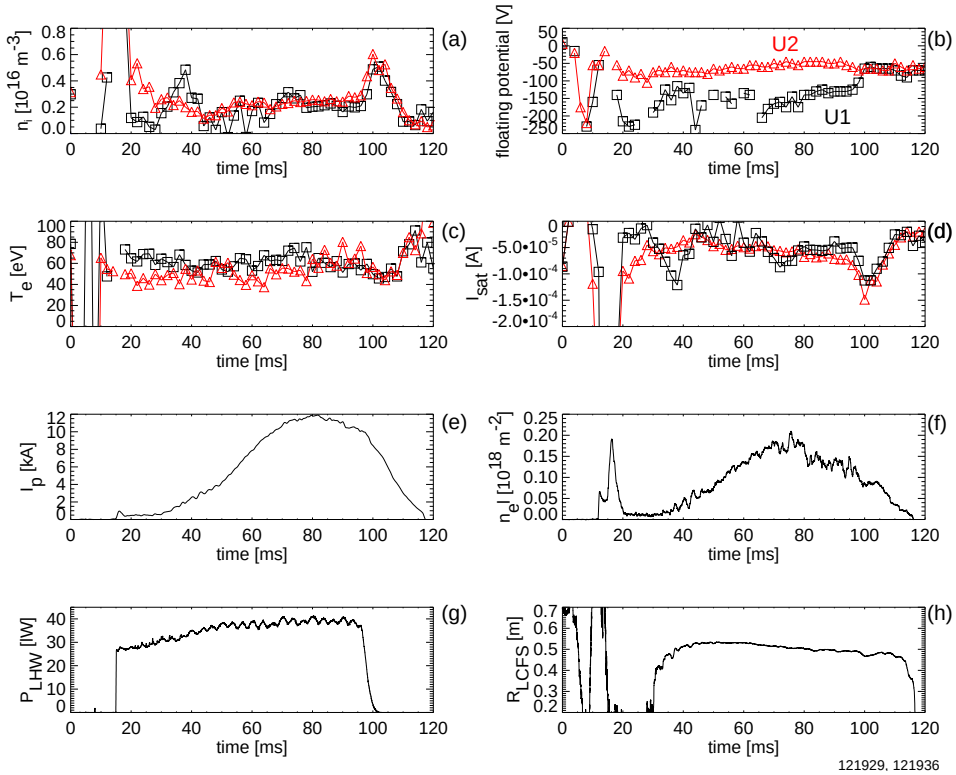

Fig. 5.15: Time dependences of quantities measured by U1 (black □) and OP1 (red △) Langmuir probes on the z450 limiter. (a) Ion density, (b) floating potential, (c) electron temperature, (d) ion saturation current, (e) plasma current, (f) line-integrated density along a vertical chord at $R = 0.39$ m, (g) incident LH power, (h) major radius of the outboard LCFS on the midplane.

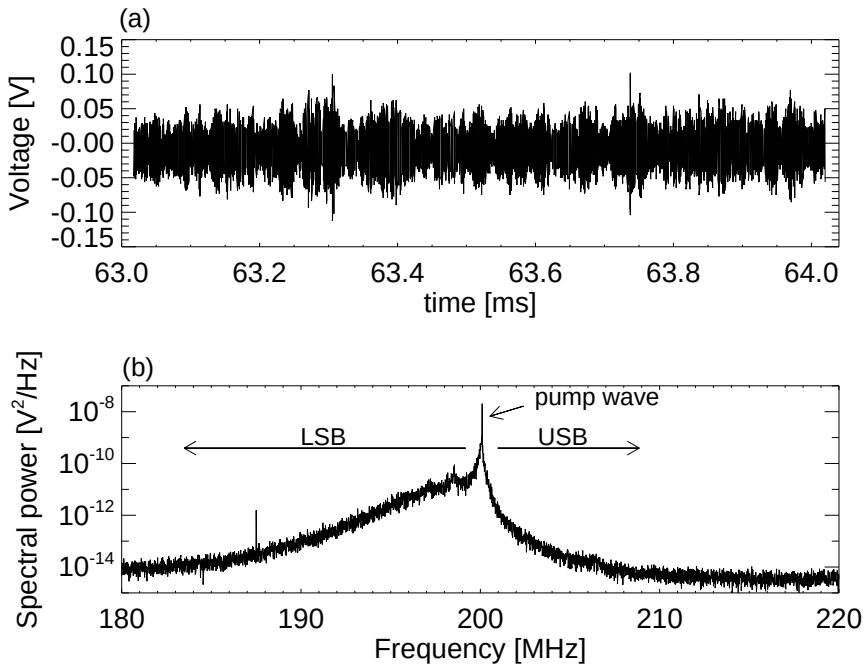

Fig. 5.16: Examples of (a) measured signal and (b) Fourier transformed power spectrum.

According to Langmuir probe measurements, only the probe at inboard side was affected by RF rectification, i.e. the LHW propagated mostly to the inboard side. A possible explanation is that the RFMP measures the electromagnetic component, but the Langmuir probe measures the electrostatic component of the wave. Short wavelength SWs are almost entirely electrostatic. When the wavelength is not sufficiently short, there is a finite electromagnetic component even for the SW. Hence, the waves measured by RFMPs are most likely long wavelength SWs.

$N_{\|,0}$ spectrum limit

In section 5.2, we reported that a sharper $N_{\|,0}$ spectrum can be realized by repositioning the antenna limiter farther towards the plasma (away from the antenna). This reduces the antenna-plasma coupling and increases n_{eff}. It is also important to investigate the relationships between the $N_{\|,0}$ spectrum and plasma parameters. The relationships can be understood from Fig. 5.18, where three limiter configurations are plotted with different symbols ($*$: (R585, -), $\diamond$: (R607, R585), $\times$: (R607, -)). According to these results, the differences are small for I_{p}-$B_{\mathrm{t},0}$ and I_{p}-P_{rad} (Fig. 5.18(a), (c)). For (R585, -) and (R607, -), the required B_{t} was lower

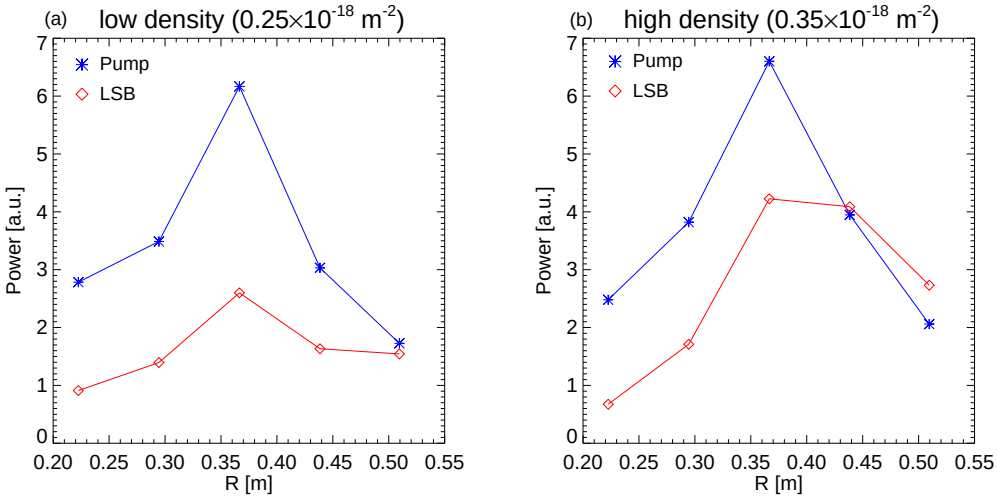

Fig. 5.17: Measured profiles of the frequency integrated power spectrum over the pump wave and the LSB in (a) low density plasma and (b) high density plasma.

than (R607, R585). According to I_p-P_{rad}, data for (R607, R585) might not be enough for reliable analysis, but the required radiated RF power for (R585, -) was lower than (R607, R585). Note that a difference in I_p-P_{rad} can be observed when $I_p \geq 10$ kA. Hence, it is difficult to find a difference in I_p-P_{rad} between (R585, -) and (R607, -) because there are no data substantially over 10 kA for (R607, -).

5.4 Comparison with grill and ICC antennas

In this section, the CCC antenna (LHW antenna, sharp and single-peaked $N_{||,0}$ spectrum), the Grill antenna (LHW antenna, broad and double peaked $N_{||,0}$ spectrum), and the ICC antenna (FW antenna, sharp and single-peaked $N_{||,0}$ spectrum) are compared. Comparison is made with parameters at the time of maximum plasma current. The analyses show that the CCC antenna is special with a high current drive figure of merit, a high antenna-plasma coupling (but also with a sharp $N_{||,0}$ spectrum), and a low reflection coefficient.

Plasma current ramp-up efficiency

First, we focus on the current drive figure of merit which is a common index to evaluate the effectiveness of current drive (Fig. 5.19(a)). In general, the current drive figure of merit is expressed as $\eta_{CD} \equiv I_p \bar{n}_e R_0 / P_{rad}$. The experimental results indicate that η_{CD} obtained with the CCC antenna is higher than the Grill

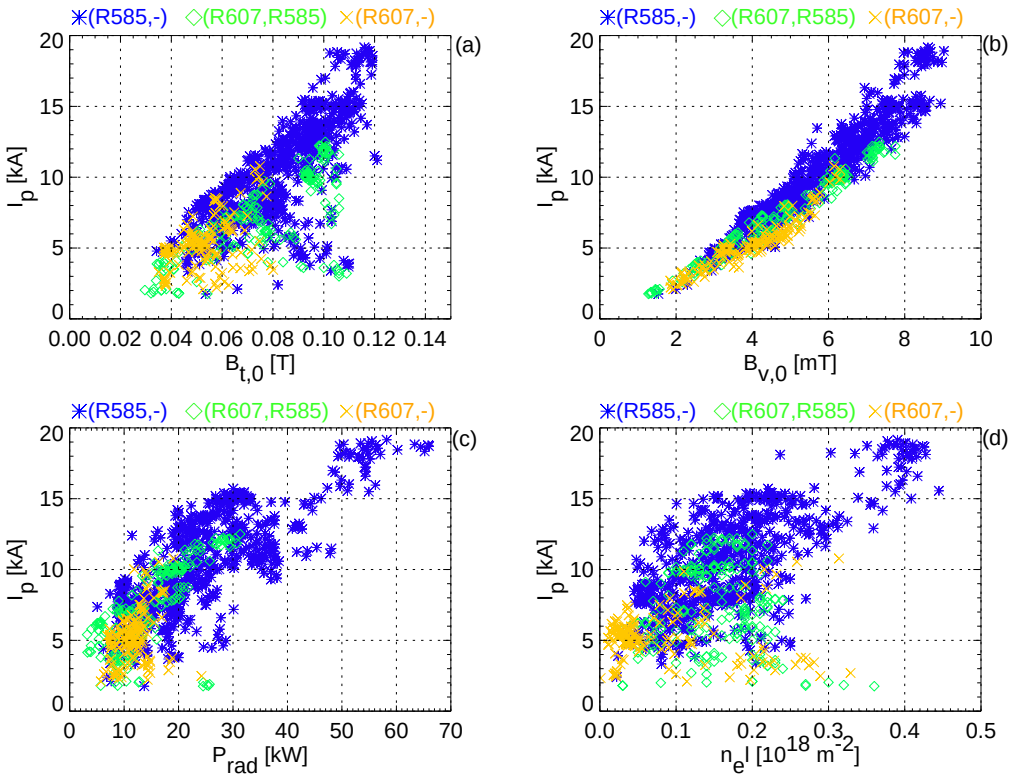

Fig. 5.18: Correlations of the maximum I_p achieved with the CCC antenna and various parameters. Three limiter configurations are plotted with different symbols (∗: (R585, -), ⋄: (R607, R585), ×: (R607, -)). (a) I_p vs. $B_{t,0}$, (b) I_p vs. $B_{v,0}$, (c) I_p vs. P_{rad}, (d) I_p vs. $n_e l$.

antenna of the ICC antenna by a factor of 2–3, especially in the high current region, $I_p \geq 10$ kA. The plasma driven by the CCC antenna maintains a higher plasma density with a lower radiated power, and hence a higher η_{CD} (= except the u/b limiter case) (Fig. 5.19(e), (f)). In addition to high η_{CD}, the required RF power into the CCC antenna is much lower than the Grill antenna or the ICC antenna (Fig. 5.19(b)). For example, the required RF power for 15 kA is only 30 kW for the CCC antenna, but 140 kW of RF power was necessary for the ICC antenna. The difference is caused by antenna-plasma coupling. CCC and ICC antennas are combline-type antennas, and hence the coupling efficiency can be evaluated as $P_{rad}/(P_{fwd} - P_{ref})$ (Fig. 5.19(c)). The coupling efficiency was only 40% to achieve 15 kA with the ICC antenna, but 100% coupling efficiency was achieved with the CCC antenna. In addition to perfect coupling, the $N_{\|,0}$ spectrum remains sharp as described in Sec. 5.2. According to the coupling-I_p relationship for the ICC antenna, the coupling efficiency becomes worse as the plasma current becomes higher. For the Grill antenna, the coupling efficiency can be defined as P_{ref}/P_{fwd}. The results indicate that the coupling efficiency for 10 kA is roughly 40–80%. According to preliminary experiments with the Grill antenna, the RF ponderomotive force reduces the density in front of the antenna, and causes a low coupling efficiency [59]. The reflected powers from CCC and ICC antennas are negligibly small because the input impedance is nearly 50Ω.

Second, the efficiency of radiated RF power was investigated. The I_p-P_{rad} relationship straightforwardly provides the quality of the radiated wave (Fig. 5.19(e)). It is clear that the efficiency is higher for the CCC antenna than for the ICC antenna. For example, ramp-up to 15 kA was achieved with only 25 kW of radiated RF power from the CCC antenna, but 50 kW of radiated RF power was necessary from the ICC antenna. This indicates that the LHW contributes to I_p ramp-up more effectively than the FW. For the Grill antenna, the efficiency is comparable to the CCC antenna case for $I_p \leq 10$ kA. This result also indicates that a sharp $N_{\|,0}$ spectrum is not necessary for $I_p \leq 10$ kA. This is equivalent to the (R607, -) case for the CCC antenna as described in Sec. 5.3. The maximum I_p achieved with the Grill antenna is around 10 kA. This is also equivalent to the (R607, -) case for the CCC antenna. Thus, it is difficult to evaluate the dependence of the I_p ramp-up efficiency on the $N_{\|,0}$ spectrum from the obtained results. However, it might be reasonable that a sharp $N_{\|,0}$ spectrum is advantageous to achieve I_p over 10 kA.

Current ramp-up limitation

The dependences of the plasma current on the background magnetic fields (B_t and B_v) were investigated for the three antennas (Fig. 5.20(a), (b)). The B_t limit and the B_v limit were observed for the Grill antenna and the ICC antenna also. The positive correlation between I_p and $B_{t,0}$ was observed for all three antennas. For

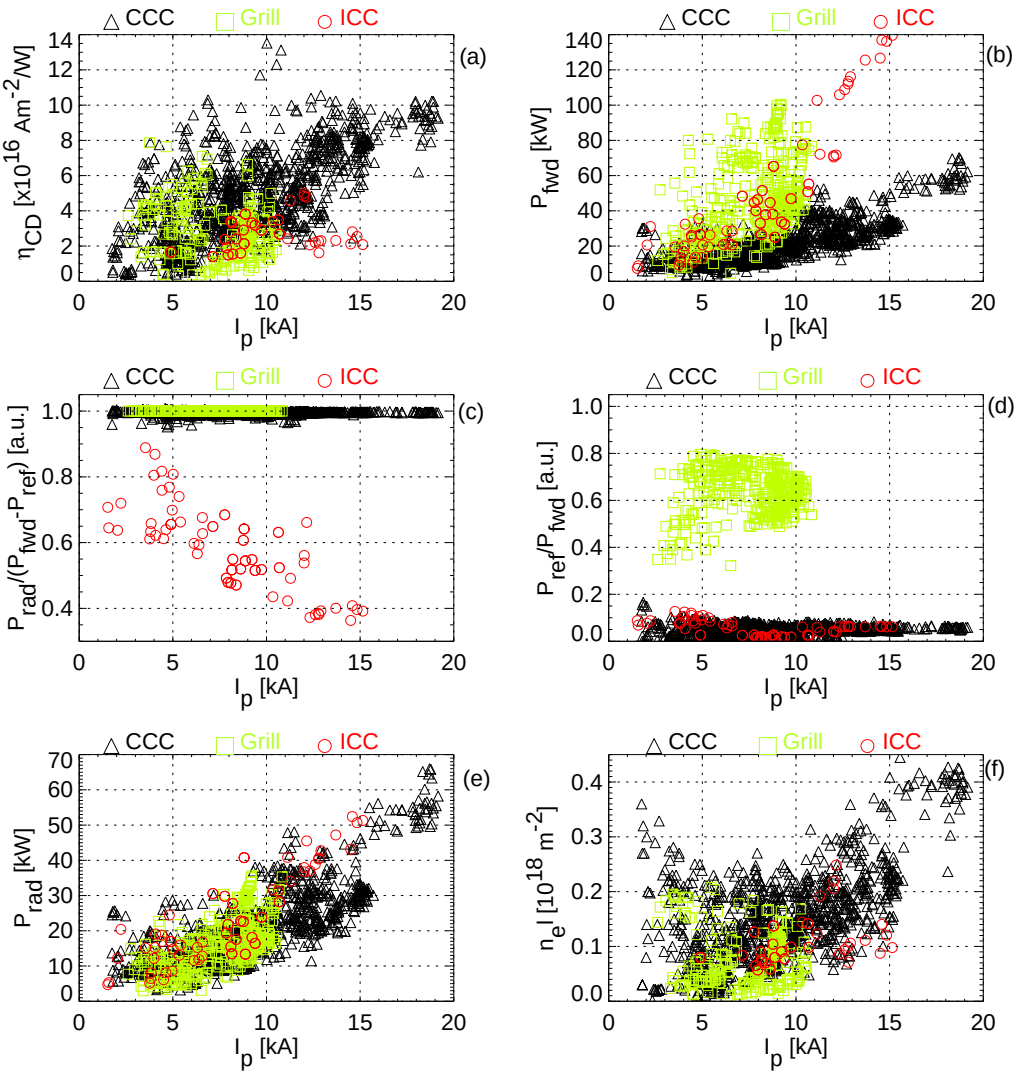

Fig. 5.19: Comparison of antenna efficiency among CCC antenna (black △), Grill antenna (green □), and ICC antenna (red ○). Parameters at the time of maximum I_p are plotted. (a) η_{CD} vs. I_p, (b) P_{fwd} vs. I_p, (c) $P_{rad}/(P_{fwd} - P_{ref})$ vs. I_p, (d) P_{ref}/P_{fwd} vs. I_p, (e) P_{rad} vs. I_p, (f) $n_e l$ vs. I_p.

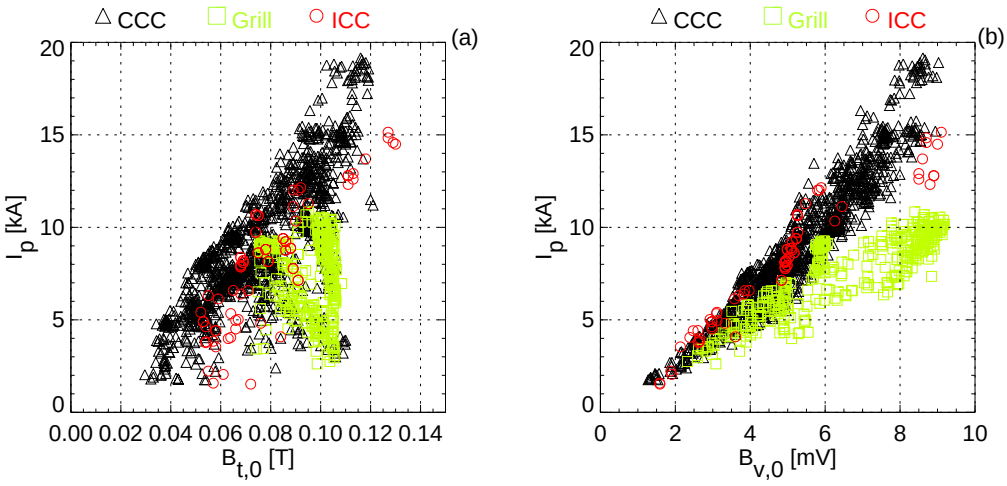

Fig. 5.20: Plasma parameters at the time of maximum I_p for CCC antenna (black △), Grill antenna (green □), and ICC antenna (red ○). (a) I_p vs. $B_{t,0}$, (b) I_p vs. $B_{v,0}$.

the CCC antenna, the required $B_{t,0}$ for the same I_p is slightly lower than the Grill antenna of the ICC antenna. The required $B_{v,0}$ for the Grill antenna is higher than the other two antennas. The I_p-$B_{v,0}$ relationship is based on the toroidal force balance of the plasma, and hence the relationship depends on the plasma size. The antenna limiter for the Grill antenna was located at R = 0.64 m, whereas the antenna limiters for the CCC and ICC antennas were located at R = 0.585 m and R = 0.590 m, respectively. Hence, the size of the plasma produced by the Grill antenna is larger than plasmas produced by CCC and ICC antennas, and a greater $B_{v,0}$ was necessary for plasmas produced by the Grill antenna.

5.5 Density suppression

We succeeded in inventing a plasma density suppression method for TST-2 plasmas driven by the LHW. In an ST with a low toroidal magnetic field, successful I_p ramp-up by the LHW can be achieved only when the plasma density is kept at a low enough level, since a high density plasma prevents the LHW from penetrating to the plasma core. If the density becomes too high, I_p starts to decline as described in Sec. 5.3. Therefore, we needed to develop a method to reduce the plasma density during the I_p ramp-up phase.

Effects of the ECW in LHW driven plasmas were observed on WT-2 and WT-3 tokamaks [29,64]. In WT-2, the ECW caused an I_p increase and a density decrease when the EC resonance was positioned on the outboard side of the magnetic axis. Conversely, I_p decreased and the density increased when EC heating was applied to the bulk electrons. Thus, the ECW can help LHW current drive if the EC resonance layer is positioned appropriately.

The effects of ECW (2.45 GHz) on plasmas ramped up by LHW current drive were investigated on TST-2 without the z450 limiter with the density limit around 0.2–$0.3 \times 10^{18}\,\mathrm{m}^{-2}$. The ECW was launched into the plasma with the fundamental EC resonance located at the nominal plasma center ($R \approx 0.38\,\mathrm{m}$, with $P_{\mathrm{EC}} \simeq 2\,\mathrm{kW}$). The LHW power injected by the CCC antenna was gradually increased to 30 kW. Note that the ECW power was lower than the LHW power by a factor of 15 at the end of the LHW pulse. The line integrated density was measured along a vertical chord at $R = 0.39$ m, and the D_α line emission (which includes the H_α line emission due to a low spectral resolution) was measured from the outboard midplane. .

In order to evaluate the effect of the ECW, only the ECW pulse length was varied in the three discharges shown in Fig. 5.21. In the discharge shown by the black line, the ECW power was turned off at 70 ms. The plasma current was increased successfully to 12.6 kA. Plasma current ramp-up continued while the vertical field (B_v) was being increased. Note that $n_e l$ was kept below $0.21 \times 10^{18}\,\mathrm{m}^{-2}$ throughout the discharge. For the case in which the ECW injection ended at 70 ms, the decline of the plasma current was caused by insufficient B_v. In the discharge shown by the red line, the ECW was turned off at 60 ms. Although the plasma current ramp-up rate remained the same after ECW turn-off, the rate of increase of both $n_e l$ and D_α emission increased abruptly after a delay of a few ms, and the plasma current started to decline after reaching 11.9 kA, and $n_e l$ increased to $0.24 \times 10^{18}\,\mathrm{m}^{-2}$ from $0.21 \times 10^{18}\,\mathrm{m}^{-2}$. In the discharge shown by the blue line, the ECW was turned off at 50 ms. The $n_e l$ and D_α increases started earlier and the plasma current started to decline after reaching 10.8 kA. Thus, the ECW injection contributed to keep the density under the density limit. The plasma current ramp-up rate is not directly affected by the low power ECW. Rather, the $n_e l$ and D_α

increases which are observed in the absence of ECW are suppressed by ECW injection. Thus, ECW is effective in reducing the plasma density in spite of the low power. The decrease in $n_e l$ (more precisely, the suppression of a $n_e l$ increase) is approximately 10%.

Note that the density suppression occurred when the EC resonance layer was located at the plasma center, whereas it was located on the outboard side in WT-2 and WT-3. If we assume that heating in the edge region of the plasma contributes to density suppression, the TST-2 results are consistent with the results of WT-2 and WT-3 because the bulk density is sufficiently higher than the cutoff density in TST-2. For ECW of 2.45 GHz in TST-2, the O-mode cutoff density is approximately $7\times10^{16}\mathrm{m}^{-3}$ and the X-mode cutoff density is roughly 10^{16}–$10^{17}\mathrm{m}^{-3}$. Thus, it is reasonable to assume that the heating by ECW occurs mainly in the edge of TST-2 plasma.

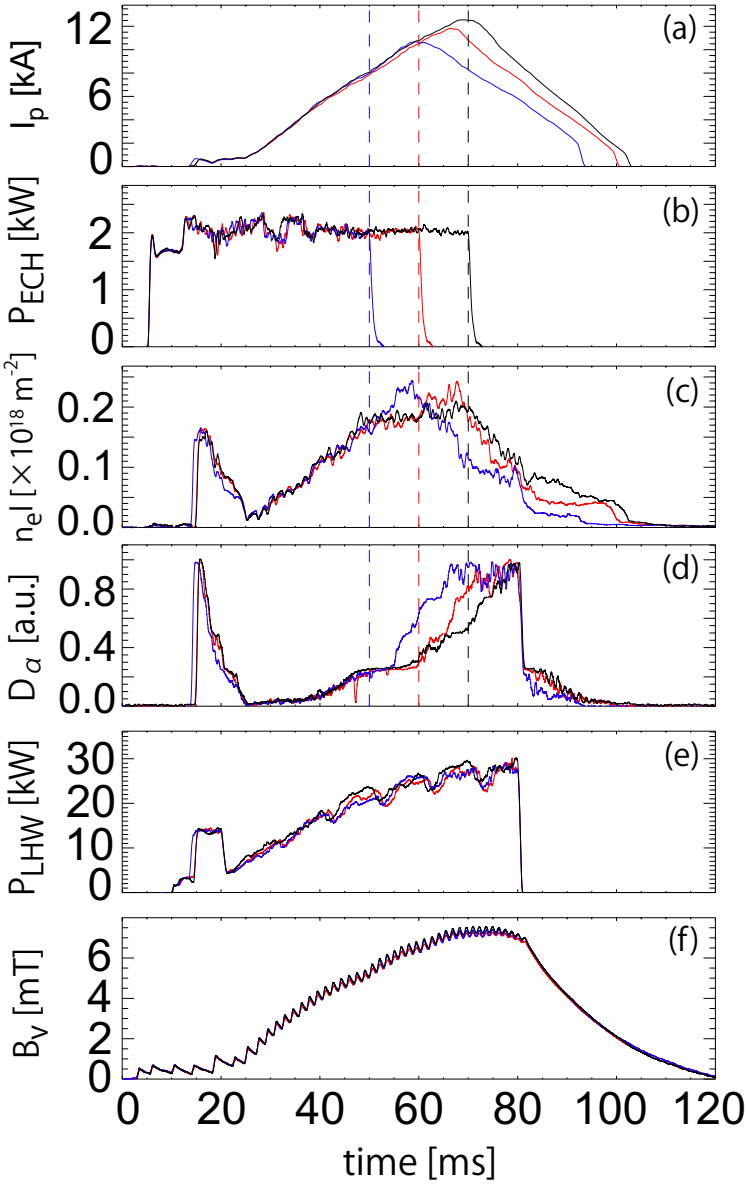

Fig. 5.21: Waveforms of (a) plasma current, (b) ECW injected power, (c) LHW injected power, (d) line integrated density through the central vertical chord (path length ~ 0.5 m), (e) D_α line emission, (f) vertical field at the plasma center. Only the ECW pulse length is different in the three discharges shown [65].

Chapter 6

Discussion

6.1 Wavenumber up-shift in TST-2

The theoretical condition for strong absorption of the LHW in the bulk plasma is $|N_{\|}|T_{\mathrm{e}}^{1/2} \geq 5$–7. During the ramp-up phase, it is difficult to predict the evolution of the electron temperature with the ramping plasma current. As described in Chapter 3, the optimum range for high current drive efficiency was determined to be $-6 \leq N_{\|,0} \leq -2$ based on LH current ramp-up experiments with the grill antenna on TST-2. Since the Thomson scattering measurement was not yet available for the grill antenna campaign, there are no electron temperature data. The electron temperature measurement was first performed during the CCC antenna campaign, and it was found that the electron temperature is too low to absorb the injected LHW with $-6 \leq N_{\|} \leq -2$. The measured temperature, 0.01–0.03 keV at the plasma center, leads to $|N_{\|}|T_{\mathrm{e}}^{1/2} = 0.6$–$1 < 5$–7. According to ray-tracing calculations using the GENRAY code [57] for TST-2 parameters, a large up-shift in the parallel wavenumber occurs after bouncing from the upper side boundary of the plasma (Fig. 6.1, Chapter 2). Hence, it is reasonable to believe that the up-shifted LHW contributed to current ramp-up in such a low temperature plasma during the early ramp-up phase. In this calculation, ray propagation was limited to the region inside the LCFS.

6.2 LHW power losses in TST-2

Calculated LHW ray patterns for the experimental condition are summarized in Fig. 6.2. Important losses are absorption in the SOL region and absorption near the LCFS which can result in a rapid loss.

We successfully achieved I_{p} ramp-up to 20 kA after installing the upper and lower limiter at $z = \pm 0.45$ m (z450 limiter), which broke the constant density

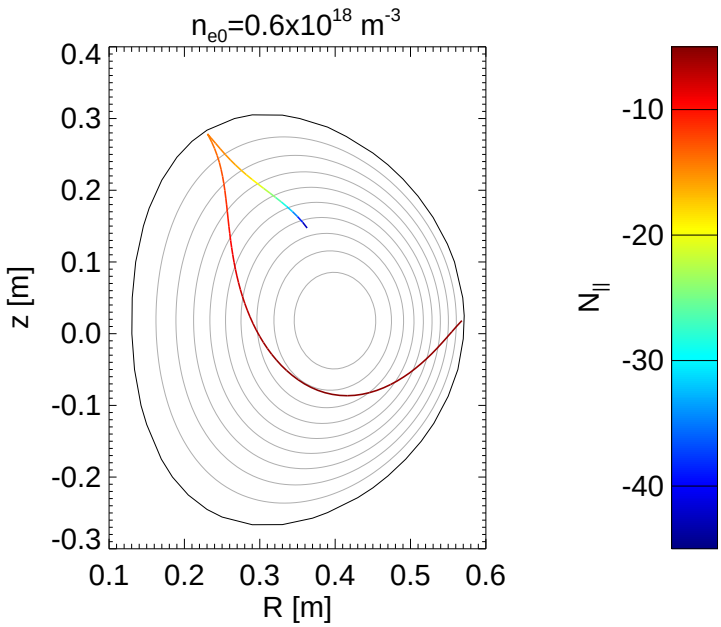

Fig. 6.1: Example of ray-tracing calculation using GENRAY with $N_{\|,0} = -5.5$ for TST-2 parameters. A rapid $N_{\|}$ up-shift occurs after bouncing from the upper plasma boundary. The region outside the LCFS is assumed to be vacuum.

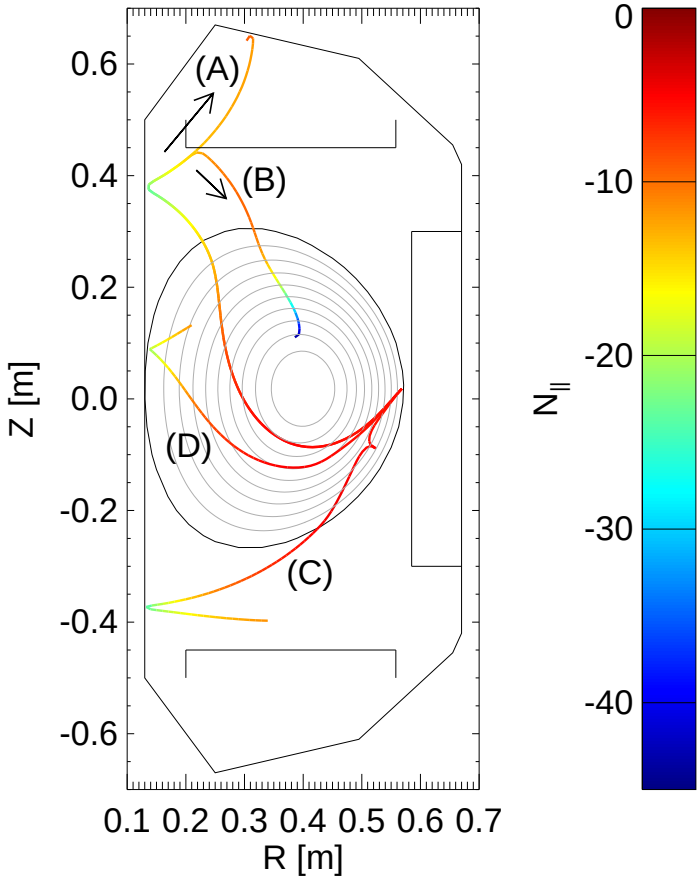

Fig. 6.2: Calculated ray patterns for the experimental condition. Ray propagations are stopped when they complete the trajectory needed for explanation. (A) There is a substantial loss in the SOL for the case without the z450 limiter, and there is a density limit. (B) Strong absorption in the plasma core is expected due to a large up-shift in the parallel wavenumber after reflection from the z450 limiter, which can contribute efficiently to current ramp-up. (C) The LHW is inaccessible to top of the plasma due to mode conversion (density limit for the z450 limiter case), which causes loss in the lower SOL. (D) Due to a large up-shift inside the LCFS, the LHW can be absorbed in the vicinity of the inboard wall where T_e is measured to be high, and can be lost easily. (A–C) The large up-shift, occurring outside the LCFS in the vicinity of the inboard boundary also results in LHW power loss.

limit observed around $\overline{n}_e \approx 0.4$–$0.6 \times 10^{18}\mathrm{m}^{-3}$. It is reasonable to assume that the z450 limiter alleviated the loss of LHW in the SOL (Fig. 6.2(A), (B)). According to Langmuir probe measurements at the upper z450 limiter, the density at $z = 0.45$ m is higher than the cutoff density, and the observed RF rectification directly indicates that the LHW propagates to $(R, z) \approx (0.28, 0.45)$ m. These results also imply that the z450 limiter alleviates the SOL loss. After installing the z450 limiter, the observed density limit correlates well with the density limit due to mode conversion. The mode conversion density increases as the toroidal magnetic field is increased, and hence we could operate at higher densities and achieve higher I_p. The measured density limit coincides with the mode conversion density for $N_\parallel = -5$, which is nearly the same as the peak of the launched spectrum, $N_\parallel = -5.5$. As described in the previous section, it is reasonable to believe that the up-shifted LHW, reflecting from the upper side of the plasma, contributed to I_p ramp-up. According to the obtained result that the density limit approximately coincides with the mode conversion density for the injected $N_\parallel$, after the first-pass without strong absorption, the injected LHW ends up bouncing from the upper plasma boundary with a subsequent large up-shift (Fig. 6.2(B)). If the density is higher than the mode conversion density, the LHW is bent toward the lower boundary of plasma (Fig. 6.2(C)). Hence, it is difficult to expect that the LHW finally reaches the upper boundary without serious losses and penetrate into the plasma core with a large up-shift.

The electron temperature profile measured in a plasma successfully ramped up by the LHW was hollow (Fig. 5.2). This result implies that the LHW power is deposited mainly in the vicinity of the LCFS due to a large up-shift. In this case, the conservation of toroidal mode number causes a large up-shift when the LHW reaches the inboard side (Fig. 6.2(D)). Since the LHW is excited by the antenna at $R = 0.621$ and the inboard boundary is at $R = 0.126$ m, the parallel refractive index up-shifts to $N_\parallel \approx N_{\parallel,0} R_a / R = -5.5 \cdot 0.621/0.126 \approx -27$. The large up-shift is confirmed by ray-tracing calculation (Fig. 6.2(A–D)). For cases (A–C), a large up-shift occurs outside the LCFS, and becomes a loss. A large up-shift also occurs inside the LCFS such as in case (D). However, it is difficult to determine experimentally whether the electrons accelerated in the vicinity of the inboard edge contribute to current ramp-up. For effective I_p ramp-up, a large up-shift in the plasma core is preferable, such as case (B).

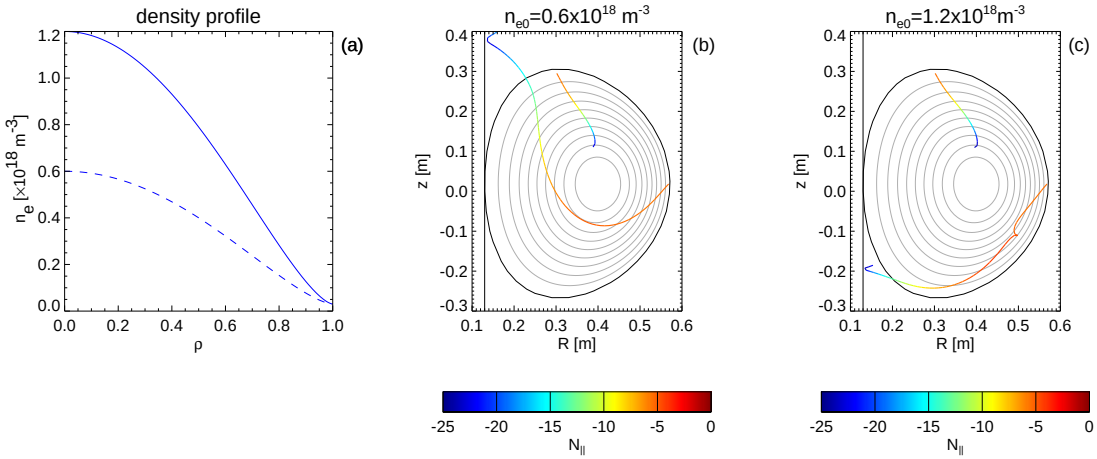

Fig. 6.3: Comparison of top-launch and outboard-launch LHW rays. (a) Standard density profile (dashed line) and higher density profile (solid line). (b) LHW rays launched from the top and from the outboard midplane for the standard density case. (c) LHW rays launched from the top and from the outboard midplane for the higher density case.

6.3 Top-launch CCC antenna

6.3.1 Concept

Top-launch of the LHW is expected to provide efficient I_p ramp-up. As described in the previous section, up-shifted LHW propagating from the upper side of the plasma is needed for absorption and bulk current drive in low temperature TST-2 plasmas. However, if the LHW is launched from the outboard side, losses in the plasma periphery are considerable before the LHW can obtain a large up-shift by reflecting from the upper side of the plasma. Thus, we developed an innovative top-launch antenna. As shown in Fig. 6.3, the LHW launched from the top is up-shifted immediately as it propagates into the plasma. In addition to the up-shift, the LHW accessibility condition is improved due to the higher toroidal magnetic field at smaller major radii (by a factor of two compared to the outboard-launch). As shown in Fig. 6.3(a), (b) the LHW launched from the top propagates into the plasm core in spite of the high density, which is inaccessible for the LHW launched from the outboard side. Propagation of the top-launched LHW is hardly affected by plasma parameters. It is also of interest to see how the B_t limit will change. If the B_t limit is subject to propagation of the LHW, the B_t limit will be broken by top-launching. Hence it is possible to achieve higher plasma currents without upgrading the TF coil power supply.

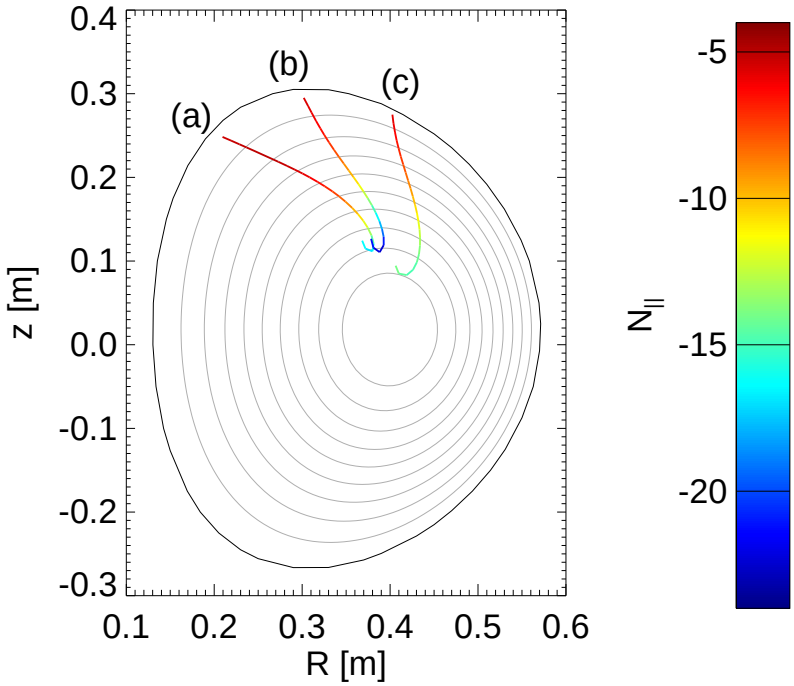

Fig. 6.4: Ray-tracing calculations for three different poloidal launching positions: (a) (R, z) = (0.22 m, 0.25 m), (b) (R, z) = (0.30 m, 0.30 m), and (c) (R, z) = (0.40 m, 0.28 m). The rays are stopped when they turn around near the plasma center.

6.3.2 Ray-tracing analysis

In order to investigate the optimum poloidal position of wave launch, ray-tracing calculations were performed for rays with $N_{\|,0} \approx -5.5$ launched from three different poloidal positions (Fig. 6.4). The rays were launched at (a) (R, z) = (0.22 m, 0.25 m), (b) (R, z) = (0.30 m, 0.30 m), and (c) (R, z) = (0.40 m, 0.28 m). All three rays undergo up-shift, but the largest up-shift occurs for case (b) . In addition, this poloidal position is suitable for installing the top-launch antenna because the plasma position along R does not affect wave launching, and we can use ample space available at the upper side of the plasma. Thus, we decided to launch the LHW from (R, z) = (0.30 m, 0.30 m).

6.3.3 Design

The top-launch antenna was developed in collaboration with GA. The electrical properties of the top-antenna is the same as the outboard-launch CCC antenna. However, it is not possible to install an antenna with the same structure at the top of the plasma. There is ample space in the z direction, but not in the R direction. Hence, the inductive rods are extended in the z direction (Fig. 6.5). Assuming a similar coupling efficiency as the outboard-launch CCC antenna, the top-launch antenna surface is placed at $z \approx 0.335$ m with the antenna limiter installed at $z = 0.300$ m. A drawing of the top-launch antenna in TST-2 is shown in Fig. 6.6. We installed six elements because the experimental results with the outboard-launch CCC antenna indicate that six elements are sufficient to launch a sharp, single-peaked $N_{\|,0}$ spectrum. We plan to launch the LHW with $N_{\|,0} \approx -5$ to make a direct comparison with the outboard-launch antenna. Since we want to excite a single-peaked spectrum, the number of wavelengths of the electric field in front of the antenna should be greater than one. The phase difference between adjacent elements is -90 degrees, so there are one and a half wavelengths in front of the antenna. The top-launch CCC antenna excites a backward wave. The gap width between adjacent elements is constant along R (major radial direction) so the electric field is nearly constant along R. Since the radiating element is wedge-shaped, the toroidal mode number is also constant along R, and hence the peak of the $N_{\|,0}$ spectrum becomes smaller along R as $1/R$.

6.3.4 Impedance matching and $N_{\|,0}$ adjustment

Calibration of the top-launch CCC antenna was performed with the NWA as explained in Sec. 4.2. The impedance was adjusted to 50Ω by changing the positions of the inductor short points and feed points. Low reflectivities were obtained in the range 193 to 205 MHz after adjustment (Fig. 6.7). The transmission power was approximately 83 %, and the other 17 % is lost by radiation into air and resistive loss in the antenna. After tuning, the phase shift between adjacent elements was -85 ± 20 degrees. The phase was measured by a 1-turn loop magnetic probe and an electrostatic (ES) probe. The phase was measured by the magnetic probe at the short points (= end of the elements) where the magnetic field is largest. The measurement of the phase with the ES probe was performed between the radiating parts where the electric field is largest. It is also possible to measure the phase between side covers and the elements with the ES probe (element number = 0.5 and 6.5). The obtained spectrum with the two instruments are shown in Fig. 6.8. The results of measurements using two types of probes are nearly the same and the peak of the $N_{\|,0}$ spectrum is -4 at $R = 0.285$ m (= antenna center along R in TST-2). This value is slightly smaller than the expected value of -5.

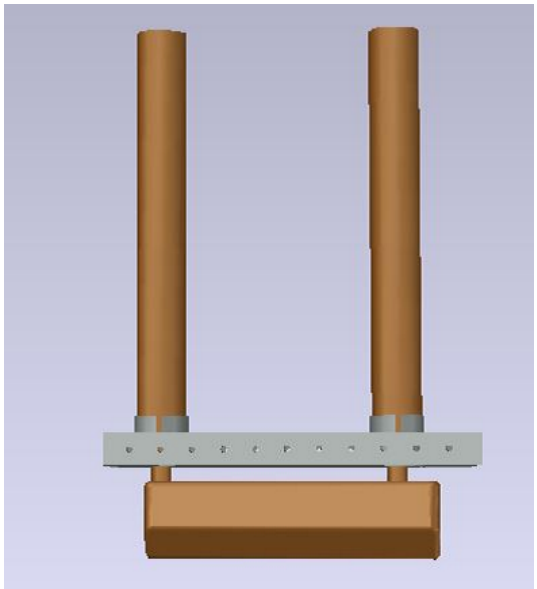

Fig. 6.5: One element of the top-launch antenna. The electrical properties are the same as the outboard-launch CCC antenna. The inductive rods are extended in the *z* direction.

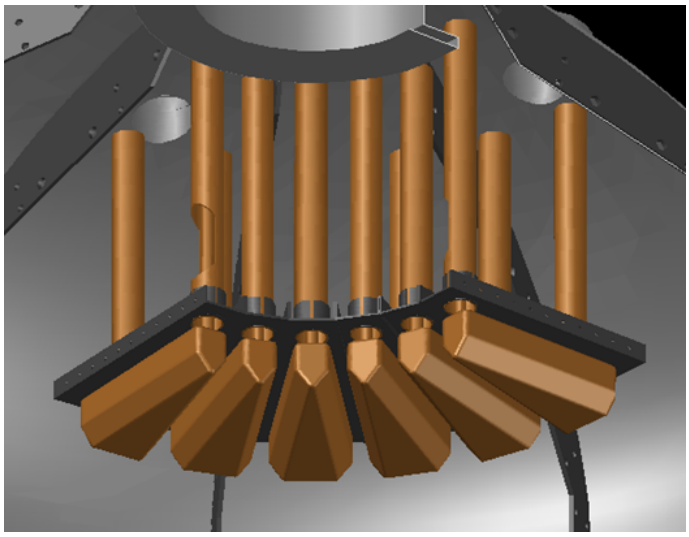

Fig. 6.6: 3-E model of the top-launch CCC antenna installed in TST-2.

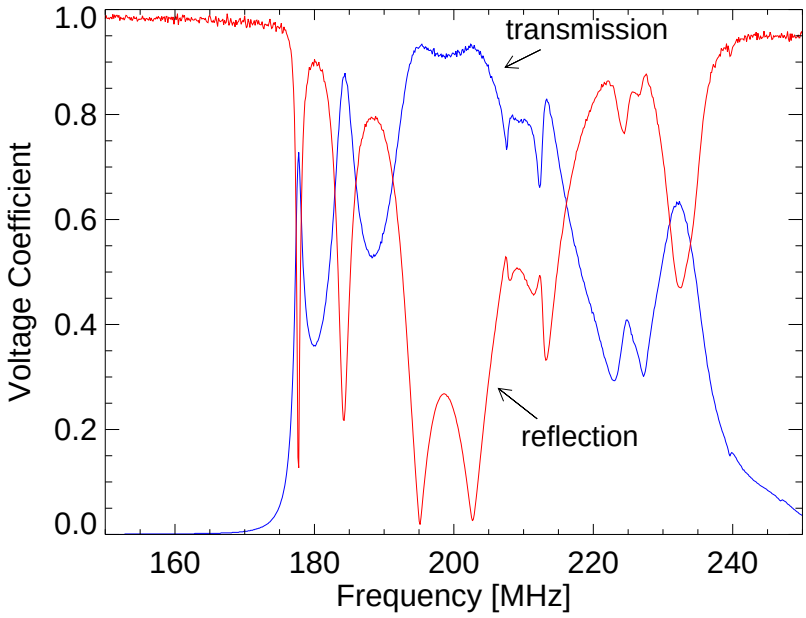

Fig. 6.7: Voltage transmission and reflection coefficients of the top-launch CCC antenna measured with NWA.

Phase measurements at the edges of the radiating part (inboard side at R = 0.193 m and outboard side at R = 0.378 m) and the center (R = 0.285 m) were also performed with the ES probe. The measured phase profiles are shown in Fig. 6.9(a). There is no large difference in the phase profile, and the result is consistent with the design. The $N_{||,0}$ spectrum calculated at R = 0.139 m, R = 0.285, and R = 0.378 are plotted in Fig. 6.9(b). The amplitude ratio of the electric field measured by the ES probe at R = 0.139 m, R = 0.285 m, and R = 0.378 m is 0.66 : 1.0 : 0.85. The peak of the $N_{||,0}$ spectrum are approximately -3, -4, and -6 at R = 0.139 m, R = 0.285 m, and R = 0.378 m respectively. Most of the $N_{||,0}$ spectral power is contained in the region -10 to -2 in vacuum.

Also the power ($\propto E^2$) and phase were measured by the ES probe along R (Fig. 6.10). The power is nearly constant along R. The phase shift from R = 0.139 m to R = 0.378 m is about 20 degrees.

6.3.5 Installation on TST-2 and antenna conditioning

The top-launch CCC antenna was successfully installed in TST-2 (Fig. 6.6). The center of the antenna surface is placed at $(R, z) = (0.285, 0.335)$ m with the an-

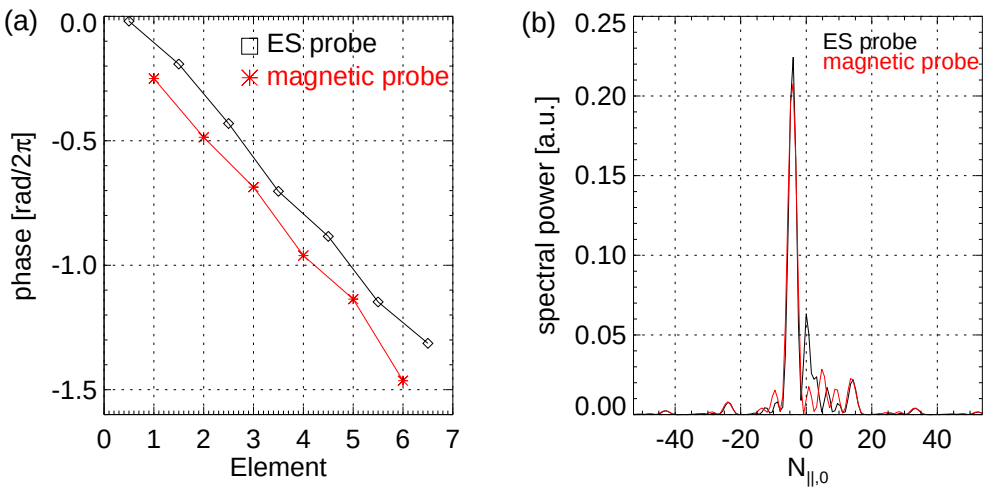

Fig. 6.8: (a) Phase profile measured with an RF magnetic probe (∗, red) and an electrostatic probe (◇, black). (b) $N_{||,0}$ spectra calculated at $R = 0.285$ m.

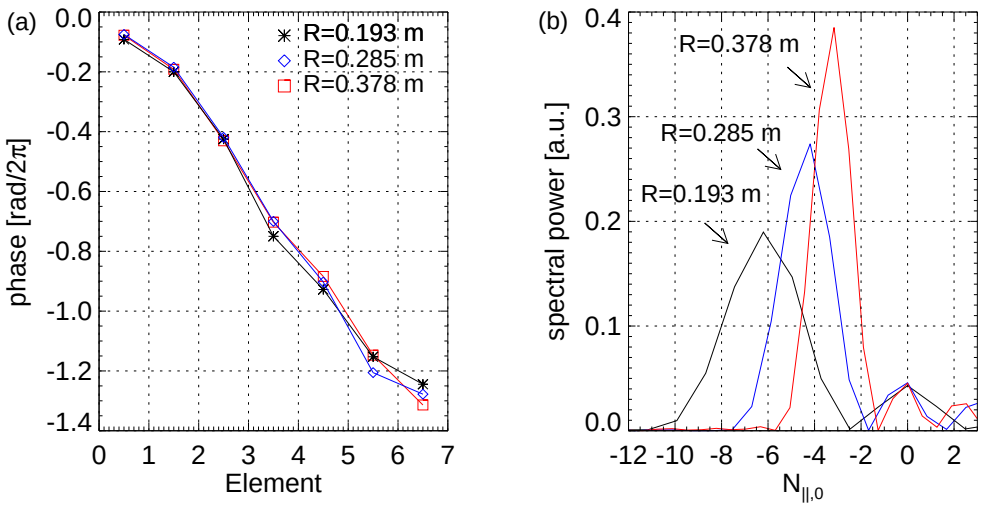

Fig. 6.9: (a) Phase profile measured with an electrostatic probe at $R = 0.139$ m (black), $R = 0.285$ (blue), and $R = 0.378$ (red). (b) Calculated $N_{||,0}$ spectra. The measured amplitude ratio of the electric field at $R = 0.139$ m, $R = 0.285$ m, and $R = 0.378$ m is 0.66 : 1.0 : 0.85.

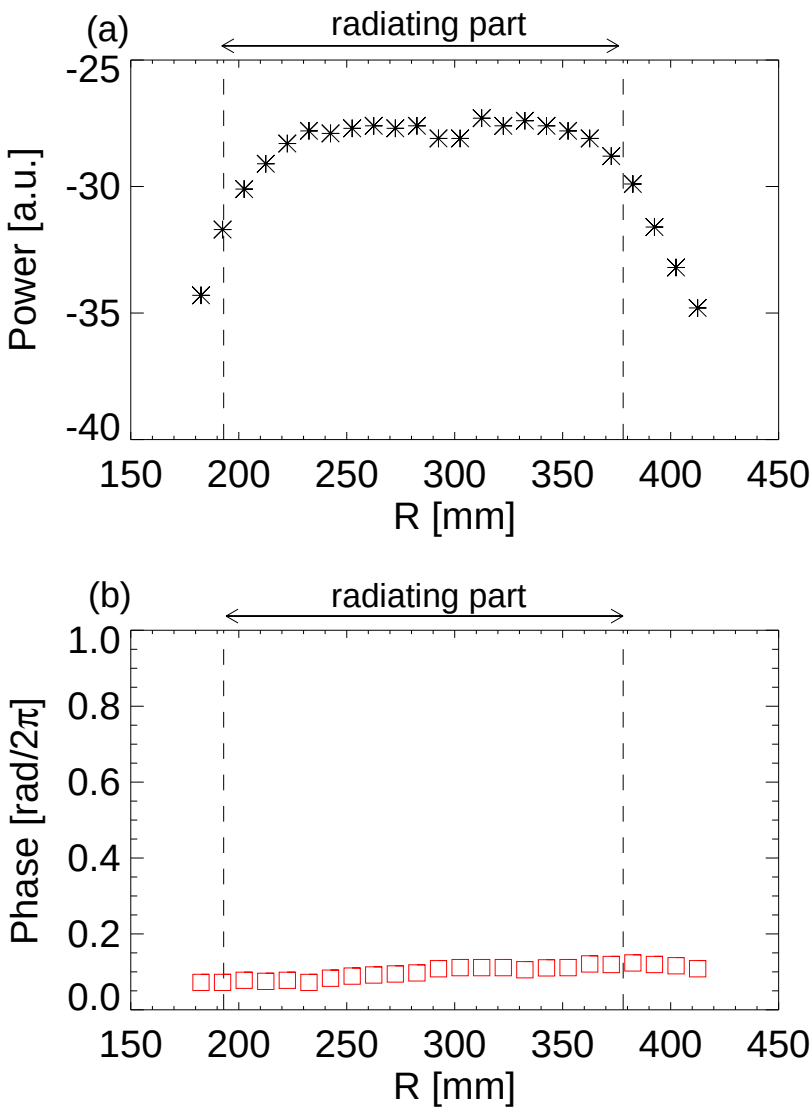

Fig. 6.10: Power ($\propto E^2$, black $*$) and phase (red $\diamond$) profiles along R measured with the ES probe.

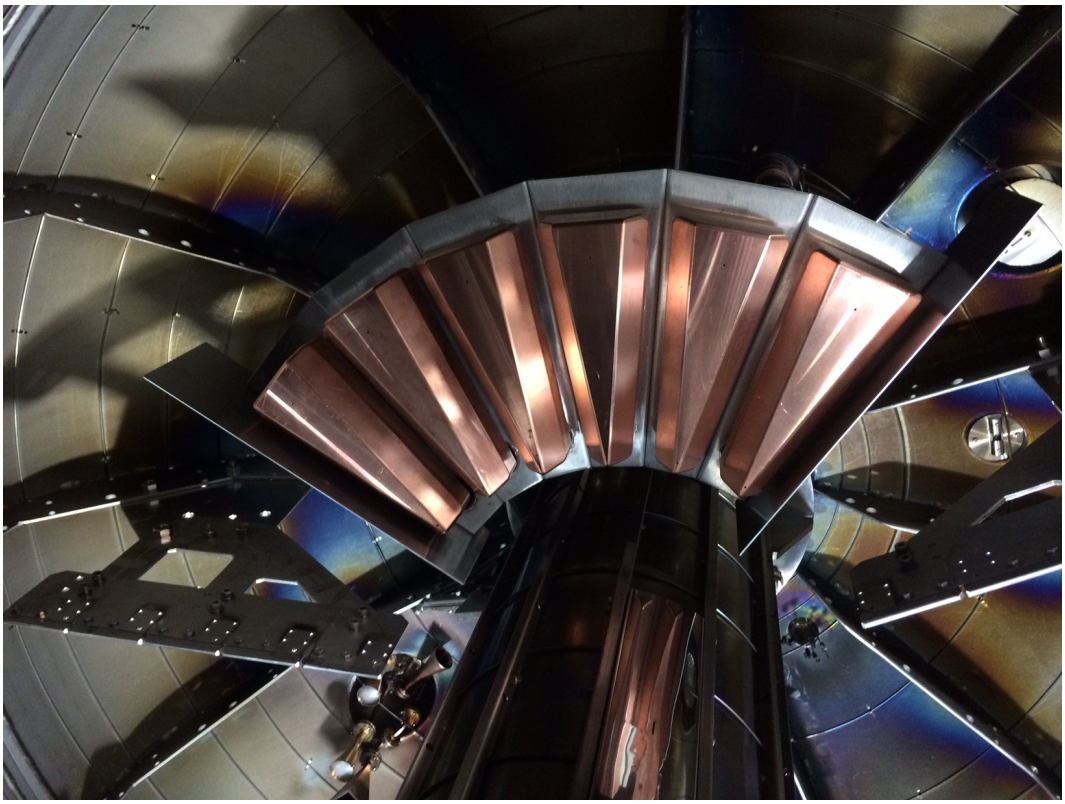

Fig. 6.11: Photograph of the top-launch antenna installed in TST-2.

tenna limiter installed at $z = 0.300$ m. The antenna limiter is located 15 degrees away from the antenna. The bottom limiter was also installed, but at $z = 0.45$ m. In this experiment, the RF power and phase monitoring system (RF magnetic probe array) has not been installed.

Conditioning of the antenna was performed with repetitive short multi-pulse injections (100 μs $\times$ 9) of RF power. Over 2000 injections into vacuum with RF power in the range 1–100 kW were performed over three days. Conditioning is needed to drive out the accumulated gas from the antenna surface. After conditioning, over 80 % of the input power was transmitted to the output port and less than 1 % of the input power was reflected from the input port for short pulse injection at high power. However, the outgas is still non-negligible for long pulse injection into the plasma. The outgas from the antenna increases the plasma density and cools the plasma.

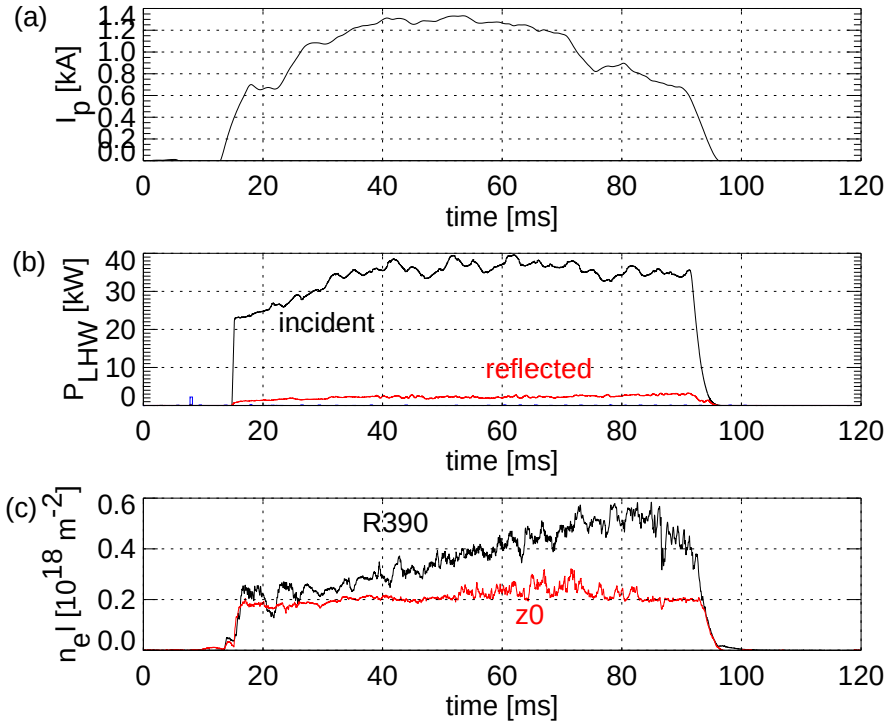

Fig. 6.12: Discharge from the first I_p ramp-up experiment using the top-launch CCC antenna: (a) Plasma current, (b) LHW power, (c) line-integrated density through a vertical chord at $R = 0.39$ m (black) and through a horizontal chord at $z = 0$ m.

6.3.6 Plasma experiments

Non-inductive I_p ramp-up experiments was performed using the top-launch CCC antenna (Fig. 6.12). This is the first attempt in the world to initiate and ramp up the plasma current using top-launching of the LHW in tokamaks. The high antenna-plasma coupling efficiency (~ 100 %) and low reflectivity (1–10 %) were verified in this experiment (Fig. 6.12(b)). Since antenna conditioning has not completed yet, the line-integrated density in low I_p discharges (< 5 kA) is higher compared to standard operation using the outboard-launch antenna by a factor of 3–5 (Fig. 6.12(c)). After sufficient conditioning, higher plasma currents than 1.5 kA obtained in this experiment should become possible. According to previous experience with the outboard-launch antenna, the line-integrated density reduces should reduce to $0.1–0.2 \times 10^{18}\mathrm{m}^{-2}$.

Electron density and temperature profiles were measured by Thomson scattering (Fig. 6.13). The measured density is as high as for high I_p operation using

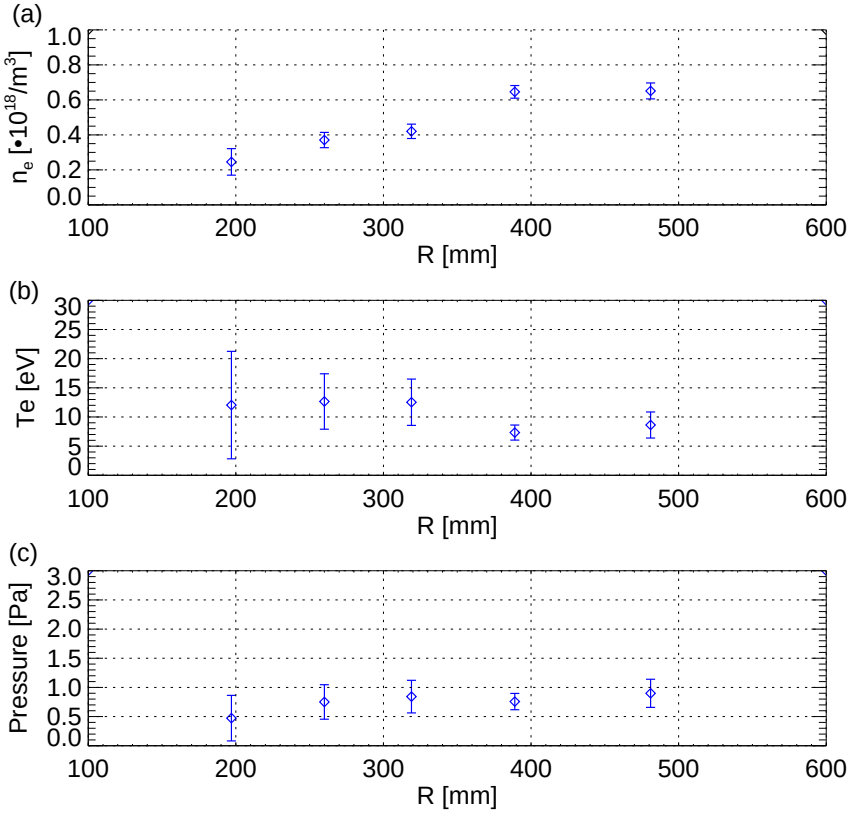

Fig. 6.13: (a) Electron density, (b) electron temperature, and (c) electron pressure profiles measured by Thomson scattering in a discharge obtained in the first experiment using the top-launch CCC antenna.

the outboard-launch antenna, and hence the slowing down time is much shorter in such a low I_p discharge. Because of the low I_p and high density, the electron temperature is low. After further conditioning of the antenna, it is expected that lower density and higher temperature can be obtained.

Chapter 7

Conclusions

Non-inductive plasma current ramp-up experiments were performed on the TST-2 spherical tokamak using the newly developed Capacitively-Coupled Combline (CCC) antenna. The CCC antenna was developed in collaboration with General Atomics (GA) to launch the LHW with a sharp, single-peaked $N_{\|,0}$ spectrum directly, and to obtain low reflectivity in order to achieve higher plasma currents. The peak of the $N_{\|}$ spectrum is adjusted to -5.5 and contains only components from -2 to -8 in a single peak in the absence of plasma. The input impedance of the CCC antenna was adjusted to 50Ω and the reflectivity of less than 0.1 % was achieved. There was an additional 10 % reflection from the vacuum feedthrough, but this level of reflectivity is not a problem for aiming at higher I_{p} with higher LHW power.

The plasma current was successfully ramped up to ~20 kA using the CCC antenna with low reflectivity (≤ 10%) and high antenna-plasma coupling efficiency (100%). The achieved plasma current is higher than those achieved in earlier experiments on TST-2. The low reflectivity is one of the main aims of CCC antenna development since high reflectivity due to low antenna-plasma coupling limited the input RF power for the Grill antenna. The $N_{\|,0}$ spectrum is also improved greatly. The $N_{\|,0}$ spectrum was calculated based on measurements by RF magnetic probes installed under the CCC antenna. The launched spectrum contains only components with $-9 \leq N_{\|,0} \leq -2$ is a single peak, with negligible secondary peaks. The spectral power at the main peak of the CCC antenna spectrum is larger than that of the Grill antenna spectrum by a factor of 3. Under this condition, the number of effective elements was $\mathrm{n_{eff}}$ = 6–8, which was optimized by adjusting the position of the antenna limiter. To achieve $\mathrm{n_{eff}}$ = 13, the antenna limiter must be positioned farther into the plasma to reduce antenna-plasma coupling, but it would also increase reflection of the LHW by the antenna limiter. We also found that the main limiter is less effective than the antenna limiter. The toroidal location of the main limiter was 60° counterclockwise toroidally from the antenna limiter

on the input side.

In order to investigate the optimum antenna for I_p ramp-up by the LHW at 200 MHz, a comparison among the CCC antenna (LHW excitation, with a sharp, single-peaked $N_{\|,0}$ spectrum), the Grill antenna (LHW excitation, with a broad, double-peaked $N_{\|,0}$ spectrum), and the ICC antenna (FW excitation, with a sharp, single-peaked $N_{\|,0}$ spectrum) was made. The CCC antenna achieved the highest current drive figure of merit (by a factor of 2–3 compared to other two antennas), and a higher antenna-plasma coupling efficiency (CCC: 100%, Grill: 40%–80%, ICC: 40%) at $I_p = 10\,\mathrm{kA}$. The I_p-P_{rad} relationship indicates that the LHW contributes more effectively to I_p ramp-up than the FW by a factor of 2 at $I_p = 15\,\mathrm{kA}$. It was difficult to evaluate the dependence of I_p ramp-up efficiency on the $N_{\|,0}$ spectrum from the obtained results.

It was also revealed that I_p ramp-up is limited by the toroidal magnetic field (B_t) and the plasma density. The obtained data can be fitted well with the mode conversion curve for $N_\| = -5.5$ (corresponds to the peak of the $N_{\|,0}$ spectrum), and hence the B_t limit and the density limit are most likely caused by mode conversion of the LHW to the FW. The achieved I_p also exhibits a positive correlation with the plasma density. The increase of density results in a more rapid slowing down of the accelerated high energy electrons. To achieve higher I_p using the CCC antenna, not only the pulse length, but also the increases of B_t and density are also necessary. Since the increases of Bt and density leads to LHW power loss by PDI when $\omega < 2\omega_{LH}$, 30–50 kA is the limit for plasma current at 200 MHz if I_p increases with density. We also found a method to break the B_t limit by launching higher LHW power, but this is not an efficient method. For example, to increase I_p by 3 kA from 10kA, 40 kW of additional LH power is needed, which is equal to the LHW power to reach 10 kA under the standard operation.

It was also found that removing the scrape-off layer (SOL) plasma above and below the LCFS is effective for achieving higher I_p. In the case without the upper and lower limiters (z450 limiter, $z = \pm 0.45$ m, 150 mm away from the LCFS), I_p ramp-up ceased when the density reached $0.4 - 0.6 \times 10^{18}\ \mathrm{m}^{-3}$. This density limit was not alleviated by increasing the magnetic field, and hence the density limit is not caused by mode conversion to the FW. LHW power loss in the SOL is a reasonable cause for I_p saturation at high density. The density at the upper z450 limiter measured by a Langmuir probe was higher than the cutoff density, and the presence of the LHW was verified by RF rectification observed on the measured floating potential.

We succeeded in inventing a plasma density suppression method using the ECW to keep the density lower than the density limit. The ECW was launched into the plasma with the fundamental EC resonance located at the nominal plasma center ($R \approx 0.38\,\mathrm{m}$, $P_{EC} \simeq 2\,\mathrm{kW}$). Despite the lower EC power than the LH power by a factor of 15, the ECW was effective in reducing the plasma density. The

decrease in $n_e l$ (more precisely, the suppression of the $n_e l$ increase) was approximately 10%.

In order to measure the density profile inside the antenna limiter, Langmuir probe arrays were installed on the inside surfaces (antenna-facing sides) of the input side and output side antenna limiters. The measured density profile was fitted well an exponential function. According to the fit, the density extrapolated to the antenna surface was $\sim 1.2 \times 10^{15}\mathrm{m}^{-3}$, which is higher than the cutoff density for the LHW ($\approx 5 \times 10^{15}\mathrm{m}^{-3}$). The measured density at edge of the antenna limiter was $\sim 2.0 \times 10^{15}\mathrm{m}^{-3}$. Thus, the measured density decay length is approximately 65 mm. The measurement was performed after sufficient wall and antenna conditioning. After opening the vacuum vessel, the density at the edge of the antenna limiter increases and the density decay length reduces. In addition to the density measurement, the effect of RF rectification was observed only at the input side. This result is reasonable because the launched LHW with a unidirectional spectrum can hit only the surface to which the LHW propagates, which is the input side.

The predicted I_p ramp-up limitations, caused by mode conversion and LHW power loss in the SOL, can be avoided by developing a top-launch antenna, according to the results of ray-tracing analysis. The LHW excited by the top-launch antenna undergoes a rapid up-shift in the parallel wavenumber of the LHW as it propagates towards the plasma center, and is directly absorbed by bulk electrons. In addition to the up-shift, the LHW accessibility condition also improves due to the higher toroidal magnetic field at smaller major radii (by a factor of two compared to the outboard-launch). I_p ramp-up at a low magnetic field, which prevents LHW power loss by PDI at high magnetic fields (> 0.2 T), may become possible. The top-launch antenna was developed in collaboration with GA. It has the same structure as the outboard-launch CCC antenna since the utility of CCC antenna has been verified experimentally. The top-launch antenna consists of 6 radiating elements, and the injected $N_{\|}$ is in the range -2 to -10 in vacuum. The top-launch antenna was installed at $z = 0.334$ m and the antenna limiter at $z = 0.3$ m. The low reflectivity ($\sim$ 1%) and the high antenna-plasma coupuling ($\sim$ 100 %) have been verified with the plasma.

Chapter 8

Acknowledgements

The completion of this thesis would not have been possible without the advice and support of numerous people. I wish to acknowledge them here.

First, I would like to express my sincere gratitude to my supervisor Professor Takase for supporting this work. I could refine my skills as a researcher for five years under his professionalism in everything, but especially in RF physics and engineering. He also gave me opportunities for collaborative research with GA and MIT to develop LHW antennas and wavenumber measurement systems. I could also take a mental break by playing tennis with him and labmates during lunch time every day (except in case of storm). Without him this work would not have been possible.

Besides my supervisor, I would like to thank Dr. Charles Moeller, Professor Ejiri, and Professor Tsujii. Charles, the world's expert on RF engineering, helped me with LHW antenna development, and gave me many useful advices on antenna tuning and conditioning. Professor Ejiri gave me insightful comments on my research at weekly meetings, and his comments steered me to better directions. Also the importance of finding pleasure in difficulty is what I learned from his attitude towards research. Professor Tsujii frequently advised me on wave theory and GENRAY/CQL3D simulations, although he was extremely busy with work and his family. I was impressed with not only his intelligence, but also with his gentle disposition.

I want to extend my gratitude to Professors at NIFS and former labmates, Oosako, Wakatsuki, Kakuda, and Hiratsuka. They taught me all about the RF system, and encouraged me when I was struggling to meet deadlines. I also want to acknowledge colleagues at MIT. Greg helped me develop the RF magnetic probe array for Alcator C-Mod, and pushed the project to measure the LHW wavenumber ahead. The digitizer system used in that experiment was developed by Seung Gyou, who frequently informed me of the progress. I could not have worked smoothly on C-Mod without Syun'ichi's support.

I also would like to thank all my labmates for their contributions to this work. These include Inada, Yajima, Yamazaki, Yoshida, Togashi, Toida, Furui, Sonehara, Imamura, Tsuda, Nakamura, Homma, Subrow, Takeuchi, and Takahashi who all generously contributed data that were used in this thesis. In particular the RF group, Inada, Yajima, Yamazaki deserve special recognition. I could take a mental break by going out for beer with them. Furui, my colleague, taught me the meaning of "Cheers". He also taught us how to play tennis, and our lab team finally won the championship in the tennis tournament sponsored by the Dean of the Graduate School of Frontier Sciences. I would also like to acknowledge Professor Yamada, my drinking buddy, for his unerring guidance and many fruitful discussions. I would never forget their help and contributions.

Lastly, my most sincere thanks are reserved for my parents for their continuous love and support.

References

[1] J. Wesson, *Tokamaks*, fourth edn.(Oxford University Press, New York, 2011).

[2] J.P. Freidberg, *Plasma Physics and Fusion Energy*(Cambridge University Press, Cambridge, 2007).

[3] J.D. Lawson, 'Some criteria for a power producing thermonuclear reactor', Proc. Phys. Soc. Sect. B, **70**, 1 (2002).

[4] M. Kikuchi, K. Lackner and M. Q. Tran, *FUSION PHYSICS*(IAEA, Vienna, 2012).

[5] L. A. Artsimovich, Nucl. Fusion **12**, 2 (1972).

[6] T. Fujita, *et al.*, 'High Performance Experiments in JT-60U Reversed Shear Discharges', 17th IAEA Fusion Energy Conf., IAEA-CN-69/EX1/2 (1998).

[7] A. Sykes, *et al.*, Phys. Plasmas **8**, 2101 (2001).

[8] H.-S. Park, *et al.*, 'High-Adiabat High-Foot Inertial Confinement Fusion Implosion Experiments on the National Ignition Facility', Phys. Rev. Lett., **112**, 055001 (2014).

[9] A. Iiyoshi, *et al.*, 'Overview of the Large Helical Device project', Nucl. Fusion **39**, 9 (1999).

[10] B. E. Chapman, *et al.*, 'High confinement plasmas in the Madison Symmetric Torus reversed-field pinch ' **9**, 2061 (2002).

[11] E. B. Hooper, *et al.*, 'Sustained Spheromak Physics Experiment(SSPX): design and physics results', Plasma Phys. Control. Fusion **54**, 26 (2012).

[12] M. Keilhacker, *et al.*, 'High fusion performance from deuterium-tritium plasmas in JET',Nucl. Fusion **39**, 2 (1999)

[13] F. Saint-Laurent, *et al.*, 'Steady state operation and control experiments on Tore Supra', Nucl. Fusion **40**, 6 (2000).

[14] `http://www.iter.org`.

[15] K. Tomabechi, *et al.*,'ITER conceptual design' Nucl. Fusion **31**, 6 (1991).

[16] Ruth Berger Goldston and Audrey Rutherford, *Plasma Physics*(Taylor & Francis Group, New York, 1995).

[17] M. Greenwald, *et al.*, 'A new look at density limits in tokamaks', Nucl. Fusion **28**, 12 (1988).

[18] P. R. Thomas, *et al.*, 'Observation of Alpha Heating in JET DT Plasmas', **80**, 25 (1998).

[19] Y.-K.M. Peng, 'The physics of spherical torus plasmas', Phys. Plasmas **7**, 5 (2000).

[20] A. Sykes, *et al.*, Phys. Plasmas **4**, 1665 (1997).

[21] S. M. Kaye, *et al.*, 'Confinement and local transport in the National Spherical Torus Experiment(NSTX)', Nucl. Fusion **47**, 490 (2007).

[22] L.A. El-Guebaly, The ARIES Team, 'Nuclear performance assessment of ARIES-AT', Fusion Eng.Des. **80**, 99 (2006).

[23] T. Nishitani, *et al.*, 'Neutronics design of the low aspect ratio tokamak reactor, VECTOR', Fusion Eng. Des. **81**, 1245 (2006).

[24] Y. Takase, *et al.*, 'Initial results from the TST-2 spherical tokamak', Nucl. fusion **41**, 1543 (2002).

[25] M. Ono, *et al.*, 'Exploration of spherical torus physics in the nstx device', Nucl. Fusion **40**, 557 (2002).

[26] M. Brambilla, 'Electron Landau damping of lower hybrid waves', Nucl. Fusion **18**, 493 (1978).

[27] N. J. Fisch, 'Theory of current drive in plasmas', Rev. Mod. Phys. **59**, 1(1987).

[28] S. Kudo, *et al.*, 'Toroidal Plasma Current Startup and Sustainment by rf in the WT-2 Tokamak', Phys. Rev. Lett. **50**, 25 (1983).

[29] A. Ando, *et al.*, 'Enhancement of efficiency for lower hybrid current drive by electron cyclotron heating in the WT-2 tokamak', Nucl. Fusion **26**, 1 (1986).

[30] F. Jobes, *et al.*, 'Formation of a 100-kA Tokamak Discharge in the Princeton Large Torus by Lower Hybrid Waves', Phys. Rev. Lett. **52**, 12 (1984).

[31] Y. Takase, *et al.*, 'Plasma current start-up, ramp-up, and achievement of advanced tokamak plasmas without the use of ohmic heating solenoid in JT-60U', J. Plasma Fusion Res. **78**, 8 (2002).

[32] T. Shinya, *et al.*, 'Non-inductive plasma start-up experiments on the TST-2 spherical tokamak using waves in the lower-hybrid frequency range', Nucl. Fusion **55**, 8 (2015).

[33] V. V. D'yachenko, *et al.*, 'Noninductive Plasma Generation and Current Drive in the Globus-M Spherical Tokamak', Plasma Phys. Rep. **39**, 189 (2013).

[34] M. Uchida, *et al.*, 'Rapid Current Ramp-Up by Cyclotron-Driving Electrons beyond Runaway Velocity', Phys. Rev. Lett. **104**, 065001 (2010).

[35] V. F. Shevchenko, *et al.*, 'Electron Bernstein wave assisted plasma current start-up in MAST', Nucl. Fusion **50**, 5 (2010).

[36] V. F. Shevchenko, *et al.*, 'Long Pulse EBW Start-up Experiments in MAST', EPJ Web of Conferences **87**, 02007 (2015).

[37] H. Idei, *et al.*, 'Fully Non-Inductive Current Drive Experiments Using 28 GHz and 8.2 GHz Electron Cyclotron Waves in QUEST', 25th Fusion Energy Conference, EX/P1-38 (2014).

[38] T.R. Jarboe, 'Formation and steady-state sustainment of a tokamak by coaxial helicity injection', Fusion Technol. **15**, 7-11 (1989).

[39] C.W. Barnes, *et al.*, 'Experimental determination of the conservation of magnetic helicity from the balance between source and spheromak', Phys. Fluids **29**, 3415 (1986).

[40] B.A. Nelson, *et al.*, 'Demonstration of 300 kA CHI-startup current, coupling to transformer drive and flux savings on NSTX', Nucl. Fusion **51**, 063008 (2011).

[41] R. Raman, *et al.*, 'Non-inductive solenoid-less plasma current startup in NSTX using transient CHI', Nucl. Fusion **47**, 792-99 (2007).

[42] R. Raman, *et al.*, 'Non-inductive current generation in NSTX using coaxial helicity injection', Nucl. Fusion **41**, 8 (2001).

[43] J.A. Reusch, *et al.*, 'Non-solenoidal Startup via Local Helicity Injection on Pegasus: Progress and Plans', 57th Annual Meeting of the APS Division of Plasma Physics, Savannah, Georgia, **60**, 19 (2015).

[44] T. H. Stix, *Waves in plasmas* (Springer-Verlag, New York, 1992).

[45] L. D. Landau, 'On the vibration of the electronic plasma', J. Phys. USSR **10**, 25 (1946).

[46] R. K. Fisher, R. W. Gould, 'Resonance cones in the field pattern of a radio frequency probe in a warm anisotropic plasma', Phys. Fluids **14**, 857 (1971).

[47] P. Bonoli, 'Linear theory of lower hybrid heating', IEEE Trans.Plasma Science **12**, 2 (1984).

[48] V. E. GOLANT, 'Plasma penetration near the lower hybrid frequency', Sov. Phys. Tech. Phys. **16**, 1980 (1972).

[49] P. M. BELLAN, M. PORKOLAB, 'Propagation and mode conversion of lower-hybrid waves generated by a finite source', Phys. Fluids **17**, 1592 (1974).

[50] P. Bonoli and E. Ott, 'Toroidal and scattering effects on lower - hybrid wave propagation', Phys. Fluids **26**, 2 (1982).

[51] P.M. Bellan and M. Porkolab, 'Experimental studies of lower hybrid wave propagation', Phys. Fluids **19**, 995 (1976).

[52] Y. Takase, *et al.*, 'Observation of parametric instabilities in the lower-hybrid range of frequencies in the high-density tokamak', Phys.Fluids **28**, 983 (1985).

[53] R. Cesario, *et al.*, 'Parametric instabilities excited by ion sound and ion cyclotron quasi-modes during lower hybrid heating of tokamak plasmas', Nucl. fusion **29**, 1709 (2011).

[54] M. Porkolab, 'Theory of parametric instability near the lower-hybrid frequency', Phys.Fluids **17**, 1432 (1974).

[55] M. Porkolab, 'Parametric instabilities due to lower-hybrid radio frequency heating of tokamak plasmas', Phys. Fluids **20**, 2058 (1977).

[56] `https://fusion.gat.com/theory/Efit`

[57] A.P. Smirnov, *et al.*, *GENRAY Code* (1994)

[58] R. J. Perkins, *et al.*, 'The Contribution of RF Rectification to Field-Aligned Losses of HHFW Power to the Divertor in NSTX', Nucl. Fusion, (2014)

[59] T. Wakatsuki, *et al.*, 'Plasma current start-up experiments using a dielectric-loaded waveguide array antenna in the TST-2 spherical tokamak', Nucl. Fusion **54**, 14 (2014).

[60] Y. Takase, *et al.*, 'Development of a plasma current ramp-up technique for spherical tokamaks by the lower hybrid wave', Nucl. Fusion **51**, 8 (2011).

[61] C. P. Moeller, *et al.*, 'Combline antennas for launching traveling fast waves',AIP Conference Proceedings **289**, 323 (1994).

[62] T. Ogawa, *et al.*, 'Radiofrequency experiments in JFT-2M: Demonstration of innovative applications of a travelling wave antenna', Nucl. Fusion **41**, 1767 (2002).

[63] Y. Takase, *et al.*, 'Non-inductive plasma initiation and plasma current ramp-up on the TST-2 spherical tokamak', Nucl. Fusion **53**, 6 (2013)

[64] T. Maekawa, *et al.*, 'Up-shifted frequency electron-cyclotron current drive in a lower hybrid current drive plasma', Phys.Rev. Lett. **70**, 17 (1993).

[65] T. Shinya, *et al.*, 'Plasma Density Suppression by Electron Cyclotron Wave in Lower Hybrid Wave Driven TST-2 Spherical Tokamak Plasma', Plasma Fusion Res. JSPF **9**, 1202133(2014).